Coherent Radar Backscatter Modelling for Drones in the OFDM Framework

by

Daniel Charron

A thesis submitted to the University of Ottawa
in partial fulfillment of the thesis requirement for the degree of

Master of Applied Science

in

Electrical Engineering and Computer Science

Examining Committee

The following served on the Examining Committee for this thesis.

External Examiner: **Ioannis Lambadaris**
Full Professor and Chancellor's Professor,
Department of Systems and Computer Engineering,
Carleton University

Internal Examiner: **Claude D'Amours**
Professor and Director,
School of Electrical Engineering and Computer Science,
University of Ottawa

Supervisor: **Miodrag Bolic**
Professor, Computer Engineering Undergraduate Associate Director;
Interim Applied AI ELG Program Graduate Director

Other Member(s): **Iraj Mantegh**
Senior Research Officer
Aerospace Research Center
National Research Council Canada

Declaration of Authorship

I hereby certify that this thesis is entirely my own original work except where otherwise indicated. I am aware of the University's regulations concerning plagiarism, including those concerning consequent disciplinary actions. Any use of the works of any other author, in any form, is properly acknowledged at their point of use.

Abstract

The problem statement of this thesis is to construct a simple, versatile, closed-form simulation model which can be used to model Orthogonal Frequency Division Multiplexing (OFDM) pulsed-radar reflections from drones.

General simulation methodologies exist which allow a simulation designer to provide an arbitrary transmit waveform, system parameters and a set of point-scatterer positions and velocities representing complex radar targets for each time sample considered in the simulation and to generate signal reflection predictions. On the other hand, certain over-simplified methodologies exist to generate reflection predictions from propellers or drones and significantly simplified to allow a closed-form solution.

The manner in which to simulate signal reflections from complex targets explored in this thesis provides a middle-ground between the over-generalized and over-simplified simulation methodologies and is adapted to the specific use-case of OFDM pulsed-radar to model drone targets. The benefit of this simulation methodology is its ease-of-use and flexibility. The solution allows one to provide system parameters, drone parameters and a drone trajectory to produce accurate backscatter predictions without having to model all the individual point-scatterers for the radar target at each point in time. Additionally, the simulation methodology presented in this thesis is derived in a separate manner than the current standard for complex target modeling which is having well-placed point-scatterers anchored to the simulated target. If one generates prediction results from two separate simulation algorithms, then their certainty in simulation accuracy increases.

This thesis presents how the simulation model derived within produces almost identical results to the state-of-the-art simulation methodology, where the same complex radar target is modeled as a set of moving point-scatters with varying Radar Cross-Sections (RCS) at each point in discrete-time. Since the model derived within require significantly less setup and modeling efforts from the user and provides roughly the same computational complexity for modeling drone targets in the OFDM pulsed-radar framework, it is the better option.

The main metrics used for comparison between the different simulation methodologies are the Fourier transforms of the received signal, micro-Doppler signatures and the range-speed response for the radar system. All three metrics are shown to match the state-of-the-art in the proposed simulation method.

Acknowledgements

Thank you to my supervisor Prof. Miodrag Bolic for his guidance through this process. Thank you to Dr. Yogesh Nijsure for all his helpful feedback, ideas and wealth of knowledge in this field. Thank you to Dr. Hamid Azad for coordinating much of the logistics. Thank you to Mr. Kenny Bala for his helpful discussions and upcoming useful contributions in this field. Thank you to Dr. Iraj Mantegh for his reviews and suggestions. Thank you to Dr. Sina Sajjadi for his helpful discussions and constructive feedback. Thanks to all my colleagues in the Computational Analysis and Acceleration Research Group at the university of Ottawa. This thesis is partially supported by the National Research Council Canada's New Beginning Ideation Fund. Credit goes to the University of Waterloo for their thesis template as well as Prof. Wail Gueaieb for his repackaging of the template.

Dedication

This is dedicated to my fiancée Olivia McCarthy and my mother Monique Charron.

Table of Contents

List of Tables

List of Figures

Chapter 1

Introduction

1.1 Problem Statement and Motivation

The primary problem statement for this research is:

Construct a simple, versatile, closed-form simulation model which can be used to model OFDM pulsed-radar reflections from drones.

Literature available adjacent to this problem make similar contribution but restrict models in some manner. Specifically, [15, 30] restrict the height of the target to be equal to that of the transceiver and restrict the number of propellers to unity. [27] restricts the rotor to contain 4 blades with one scatterer per blade. [32, 41] state that they use the point-scatterer model without going into detail as to how it is done. This is difficult for someone attempting to build a simulator to recreate. [25, 35] assume that the rotors are constantly rotating in the same orientations which is not always the case. As the simulation evolves, the target changes orientation, velocity, position, etc.

A simulator like this one is useful because, as [13, 36] show, the micro-Doppler signatures are an ideal set of data for an AI system to learn from. A simulator which can allow one to define any specific scenario desired and generate valuable training data for a Machine Learning (ML) model. Radar performance can be evaluated using this simulator in the cases where different OFDM symbols are to be compared, for example using their ambiguity functions, before being deployed in the real-world. The simulator can be used to test JCR/ISAC use-cases where certain data symbols would be designated as "communication symbols" and not radar symbols. Additionally, in Low Probability of Intercept (LPI) radar, this simulator can be used to define complex drone models and trajectories to validate

performance. A simulation which is in agreement with the standard simulation strategy also increases confidence that both models are going reliably predict real-world data.

1.1.1 Application

As Uncrewed Aerial Vehicles (UAV)s including drones continue to become more common for both recreation, law enforcement and military purposes, being able to detect UAVs becomes a increasingly valuable capability. When UAVs operate in "dark" mode, where they do not emit electromagnetic waves of any kind, it becomes even more useful to be able to identify whether a UAV is present and infer its characteristics. These characteristics include the UAV's model, position, velocity, orientation, etc.

This detection and characteristic inference can done either actively, using the radar systems' transmit signal, or passively, using some other source of EM radiation which interacts with the UAV. The source of EM radiation under investigation affects how well and under which conditions the UAV can be detected. For example, in optical sensing or Lidar, a UAV could be very easily distinguished in a high Signal-to-Noise (SNR) ratio environment but would be very susceptible to range decay and weather related obstructions due to the frequency of the signal, compared to a lower frequency signal such as radar.

Another way in which this inference can be accomplished is by using the 5G NR infrastructure. Let there be a 5G transceiver nearby to a dark drone (the target). The 5G transceiver, if taken control of, could actively transmit a radar signal and analyze the backscatter signal to detect and infer about the target. This is the scenario for the research presented in this thesis.

1.2 Objectives

The objectives of this research are to

1. define a strategy for using OFDM as a radar,
2. derive what the expected coherent time and OFDM symbol-dependent backscatter signal should be in the OFDM radar strategy,
3. create a simulation tool using this strategy and generate backscatter predictions using it for different system configurations and

4. compare the result from the new simulation model with state-of-the-art simulation models to validate it.

Having all these steps completed, a conclusion can be made as to whether or not the new model is a viable alternative to state-of-the-art.

1.3 Contributions

The contribution to literature resulting from this thesis are

- deriving the closed-form expression for the expected backscatter signal for an OFDM pulsed-radar with varying communication symbols,
- the construction of the new simulation methodology for predicting OFDM radar backscatter derived within,
- successful comparison of the new model to state-of-the-art.

The contributions herein may be used in the future by other researchers for performing simulations of active OFDM radars with drone(s) nearby in a more simple way than to use state-of-the-art. Researchers may also use the analytical contribution herein to expand collective knowledge through further analysis.

1.4 Definitions, Conditions, Context, Assumptions and Limitations

The term *simulation* in this thesis refers the the process of recreating a real-world scenario virtually. Simulations may deterministic or partially randomized. The term *model* refers to the method of computing a particular result. The term *monostatic* refers to the radar system using the same antenna for both transmitting and receiving a signal. The transmitter and receiver are isolated from each other through hardware.

The 5G NR infrastructure could be used either actively or passively for target detection where in the active sensing mode, the 5G transceiver hardware would be severed from the 5G network to transmit only specific OFDM radar signals, enabling radar processing gains, instead of transmitting its standard 5G NR traffic. In the passive sensing mode, the 5G NR

receiver would need to correlate what it receives to what was transmitted from all the local 5G NR base stations. This document is focused on the former active sensing where a single monostatic transceiver is responsible for both generating and receiving the radar transmit and receive signals respectively. There are also bistatic and multistatic configurations for target detection but this work strictly examines the monostatic case.

The radar backscatter signal when a drone of arbitrary size is within the radar's unambiguous range is modeled by two separate reflection models which are closely examined, the Martin-Mulgrew point-scatterer models. From these radar signals, it is shown that UAV detection, classification and inference of radial distance, bulk velocity, rotor velocity and orientations are all possible.

The theoretical models that are used in this document have the ultimate goal of being applied to the 5G hardware context, that is, they are to be used specifically to model the backscatter signal which results from a radar transmitting a signal compliant with 5G standards and regulations. The 5G 3GPP communications standard uses OFDM for its signals. In OFDM, a set of orthogonal subcarriers are used to transmit information. The subcarriers are simple sinusoidal carriers at frequencies which are separated by their SubCarrier Spacings (SCS)s. To form an OFDM signal, the subcarriers are linearly combined. For this reason, the theoretical analysis begins with backscatter analysis of simple sinusoidal carrier transmit signals of the form $e^{j2\pi f_c t}$, where f_c is the carrier frequency, t is the analysis time and j is the imaginary unit. When a complex exponential signal is being transmitted, it is assumed to undergo I/Q modulation to preserve the imaginary component of the signal. I/Q demodulation is also assumed for the received signal.

The primary tools for detection, classification and inference are the radar range-speed response and the micro-Doppler signature of the target. These are presented in detail in subsequent sections.

Two separate theoretical models for modeling target backscatter are analyzed and compared to full-system simulation results offered by MATLAB. The first of the models is the Martin-Mulgrew model as presented in [30] and used in [13] & [15], henceforth referred to as the MM model. The model performs theoretical analysis for propeller backscatter signals. This model initially does not consider modification to frequency due to the Doppler effect aside from bulk-velocity of the UAV, as seen in more detail in Section 2.1.1, and therefore would not produce any micro-Doppler signatures. The MM model is augmented to show how the micro-Doppler effect could be included into the model. The framework for modeling the complex drone target is defined. The second model is to have a dedicated set of point-scatterers, each with their own Radar Cross-Sections (RCS), positions and velocities, as presented in [8] in a way which shows general scatterer behavior. This model

is adapted to fit the situation of complex drone modeling. This is the current industry standard for modeling complex radar targets.

This thesis presents only theoretical work and simulation data; no real-world experiments have been performed to validate the simulation method created herein. Other sources showing that the state-of-the-art point-scatterer model sufficiently matches real-world data such as [8] are relied upon to prove the simulation methodology is valid.

Standard 5G NR will make use of cyclic prefix for additional redundancy in signal communication. For the purpose of this active OFDM radar, the cyclic prefix is not considered since the redundancy is embedded in the need to repeat the OFDM radar pulse to achieve radar gains. Additionally, for a base station to be active in 5G NR, it must periodically transmit certain *keep-alive* signals. These signals are considered absent in the OFDM radar used herein since it is assumed the 5G transceiver has been taken-over for use specifically for radar.

1.5 Thesis Structure

This remaining portion of this thesis is structured into four separate chapters. Chapter 2 is the literature review which presents background information, review of the state-of-the-art and relevant papers. Chapter 3 derives the base form of the Martin-Mulgrew model and presents how the model can be augmented to include micro-Doppler modifications to the signal. Chapter 4 presents the strategy to adapt the augmented Martin-Mulgrew model for use with 5G OFDM transmit signals. Algorithms for simulations are provided and explained in detail at the end of the chapter. Chapter 5 is the conclusion of the thesis.

Chapter 2

Background Information and Literature Review

2.1 Background Information

In this section, several concepts necessary to the understanding of the work completed in this document are presented.

2.1.1 Reflected Doppler Signal

Let there be a monostatic radar which transmits a simple continuous signal modeled by $s_{tx}(t, f_c)$ which carries baseband data within the complex envelope of $s_c(t) = I(t) + jQ(t)$ composed of in-phase and quadrature components:

$$s_{tx}(t, f_c) = \mathrm{Re}\{s_c(t)e^{j2\pi f_c t}\} \tag{2.1}$$

where f_c is the carrier frequency, t is time and j is the imaginary unit. The amplitude of $s_{tx}(t)$ is the maximum voltage, which is proportional to the square root of the transmitted power (in Watts) and the Effective Radiated Power (ERP) of the transceiver.

Let there also be an electromagnetic-reflecting object moving in an arbitrary direction. This object is labeled as an Uncrewed Aerial Vehicle (UAV) for convenience. In Cartesian coordinates, let the coordinates of the transceiver be given as $\vec{x}_t$. Let the coordinates of the moving UAV be $\vec{x}_u$. The distance vector between the two position vectors is $(\vec{x}_u - \vec{x}_t)$.

For this scenario, there is need to express the relative velocity $\vec{v}_r$ between the transceiver and the UAV. For arbitrary velocity vectors for the transceiver and UAV, $\vec{v}_t$ and $\vec{v}_u$ respectively, the relative velocity can be expressed as the difference between the projections of the velocity vectors onto the distance vector $(\vec{x}_u - \vec{x}_t)$. Using typical notation,

$$\vec{v}_r = \text{proj}_{\vec{x}_u - \vec{x}_t}\vec{v}_u - \text{proj}_{\vec{x}_u - \vec{x}_t}\vec{v}_t \tag{2.2}$$

$$= \frac{\vec{v}_u \cdot (\vec{x}_u - \vec{x}_t)}{||\vec{x}_u - \vec{x}_t||}\frac{\vec{x}_u - \vec{x}_t}{||\vec{x}_u - \vec{x}_t||} - \frac{\vec{v}_t \cdot (\vec{x}_u - \vec{x}_t)}{||\vec{x}_u - \vec{x}_t||}\frac{\vec{x}_u - \vec{x}_t}{||\vec{x}_u - \vec{x}_t||} \tag{2.3}$$

$$= (\vec{v}_u \cdot (\vec{x}_u - \vec{x}_t) - \vec{v}_t \cdot (\vec{x}_u - \vec{x}_t))\frac{\vec{x}_u - \vec{x}_t}{||\vec{x}_u - \vec{x}_t||^2} \tag{2.4}$$

$$= (\vec{v}_u - \vec{v}_t) \cdot (\vec{x}_u - \vec{x}_t)\frac{\vec{x}_u - \vec{x}_t}{||\vec{x}_u - \vec{x}_t||^2}. \tag{2.5}$$

As the signal $s_{tx}(t, f_c)$ is transmitted, it travels a distance of $R = ||\vec{x}_u - \vec{x}_t||$. In terms of modeling the signal just before arrival at the target with $s_0(t, f_c)$, $s_{tx}(t, f_c)$ should be delayed — shifted by the time it takes for light to travel a distance of R meters. The time for light to travel a distance of R meters is R/c seconds so

$$s_{tx}(t - \frac{R}{c}, f_c) = \text{Re}\left\{ s_c(t - \frac{R}{c})e^{j2\pi f_c(t - \frac{R}{c})} \right\} = s_0(t, f_c) \tag{2.6}$$

$$= \text{Re}\left\{ s_c(t - \frac{R}{c})e^{j2\pi f_c t}e^{-j2\pi f_c \frac{R}{c}} \right\}. \tag{2.7}$$

Due to the relative velocity $\vec{v}_r$ between the transceiver and the UAV, the signal is Doppler-shifted by a frequency f_d when it is reflected. The observed (Doppler-shifted) frequency f_o can be calculated in two steps using the following relationship. The one-way, one-dimensional Doppler-shift formula [38] states that the observed frequency f_o is given by

$$f_o = \frac{c \pm v_q}{c \pm v_s} f_c \tag{2.8}$$

where v_q is the magnitude of the radial velocity of the receiver and v_s is the magnitude of the radial velocity of the source. The sign of v_q is positive when the receiver is moving towards the source and the sign of v_s is positive when the source is moving away from the receiver.

To apply this concept to this scenario using the relative velocity between the two objects $\vec{v}_r$, firstly, the scenario is observed from the point-of-view of the source such that $v_s = 0$ and $v_q = ||\vec{v}_r||$ when the receiver is moving towards the source. For the signal going from

the transceiver, acting as the Doppler source, to the UAV, acting as the Doppler receiver, the intermediate observed frequency f_i is given by

$$f_i = \frac{c + ||\vec{v}_r||}{c + 0} f_c. \tag{2.9}$$

Second, for the reflected signal going from the UAV to the transceiver, the Doppler roles are reversed. That is, the UAV acts as the source and the radar transceiver acts as the Doppler receiver. Since the UAV is moving towards the transceiver, $v_q = 0$ and $v_s = -||\vec{v}_r||$. The observed frequency f_o is then

$$f_o = \frac{c + 0}{c - ||\vec{v}_r||} f_i = \frac{c}{c - ||\vec{v}_r||} \frac{c + ||\vec{v}_r||}{c} f_c = \frac{c + ||\vec{v}_r||}{c - ||\vec{v}_r||} f_c. \tag{2.10}$$

Using the observed frequency, the Doppler-shift frequency is defined as follows and is further simplified.

$$f_d = f_o - f_c \tag{2.11}$$

$$= \frac{c + ||\vec{v}_r||}{c - ||\vec{v}_r||} f_c - f_c = f_c \left(\frac{c + ||\vec{v}_r||}{c - ||\vec{v}_r||} - 1 \right) \tag{2.12}$$

$$= f_c \left(\frac{c + ||\vec{v}_r||}{c - ||\vec{v}_r||} - \frac{c - ||\vec{v}_r||}{c - ||\vec{v}_r||} \right) = f_c \frac{2||\vec{v}_r||}{c - ||\vec{v}_r||}. \tag{2.13}$$

Since the relative velocity is insignificant with respect to the speed of light in the denominator, it is common to make the following approximation: $c - ||\vec{v}_r|| \approx c$. Therefore,

$$f_d \approx \frac{2 f_c ||\vec{v}_r||}{c} \tag{2.14}$$

for the UAV moving towards the transceiver. When the UAV moves away from the transceiver, similar analysis can be performed to show that

$$f_d \approx -\frac{2 f_c ||\vec{v}_r||}{c}. \tag{2.15}$$

The Doppler-shift applied to the reflected signal model at the target immediately after it is reflected by a UAV moving towards the transceiver, represented by $s_1(t)$, results in

$$s_1(t) = s_0(t, f_c + f_d) = \mathrm{Re}\left\{ s_c(t - \frac{R}{c}) e^{j2\pi(f_c + f_d)(t - \frac{R}{c})} \right\} \tag{2.16}$$

The signal then travels another distance R from the UAV back to the transceiver. To delay the signal once more due to the travel time to model the received signal to obtain $s_2(t)$, another time shift of R/c is performed:

$$s_2(t) := s_1(t - \frac{R}{c}) = \mathrm{Re}\Big\{ s_c(t - \frac{2R}{c}) e^{j2\pi(f_c+f_d)(t-\frac{2R}{c})} \Big\} \tag{2.17}$$

The modeled received signal before demodulation, $s_{rx}(t)$ is then obtained by inserting the approximate Doppler-shift and simplifying:

$$s_{rx}(t) \approx s_2(t) = \mathrm{Re}\Big\{ s_c(t - \frac{2R}{c}) e^{j2\pi f_c(1+\frac{2||\vec{v}_r||}{c})(t-\frac{2R}{c})} \Big\}. \tag{2.18}$$

Throughout the remainder of this thesis, it is implied that when complex exponential notation is used to describe a signal propagating through space, only the real part of the signal is actually being propagated as displayed in this section.

The amplitude of the received signal could be quantified using a form of Radar Range Equation (RRE) [28] which depends on ERP, propagation loss, receiver gain, etc. A standard form of RRE of the received signal for the Signal to Noise Ratio (SNR) relative to environmental noise power at the receiver is

$$\mathrm{SNR} = \frac{P_t G_t G_r \lambda^2 \sigma}{(4\pi)^3 R^4 k T_0 B F} \tag{2.19}$$

where

- P_t is the transmit power in Watts,
- G_t is the transmitter antenna gain in dBi,
- G_r is the receiver antenna gain in dBi,
- λ is the wavelength of the carrier frequency in meters,
- σ is the RCS in m^2,
- k is the Boltzman constant in Joules/Kelvin,
- T_0 is the receiver temperature in Kelvin,
- B is the receive bandwidth in Hertz,
- F is the receiver noise figure.

2.1.2 Rotation Matrices for Drone Modeling

Let the position of the center of reference frame i with respect to reference frame j be denoted $\vec{x}_i^j$. Let $\vec{p}^i$ denote a position vector at point $\vec{p}$ with respect to reference frame i. For a point $\vec{p}^i$ to be represented in reference frame j while i and j have the same origin, the rotation matrix $\boldsymbol{R}_i^j$, read as "$\boldsymbol{R}$ from i to j", can be used in the following manner:

$$\vec{p}^j = \boldsymbol{R}_i^j \vec{p}^i. \tag{2.20}$$

The values of this rotation matrix are derived below.

The point $\vec{p}^i$ with respect to the reference frame i is represented by a 3-element vector indicating the distance along each axis of reference frame i where the point is located. The point can be represented by a linear combination of the basis vectors representing each axis as in the following equation where $a, b, c \in \mathbb{R}$.

$$\vec{p}^i = \begin{bmatrix} a \\ b \\ c \end{bmatrix} = a \begin{bmatrix} 1 \\ 0 \\ 0 \end{bmatrix} + b \begin{bmatrix} 0 \\ 1 \\ 0 \end{bmatrix} + c \begin{bmatrix} 0 \\ 0 \\ 1 \end{bmatrix}. \tag{2.21}$$

The basis vectors used to represent point $\vec{p}^i$ with respect to reference frame i are thus conventionally $[1, 0, 0]^\top, [0, 1, 0]^\top$ and $[0, 0, 1]^\top$. Using these simple basis vectors as reference, the phrase *rotating a reference frame* is described as changing the orientation of each basis vector while preserving their magnitudes of 1, orthogonality and relative orientations. The orientation of a reference frame can be described by three angles of rotation, referred to as the Euler angles as in [43]. Conventionally, these refer to a rotation of the initial reference frame by a rotation around the $\hat{x}_i^i$ axis[1], then a rotation around the $\hat{y}_i^i$ axis followed by a rotation around the $\hat{z}_i^i$ axis. This is known as a *roll, pitch, yaw* or ZYX rotations [43]. These rotations are shown in Figure 2.1.

To rotate reference frame i by a certain angle θ_z around the $\hat{z}_i^i$ axis to yield reference frame j as in the left side of Figure 2.1, the basis vectors are transformed as follows to produce the basis vectors $\hat{x}_j$ with respect to i, $\hat{y}_j$ with respect to i and $\hat{z}_j$ with respect to

[1]The notation $\hat{x}_i^i$ represents the coordinates of the $\hat{x}_i$ basis vector of reference frame i with respect to reference frame i. Based on convention, $\hat{x}_i^i = [1, 0, 0]^\top \forall i$.

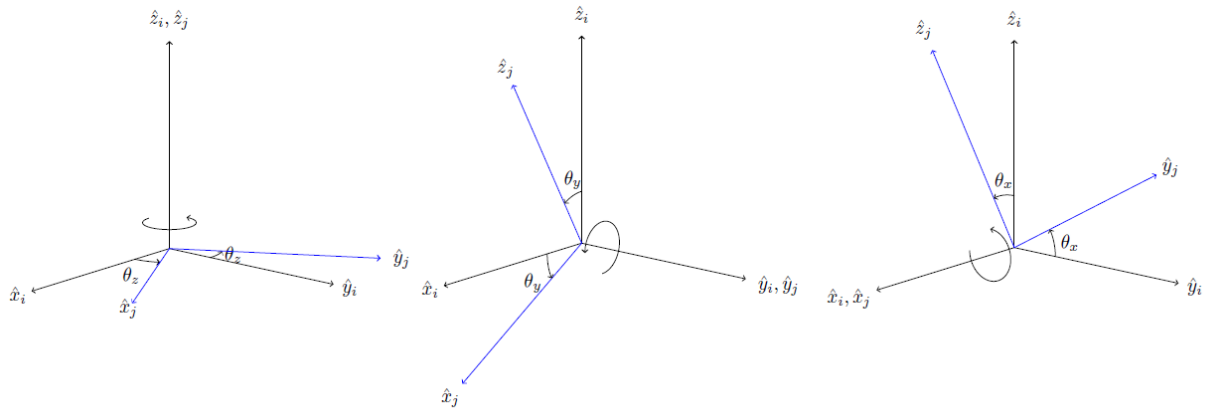

Figure 2.1: Rotations of reference frame i to yield reference frame j using the right-hand rule [43]. Left: rotating reference frame i around the $\hat{z}_i$ axis by an angle θ_z. Middle: rotating reference frame i around the $\hat{y}_i$ axis by an angle θ_y. Right: rotating reference frame i around the $\hat{x}_i$ axis by an angle θ_x.

i ($\hat{x}_j^i, \hat{y}_j^i$ and $\hat{z}_j^i$).

$$\hat{x}_i^i = \begin{bmatrix} 1 \\ 0 \\ 0 \end{bmatrix} \rightarrow \hat{x}_j^i = \begin{bmatrix} \cos\theta_z \\ \sin\theta_z \\ 0 \end{bmatrix} \tag{2.22}$$

$$\hat{y}_i^i = \begin{bmatrix} 0 \\ 1 \\ 0 \end{bmatrix} \rightarrow \hat{y}_j^i = \begin{bmatrix} -\sin\theta_z \\ \cos\theta_z \\ 0 \end{bmatrix} \tag{2.23}$$

$$\hat{z}_i^i = \begin{bmatrix} 0 \\ 0 \\ 1 \end{bmatrix} \rightarrow \hat{z}_j^i = \begin{bmatrix} 0 \\ 0 \\ 1 \end{bmatrix} \tag{2.24}$$

These vectors are derived using trigonometry where the magnitude of each basis vector is 1. Any point in space can then be represented by a linear combination of the new basis vectors of reference frame j, $\hat{x}_j^i$, $\hat{y}_j^i$ and $\hat{z}_j^i$, as follows for $d, e, f \in \mathbb{R}$.

$$\vec{p}^{\,i} = \begin{bmatrix} a \\ b \\ c \end{bmatrix} = d \begin{bmatrix} \cos\theta_z \\ \sin\theta_z \\ 0 \end{bmatrix} + e \begin{bmatrix} -\sin\theta_z \\ \cos\theta_z \\ 0 \end{bmatrix} + f \begin{bmatrix} 0 \\ 0 \\ 1 \end{bmatrix} = \begin{bmatrix} \cos\theta_z & -\sin\theta_z & 0 \\ \sin\theta_z & \cos\theta_z & 0 \\ 0 & 0 & 1 \end{bmatrix} \begin{bmatrix} d \\ e \\ f \end{bmatrix}. \tag{2.25}$$

The vector $[d, e, f]^\top$ is the position of the point $\vec{p}$ with respect to the reference frame j ($\vec{p}^{\,j}$). Therefore, the previous equation defines the rotation matrix for a rotation around

the $\hat{z}_i^i$ axis:

$$\vec{p}^{\,i} = \begin{bmatrix} \cos\theta_z & -\sin\theta_z & 0 \\ \sin\theta_z & \cos\theta_z & 0 \\ 0 & 0 & 1 \end{bmatrix} \vec{p}^{\,j} = \begin{bmatrix} & & \\ \hat{x}_j^i & \hat{y}_j^i & \hat{z}_j^i \\ & & \end{bmatrix} \vec{p}^{\,j} = \boldsymbol{R}_j^i \vec{p}^{\,j}. \tag{2.26}$$

For convenience, let this rotation matrix also be labelled $\boldsymbol{R}_z(\theta_z)$. Similarly, the new basis vectors for reference frame j after a rotation around the $\hat{y}_i^i$ axis as in the middle part of Figure 2.1 are:

$$\hat{x}_i^i = \begin{bmatrix} 1 \\ 0 \\ 0 \end{bmatrix} \rightarrow \hat{x}_j^i = \begin{bmatrix} \cos\theta_y \\ 0 \\ -\sin\theta_y \end{bmatrix} \tag{2.27}$$

$$\hat{y}_i^i = \begin{bmatrix} 0 \\ 1 \\ 0 \end{bmatrix} \rightarrow \hat{y}_j^i = \begin{bmatrix} 0 \\ 1 \\ 0 \end{bmatrix} \tag{2.28}$$

$$\hat{z}_i^i = \begin{bmatrix} 0 \\ 0 \\ 1 \end{bmatrix} \rightarrow \hat{z}_j^i = \begin{bmatrix} \sin\theta_y \\ 0 \\ \cos\theta_y \end{bmatrix} \tag{2.29}$$

This leads to the rotation matrix

$$\boldsymbol{R}_j^i = \boldsymbol{R}_y(\theta_y) = \begin{bmatrix} \cos\theta_y & 0 & \sin\theta_y \\ 0 & 1 & 0 \\ -\sin\theta_y & 0 & \cos\theta_y \end{bmatrix}. \tag{2.30}$$

Similarly when performing a rotation of θ_x around the $\hat{x}_i^i$ axis,

$$\boldsymbol{R}_j^i = \boldsymbol{R}_x(\theta_x) = \begin{bmatrix} 1 & 0 & 0 \\ 0 & \cos\theta_x & -\sin\theta_x \\ 0 & \sin\theta_x & \cos\theta_x \end{bmatrix}. \tag{2.31}$$

Rotation matrices can be multiplied together to yield a combined rotation matrix, a matrix composed of multiple rotation angles. To illustrate this, let there be two additional reference frames: k and l. Let j be rotated by θ_z around $\hat{z}_i^i$, k be rotated by θ_y around $\hat{y}_j^j$ and l be rotated by θ_x around $\hat{x}_k^k$. Then the following deduction can be made:

$$\vec{p}^{\,i} = \boldsymbol{R}_j^i \vec{p}^{\,j} = \boldsymbol{R}_j^i \boldsymbol{R}_k^j \vec{p}^{\,k} = \boldsymbol{R}_j^i \boldsymbol{R}_k^j \boldsymbol{R}_l^k \vec{p}^{\,l} = \boldsymbol{R}_z(\theta_z)\boldsymbol{R}_y(\theta_y)\boldsymbol{R}_x(\theta_x)\vec{p}^{\,l} = \boldsymbol{R}_l^i \vec{p}^{\,l}. \tag{2.32}$$

The combined rotation matrix $\boldsymbol{R}_l^i$ is a ZYX rotation matrix and has the following values, achieved by multiplying the three rotation matrices together.

$$\boldsymbol{R}_l^i = \boldsymbol{R}_l^i(\theta_x, \theta_y, \theta_z) = \boldsymbol{R}_z(\theta_z)\boldsymbol{R}_y(\theta_y)\boldsymbol{R}_x(\theta_x) \tag{2.33}$$

$$= \begin{bmatrix} \cos\theta_z \cos\theta_y & \cos\theta_z \sin\theta_y \sin\theta_x - \sin\theta_z \cos\theta_x & \cos\theta_z \sin\theta_y \cos\theta_x + \sin\theta_z \sin\theta_x \\ \sin\theta_z \cos\theta_y & \sin\theta_z \sin\theta_y \sin\theta_x + \cos\theta_z \cos\theta_x & \sin\theta_z \sin\theta_y \cos\theta_x - \cos\theta_z \sin\theta_x \\ -\sin\theta_y & \cos\theta_y \sin\theta_x & \cos\theta_y \cos\theta_x \end{bmatrix}. \tag{2.34}$$

2.2 Review of State-of-the-Art

This section overviews the latest theory relevant to the research topic of this thesis.

2.2.1 Point-Scatterer Model

Throughout this thesis, theoretical derivations are verified through MATLAB simulations by comparing the results obtained to simulation results obtained through the standard for complex target modelling: the point-scatterer model [8].

The point-scatterer model describes a complex target by a set of point-scatterers, each with their own Radar Cross Section (RCS). The RCS for a radar target is the projection of its effective reflective area onto the plane orthogonal to the vector from the transceiver to the target positioned on the target. The RCS depends on radar carrier frequency, aspect and elevation angles and varies significantly for even slight angle adjustments for complex targets. For evaluating the phase of the received signal for each of the point-scatterers, the result from equation (2.18) is used: namely that the signal is a delayed version of the transmit signal which has been Doppler-shifted by an amount proportional to the relative velocity between the monostatic transceiver and point-scatterer. The amplitude of the backscatter signal is proportional to the RRE of each point-scatterer, which include the point-scatterer's RCS. For P_s point-scatterers on a complex drone model, the backscatter received signal, represented by $\psi_{PS}(t)$, is given by

$$\psi_{PS}(t) = \psi_{PS}(P_{PS}(t)) = \sum_{p=0}^{P_s-1} \text{RRE}(\sigma_p(t), R_p^o) e^{j2\pi f_c (1+\frac{2||\vec{v}_{r,p}^o||}{c})(t-\frac{2R_p^o}{c})} \tag{2.35}$$

where σ_p is the pth point-scatterer RCS, $||\vec{v}_{r,p}^o||$ is the norm of the relative velocity between the transceiver and the point-scatterer w.r.t. the o reference frame and R_p^o is the relative

distance between the transceiver and the pth point-scatterer w.r.t. the o reference frame[2]. Notice the similarity between equations (2.35) and (2.18). The framework established in Chapter 3 can be used to define both where the point-scatterers are on the drone model and their velocities. In general, one point-scatterer can be placed at the center-of-mass of the drone and one point-scatterer can we placed at the tip of each blade on each propeller to model the complex drone target. The RCSs of the point-scatterers at the tip of the blades are going to be significantly smaller than the RCS of the static portion of the drone since the intention is to have one RCS at the center of the drone to represent the area due to all the bulk, non-rotating matter on the vehicle. The general time-dependent parameter set used to parameterize equation (2.35), $P_{PS}(t)$, is then the union of the time-dependent and time-independent parameters:

$$P_{1,PS}(t) = \{\sigma_p, ||\vec{v}^{\,o}_{r,p}||, R^o_p\}_{p=0}^{P-1} \tag{2.36}$$

$$P_{2,PS} = \{f_c\} \tag{2.37}$$

$$P_{PS}(t) = P_{1,PS}(t) \cup P_{2,PS} \tag{2.38}$$

where $P_{1,PS}(t)$ and $P_{2,PS}$ represent the time-dependent and time-independent parameters respectively.

In designing MATLAB simulations used for theoretical validation, reasonable RCS values are chosen $\forall p$ while relative distance and velocities are updated for each point-scatterer for all time samples in the simulations.

2.2.2 Martin-Mulgrew Model

The Martin-Mulgrew reflection model was first introduced in [30] and has since been used numerous times, for example in [13,15,36]. The initial model makes the important far-field approximation to achieve a closed-form solution for a complicated integral representing an expression for the radar backscatter signal from a jet engine. The model also makes several assumptions such as the blade being an infinitesimally thin reflective element and that the transceiver is at the same height as the propeller center (see [15, 30]).

[2]The relative distance magnitude is the same w.r.t. any reference frame but the distance vector itself varies depending on reference frame.

Parameter label	Description
A_r	A scale factor
L_1	Distance of the blade start to the center of the propeller (m)
L_2	Distance of the blade end to the center of the propeller (m)
N	Number of blades
R	Range of the center of rotation (m)
t	Time (s)
v	Radial velocity of the center of the propeller w.r.t. the transceiver (m/s)
λ	Wavelength of transmitted signal (m)
θ	Angle between the plane of rotation of the rotor and the plane containing the vector going from the transceiver to the propeller center (rad)
f_c	Carrier frequency of the transmitted signal (Hz)
ω_r	Angular frequency of rotation of the rotor (rad/s)

Table 2.1: Martin-Mulgrew parameter description

The model is presented as follows, as in [30], for a single rotor with N blades:

$$\psi(t) = \sum_{n=0}^{N-1} A_r(L_2 - L_1) \exp\left(j2\pi f_c t - \frac{j4\pi}{\lambda}\left(R + vt + \frac{L_1 + L_2}{2}\cos\theta \sin\left(\omega_r t + \frac{2\pi n}{N}\right)\right)\right) \cdot \operatorname{sinc}\left(\frac{4\pi(L_2 - L_1)}{2\lambda}\cos\theta \sin\left(\omega_r t + \frac{2\pi n}{N}\right)\right) \tag{2.39}$$

where all the variables are defined in Table 2.1. The model is thoroughly derived and augmented in several manners in Chapter 3.

2.2.3 OFDM Radar

OFDM radar is commonly used in literature for obtaining micro-Doppler signatures from varying different targets [10,11,25,27,32,35,41]. In general, OFDM provides several degrees of freedom to customize the radar transmit signal. It can be used in both active and passive radar and allows for Joint Communication Radar (JCR) or, equivalently, Integrated Sensing and Communication (ISAC) capabilities due to the ability to vary data symbols in both

time and frequency domains. In existing literature, simulations are usually constructed using the point-scatter model such that well positioned scatterers are used to build the complex target, whatever the target is. It has been shown a viable radar transmit signal whose system is capable of generating micro-Doppler signatures without having excessive transmit power and reasonable system losses.

In the literature deriving closed-form solutions for the radar backscatter using OFDM, rotating scatterers are usually used to substitute the position of each point-scatterer. The benefit of using the simulation method derived in this thesis is that the simulation allows *any* trajectory, topology, orientation, etc. For example, the simulator is not restricted to a certain movement pattern and can define their own, should they choose. OFDM radar can be either pulsed or Continuous Wave (CW) [45]. This thesis presents both cases but focuses on pulsed OFDM radar.

2.3 Relevant Research

This section enumerates the various sources of information relevant to the topic of this thesis.

2.3.1 OFDM Pulsed Radar and Integrated Sensing and Communication (ISAC)

Numerous sources develop theory regarding using the same transmission for both sensing (radar) and communications simultaneously. This is relevant to the research presented in this thesis because the simulation model developed herein allows an arbitrary OFDM symbol set for the transmit signal. The OFDM symbols can be chosen intelligently, such as in [2, 32, 46], to carry information while being used as a radar signal. OFDM pulsed radar has been shown to produce similar performance compared to traditional Linear Frequency Modulation (LFM) radar as in [17] while also being used to communication information reliably.

Other sources such as [24] disregard the communication component in favor of maximizing the radar performance based on the OFDM symbol set and modulations used. [39] uses the ambiguity function to quantify how good an OFDM radar signal is based on how close the ambiguity function resembles a thumb-tack response (Dirac-delta function in 2D).

In the approach used in this thesis, several pulses are expected to be transmitted to achieve a decent radar processing gain. However, in this source [51], range-Doppler imaging

is performed using a single pulse of a carefully chosen OFDM transmit signal. This could be tested by the resulting simulation tool shown in this thesis.

A common problem in OFDM pulsed radar is Inter-Carrier Interference (ICI) in the presence of the Doppler effect. Spectrum leakage may occur from one carrier to the next if the frequency of the received signal is shifted as a result of the Doppler effect. A way to mitigate this is presented here [21].

This source [4] also tackles the issue of blind range where the transmitter leaks into the receiver at a transceiver gNB/eNB base station and obscures the nearby target in the 5G NR and Long-Term Evolution (LTE) contexts. The ISAC topic is more generally overviewed in [49].

The 5G infrastructure can also be used passively as sources of illumination for passive radar as in [9]. These sources [5,6] make use of the localization signals known as Positioning Reference Signals (PRS) being transmitted in 5G to perform radar identification. [12] examines the current 5G NR standards and proposes some slight modification to enhance the radar capability through looking at ambiguity and cross-ambiguity functions.

General OFDM radars are common and have been used for target detection in multi-path scenarios [42]. OFDM radars are also common in driving safety applications so [26] investigates cross-vehicle interference by attempting to find subcarrier channels which have lower levels of ICI.

2.3.2 Micro-Doppler Signatures

The primary references for micro-Doppler signatures are from Dr. V.C. Chen as in [7, 8]. These show how rotating objects impart micro-Doppler signatures into radar signals. These as well as [47] (using wavelet transforms) show how helicopters, drones, humans, etc., generate their own micro-Doppler signatures hence they are an ideal dataset for target detection.

[48] elaborate how micro-Doppler signature generation is a valuable asset and present a low-cost option for simulating them for different objects by using time-domain digital coding metasurface. [23] show how micro-Doppler signatures can be used to detect humans walking among trees and perform inference based on the micro-Doppler data. Usefulness of the micro-Doppler signature is further emphasized in [35] and they show how inference is performed for the signatures in question.

2.3.3 Complex Radar Target Modeling

The current industry-standard for target modeling is the point-scatterer model as in [3, 8, 20] . There exists other ways to determine the expected backscatter signal however, for example, to assume a moving component scatters energy all across it as in the Martin-Mulgrew model [30].

For modeling UAVs specifically, [14, 19, 31] show that a small UAV could be viewed as a dynamic RCS for a radar target and does not consider its micro-Doppler characteristics. However, this approach could produce confusing results since birds can also fit into this category since they are aerial and of roughly the same size as some UAVs.

It is also possible to model the UAV more precisely as in [33] where the full 3D model for the exact drone is decomposed into significantly more point-scattering centers, becoming more precise at the cost of also becoming computationally intensive and requiring parallelization. Their algorithm also makes use of the Hidden Point Removal (HPR) [22] algorithm to essentially occlude any point-scatterer which is radially behind another scattering center from the radar.

Source [18] also concludes that there exists a middle-ground for radar dwell time to accurately collect micro-Doppler data and source [52] concludes that the different types of drones can be distinguished based on their signatures.

Chapter 3

Augmented Martin-Mulgrew Model

The Martin-Mulgrew model, initially presented in [30], quantifies the theoretical radar return signal from aircraft propeller blades. In the model, each propeller blade acts as an infinitesimal-width antenna which reflects radar signal. The closed-form expression is stated in equation (2.39). The original model takes into account the Doppler shift due to the bulk velocity of motion of the propeller, v, but not of the additional velocity due to the micro motions of the propeller blades. Only the positions of the blades are updated; the frequency is not modified to compensate. In addition, the model predicts the backscatter signal off the target for a single propeller and a single carrier. The purpose of this thesis includes making use of this model to predict backscatter signal of an entire drone, therefore, the Martin-Mulgrew model must be augmented to include these additional considerations.

3.1 Martin-Mulgrew Model Derivation

This paper [30] does not show the derivation of the model but only presents the model itself. The best source showing a derivation of the model currently available is in appendix E of [15].

The scenario described in appendix E of [15] is as follows. There is a transceiver radar at an arbitrary position. There is also an object, intended to represent the jet engine, composed of the combination of N separate blades. The N blades rotate around a center point which is also the center of the reference frame with basis vectors $\hat{x}_u$, $\hat{y}_u$ and $\hat{z}_u$. As is shown in Figure 3.1, the blades do not originate from the center of the reference frame but after a distance L_1. The length of the end of the blade from the center of the reference frame is L_2. Therefore, the length of each blade is $L_2 - L_1$.

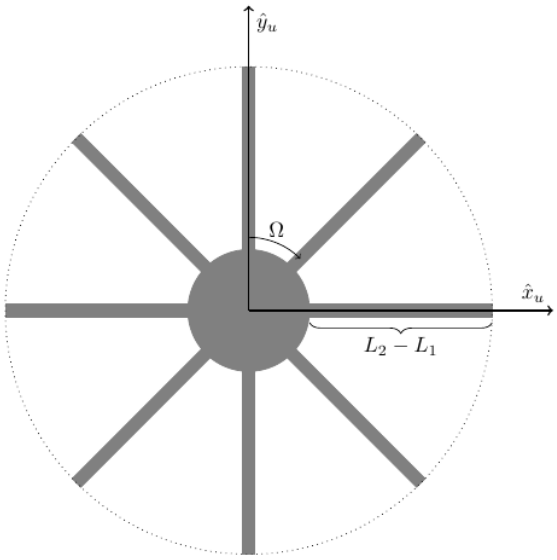

Figure 3.1: Simplified 2D diagram of the jet engine for $N = 8$.

Applying the same vectorization as in Section 2.1.1, the position vectors of the transceiver and the center of rotation respectively would be $\vec{x}_t$ and $\vec{x}_u$ with respect to an observing reference frame with basis vectors $\hat{x}_o$, $\hat{y}_o$, $\hat{z}_o$[1]. The [15] thesis states in a different manner that the vector $\vec{R}$ is the distance between these two positions; $\vec{R} = \vec{x}_t - \vec{x}_u$. The vector $\vec{r}(\alpha)$ as a function of some length $\alpha \in [L_1, L_2]$ is defined as the vector pointing along the blade from the origin of the propeller and $||\vec{r}(\alpha)|| = \alpha$, $\forall \alpha$. This is illustrated in Figure 3.2.

To quantify the magnitude of the $\vec{R} + \vec{r}(\alpha)$ vector, the following definition is used, as in [15]. Constructing triangles with the magnitudes results in what is shown in Figure 3.3.

$$||\vec{R} + \vec{r}(\alpha)|| := ||\vec{R}|| - \delta R(\alpha), \quad \delta R : \mathbb{R}^+ \to \mathbb{R} \tag{3.1}$$

In isolating a single one of these infinitesimal-width blade/antennas, the computation of the reflected signal is the combination of all the reflected signals along the antenna. [15] describes this as

$$\psi(R, t) = \int_{L_1}^{L_2} \frac{A(\alpha)}{R + \delta R(\alpha)} e^{2\pi j f_{Tx} - jk(R - \delta R(\alpha))} d\alpha \tag{3.2}$$

[1]The quantities $\vec{x}_t$ and $\vec{x}_u$ could also be written as $\vec{x}_t^o$ and $\vec{x}_u^o$ respectively to indicate that the two quantities are viewed w.r.t. the observer reference frame. When the superscript is omitted from the vector quantity, this means it is to be viewed from the observer.

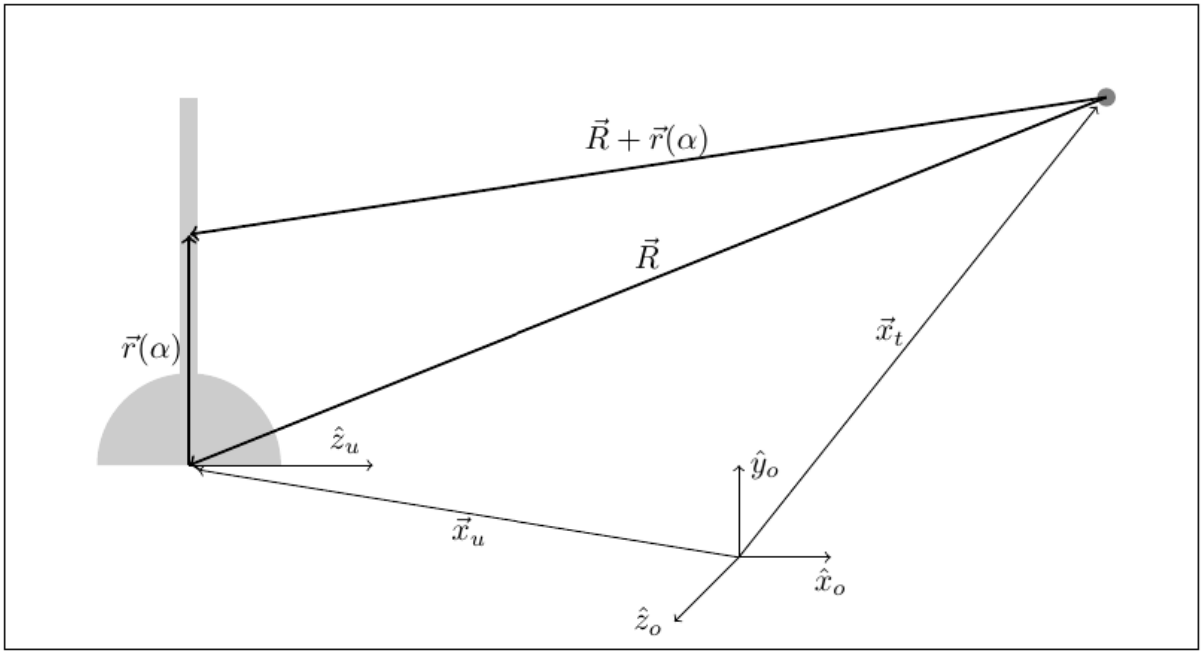

Figure 3.2: Vectors and reference frames

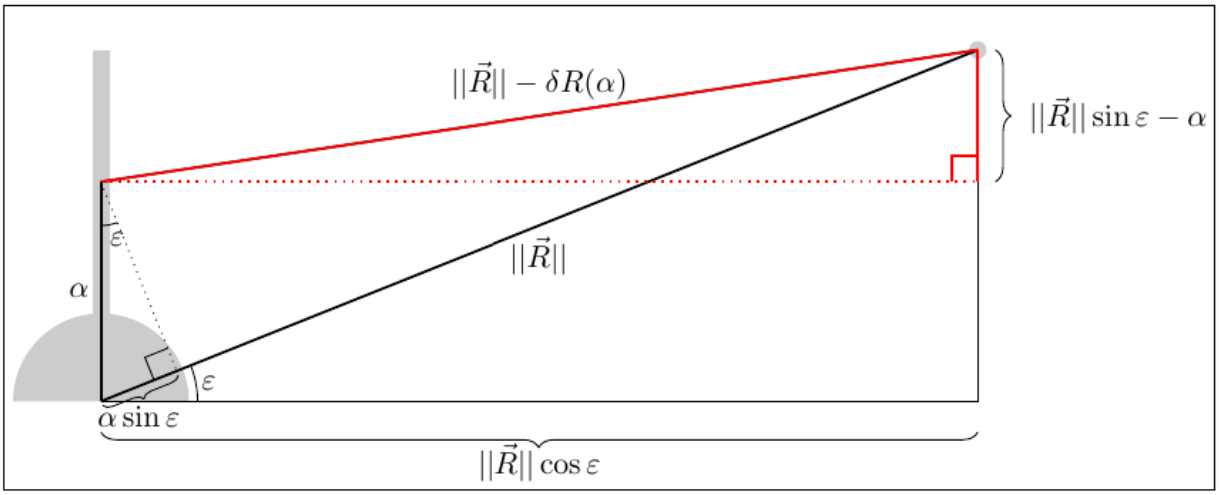

Figure 3.3: Magnitude triangle construction

where ψ is the reflected signal received by the transceiver as a function of the range of the object $R = ||\vec{R}||$ in the time domain, $f_{Tx} = f_c$ is the carrier frequency, $k = 2\pi/\lambda$ is referred to as the wave number and $A(\alpha)$ is the amplitude function of the reflected signal observed directly after it is reflected. Here, i is used as the imaginary unit instead of j to follow the author's convention in [15]. The function assumes that the magnitude of the signal received by the transceiver is inversely proportional to the distance between the reflected signal component and the transceiver $(R - \delta R(\alpha))^2$. Though this is approximately correct, it is actually inversely proportional to the square of the distance. For example, in the Free Space Path Loss model as in [16], the received power is modelled by

$$P_r = \frac{P_t}{4\pi R^2} \tag{3.3}$$

where P_r and P_t are the received and transmitted powers in Watts respectively. The standard form of RRE as in equation (2.19) includes R^4 in the denominator whereas the FSPL has an R^2 term. This is because the FSPL formula is one-way while the RRE includes the path-loss for the same distance twice as the radar signal is reflected off the target and returned to the transceiver.

To derive the exponential component in equation (3.2), let the antenna section at α be transmitting a signal proportional to $e^{2\pi j f_{Tx} t}$ in order to be received by the transceiver. To account for the phase differences of the different ranges $\forall \alpha \in [L_1, L_2]$, the signals are delayed based on the distance that the signal travels, $R - \delta R(\alpha)$. The time for light to travel a distance of $R - \delta R(\alpha)$ is $(R - \delta R(\alpha))/c$. Then the received signal is quantified by

$$\begin{aligned} & e^{2\pi j f_{Tx}(t - \frac{R - \delta R(\alpha)}{c})} \\ &= e^{2\pi j f_{Tx} t} e^{-2\pi j f_{Tx} \frac{R - \delta R(\alpha)}{c}} \\ &= e^{2\pi j f_{Tx} t} e^{-\frac{2\pi}{\lambda} j (R - \delta R(\alpha))} \\ &= e^{2\pi j f_{Tx} t - jk(R - \delta R(\alpha))}. \end{aligned}$$

A more general definition for the received signal is, using different variable conventions,

$$\psi(R, t) = \int_{L_1}^{L_2} \frac{A(\alpha)}{L(R - \delta R(\alpha))} e^{j2\pi f_c t - jk(R - \delta R(\alpha))} d\alpha \tag{3.4}$$

$$= \int_{L_1}^{L_2} \frac{A(\alpha)}{L(R - \delta R(\alpha))} e^{j2\pi f_c t} e^{-jkR} e^{jk\delta R(\alpha)} d\alpha \tag{3.5}$$

[2] In equation (3.2), $R + \delta R(\alpha)$ is used by the author however this is a mistake and should be $R - \delta R(\alpha)$. The function also incorrectly leaves out the t variable from the $e^{2\pi j f_{Tx}}$ component.

where $L(d) : \mathbb{R}^+ \to \mathbb{R}^+$ is the loss as a function of the distance in meters. Using the fact that the $\exp(j2\pi f_c t)$ and $\exp(-jkR)$ terms are independent of the distance along the blade α, the terms can be moved to the outside of the integral:

$$\psi(R,t) = e^{j2\pi f_c t} e^{-jkR} \int_{L_1}^{L_2} \frac{A(\alpha)}{L(R-\delta R(\alpha))} e^{jk\delta R(\alpha)} d\alpha. \tag{3.6}$$

To simplify the expression, Pythagoras is used on the red triangle in Figure 3.3:

$$(R-\delta R(\alpha))^2 = (R\sin\varepsilon - \alpha)^2 + (R\cos\varepsilon)^2. \tag{3.7}$$

This leads to the expression

$$R - \delta R(\alpha) = \sqrt{R^2 - 2\alpha R\sin\varepsilon + \alpha^2}. \tag{3.8}$$

Dividing both sides by R,

$$1 - \frac{\delta R(\alpha)}{R} = \sqrt{1 - \frac{2\alpha\sin\varepsilon}{R} + \frac{\alpha^2}{R^2}}. \tag{3.9}$$

The right-hand side has the form $(1+x)^a$ where

$$x = \frac{\alpha^2}{R^2} - \frac{2\alpha\sin\varepsilon}{R} \text{ and } a = \frac{1}{2}. \tag{3.10}$$

Labelling $(1+x)^a$ as the function $f(x)$ and using the MacLaurin series, the function is expressed by

$$f(x) = (1+x)^a = \sum_{n=0}^{\infty} \frac{f^{(n)}(0)}{n!} x^n \tag{3.11}$$

$$= 1 + ax + \frac{a(a-1)}{2}x^2 + ... \tag{3.12}$$

Taking the two most significant terms in the series, $f(x)$ can be approximated by $1+ax$. This MacLaurin series approximation can be referred to as *binomial approximation*. Using this approximation,

$$1 - \frac{\delta R(\alpha)}{R} \approx 1 + \frac{1}{2}\left(\frac{\alpha^2}{R^2} - \frac{2\alpha\sin\varepsilon}{R}\right). \tag{3.13}$$

Subtracting 1 from both sides and multiplying by $-R$,

$$\delta R(\alpha) \approx \alpha\sin\varepsilon - \frac{\alpha^2}{2R}. \tag{3.14}$$

Inserting the approximation into the expression for the reflected signal in equation (3.6) and simplifying,

$$\psi(R,t) \approx e^{j2\pi f_c t} e^{-jkR} \int_{L_1}^{L_2} \frac{A(\alpha)}{L(R - \alpha \sin\varepsilon + \frac{\alpha^2}{R^2})} e^{jk(\alpha \sin\varepsilon - \frac{\alpha^2}{2R})} d\alpha \tag{3.15}$$

$$\approx e^{j2\pi f_c t} e^{-jkR} \int_{L_1}^{L_2} \frac{A(\alpha)}{L(R(1 - \frac{\alpha \sin\varepsilon}{R} + \frac{\alpha^2}{R^3}))} e^{jk\alpha \sin\varepsilon} e^{-jk\frac{\alpha^2}{2R}} d\alpha. \tag{3.16}$$

At this point, an assumption is used that the distance between the propeller and the transceiver is much greater than the blade length: $R \gg \alpha, \forall\alpha \equiv R \gg L_2 - L_1$. This is known as the far-field approximation and it critical to computing a closed-form solution. With this assumption, the expression can be further simplified:

$$\psi(R,t) \approx e^{j2\pi f_c t} e^{-jkR} \int_{L_1}^{L_2} \frac{A(\alpha)}{L(R)} e^{jk\alpha \sin\varepsilon} d\alpha \tag{3.17}$$

$$\approx \frac{1}{L(R)} e^{j2\pi f_c t} e^{-jkR} \int_{L_1}^{L_2} A(\alpha) e^{jk\alpha \sin\varepsilon} d\alpha \tag{3.18}$$

Going back to using vector notation, the term $\alpha \sin\varepsilon$ can be represented as magnitude of the projection of $\vec{r}(\alpha)$ onto $\vec{R}$ and

$$-||\text{proj}_{\vec{R}} \vec{r}(\alpha)|| = -\vec{r}(\alpha) \cdot \frac{\vec{R}}{||\vec{R}||} = -\vec{r}(\alpha) \cdot \frac{\vec{R}}{R} = \alpha \sin\epsilon. \tag{3.19}$$

The minus sign is introduced because the vector $\vec{R}$ goes from the transceiver to the UAV and not the other way around. Therefore the exponent with $\alpha \sin\varepsilon$ can be rewritten in equation (3.18):

$$\psi(R,t) \approx \frac{1}{L(R)} e^{j2\pi f_c t} e^{-jkR} \int_{L_1}^{L_2} A(\alpha) e^{-jk\vec{r} \cdot \frac{\vec{R}}{R}} d\alpha \tag{3.20}$$

To further define the amplitude of the signal, the $A(\alpha)$ function can be quantified. The definition for this $A(\alpha)$ function is the amplitude of the signal arriving at the infinitesimal point α along the antenna (blade). The function has to modify the phase of the resulting signal based on the distance travelled from the transceiver to the UAV. Therefore, let

$$A(\alpha) = \frac{\psi_0}{L(R)} e^{-jk(R - \delta R(\alpha))} \tag{3.21}$$

where ψ_0 is the amplitude of the voltage of the signal leaving the transmitter. The loss function is present again because of its effect in both directions, forward and backwards. The exponential term is again the phase difference due to having the wave travel a distance of $R - \delta R(\alpha)$. Applying the MacLaurin series approximation for $\delta R(\alpha)$ as well as the approximation that $R \gg \alpha$,

$$A(\alpha) \approx \frac{\psi_0}{L(R)} e^{-jk(R-\alpha \sin\varepsilon + \frac{\alpha^2}{2R})} \tag{3.22}$$

$$\approx \frac{\psi_0}{L(R)} e^{-jk(R-\alpha \sin\varepsilon)}. \tag{3.23}$$

In vector form,

$$A(\alpha) \approx \frac{\psi_0}{L(R)} e^{-jk(R+\vec{r}\cdot\frac{\vec{R}}{R})}. \tag{3.24}$$

Replacing the amplitude value into the reflected signal equation yields

$$\psi(R,t) \approx \frac{1}{L(R)} e^{j2\pi f_c t} e^{-jkR} \int_{L_1}^{L_2} \frac{\psi_0}{L(R)} e^{-jk(R+\vec{r}\cdot\frac{\vec{R}}{R})} e^{-jk\vec{r}\cdot\frac{\vec{R}}{R}} d\alpha \tag{3.25}$$

$$\approx \frac{\psi_0}{L^2(R)} e^{j2\pi f_c t} e^{-jkR} e^{-jkR} \int_{L_1}^{L_2} e^{-jk\vec{r}\cdot\frac{\vec{R}}{R}} e^{-jk\vec{r}\cdot\frac{\vec{R}}{R}} d\alpha \tag{3.26}$$

$$\approx \frac{\psi_0}{L^2(R)} e^{j2\pi f_c t} e^{-j2kR} \int_{L_1}^{L_2} e^{-j2k\vec{r}\cdot\frac{\vec{R}}{R}} d\alpha \tag{3.27}$$

It's still not possible to evaluate the integral because the $\vec{r}$ vector is still depending on the value of α. Specifically, the $\vec{r}$ vector can be defined with respect to the UAV reference frame basis vectors $\hat{x}_u$, $\hat{y}_u$ and $\hat{z}_u$:

$$\vec{r} = \alpha \sin\Omega \hat{x}_u + \alpha \cos\Omega \hat{y}_u \tag{3.28}$$

where Ω is the orientation of the blade as in Figure 3.1. The integral then becomes

$$\int_{L_1}^{L_2} e^{-j2k\alpha(\sin\Omega\hat{x}_u + \cos\Omega\hat{y}_u)\cdot\frac{\vec{R}}{R}} d\alpha. \tag{3.29}$$

For convenience, let $\gamma = -2k(\sin\Omega\hat{x}_u + \cos\Omega\hat{y}_u)\cdot\frac{\vec{R}}{R}$. The integral can now be solved:

$$\int_{L_1}^{L_2} e^{j\alpha\gamma} d\alpha = \frac{1}{j\gamma}\left[e^{j\alpha\gamma}\right]_{L_1}^{L_2} = \frac{1}{j\gamma}(e^{jL_2\gamma} - e^{jL_1\gamma}) \tag{3.30}$$

The expression on the right-hand side looks like the expression

$$\sin\theta = \frac{1}{2j}(e^{j\theta} - e^{-j\theta}) \tag{3.31}$$

but not quite. Perhaps a multiplication by 1 can be done to the expression in order to make the angles match. Ideally, $\exists A, B \in \mathbb{R}$ such that

$$e^{j(L_2-A)\gamma} - e^{j(L_1-A)\gamma} = e^{jB\gamma} - e^{-jB\gamma}. \tag{3.32}$$

If that were true, then $L_2 - A = B$ and $L_1 - A = -B$. Adding these two equations together produces $L_2 + L_1 = 2A$; $A = (L_1 + L_2)/2$. Deducing the value of B based on the value of A produces $B = L_2 - (L_1 + L_2)/2$; $B = (L_2 - L_1)/2$. So indeed, this multiplication by 1 is possible to make the angles match:

$$\begin{aligned}
&\frac{1}{j\gamma}(e^{jL_2\gamma} - e^{jL_1\gamma}) \\
&= \frac{1}{j\gamma}(e^{jL_2\gamma} - e^{jL_1\gamma})\frac{e^{-jA\gamma}}{e^{-jA\gamma}} \\
&= \frac{1}{j\gamma e^{-jA\gamma}}(e^{j(L_2-A)\gamma} - e^{j(L_1-A)\gamma}) \\
&= \frac{1}{j\gamma e^{-jA\gamma}}(e^{jB\gamma} - e^{-jB\gamma}).
\end{aligned}$$

With this simplification, the identity in equation (3.31) can be used:

$$\begin{aligned}
\frac{1}{j\gamma e^{-jA\gamma}}(e^{jB\gamma} - e^{-jB\gamma}) &= \frac{1}{j\gamma e^{-jA\gamma}} 2j\sin(B\gamma) \\
&= \frac{2\sin\left(\frac{L_2-L_1}{2}\gamma\right)}{\gamma e^{-j(L_1+L_2)\gamma/2}} \\
&= \frac{2}{\gamma} e^{j(L_1+L_2)\gamma/2} \sin\left(\frac{L_2-L_1}{2}\gamma\right).
\end{aligned}$$

It is also possible to express this using the sinc function, whose definition is $\mathrm{sinc}(\theta) = \sin(\theta)/\theta$.

$$\mathrm{sinc}\left(\frac{L_2-L_1}{2}\gamma\right) = \sin\left(\frac{L_2-L_1}{2}\gamma\right)\frac{2}{(L_2-L_1)\gamma} \tag{3.33}$$

$$\therefore \frac{2}{\gamma} e^{j(L_1+L_2)\gamma/2} \sin\left(\frac{L_2-L_1}{2}\gamma\right) = (L_2-L_1) e^{j(L_1+L_2)\gamma/2} \mathrm{sinc}\left(\frac{L_2-L_1}{2}\gamma\right). \tag{3.34}$$

With the integral being evaluated, the reflected signal expression can be simplified to

$$\psi(R,t) \approx \frac{\psi_0}{L^2(R)} e^{j2\pi f_c t} e^{-j2kR} \left((L_2 - L_1) e^{j(L_1+L_2)\gamma/2} \text{sinc}(\frac{L_2 - L_1}{2}\gamma) \right) \tag{3.35}$$

$$\approx \frac{\psi_0 (L_2 - L_1)}{L^2(R)} e^{j2\pi f_c t} e^{-j2kR} e^{j(L_1+L_2)\gamma/2} \text{sinc}(\frac{L_2 - L_1}{2}\gamma). \tag{3.36}$$

This is the general form of the Martin-Mulgrew model for a single blade. The authors in [30] use additional assumptions to simplify the model further such as the center of rotation of the jet-engine being at the same height as the transceiver. These assumptions cannot be used here and the model is left general. Note that the authors in [30] also introduce Doppler shifting to their model subsequent to the insertion of additional assumptions. The general form of MM model as in equation (3.36) does not include any Doppler shifting properties.

In order to combine the result of the model from N separate blades spinning around the same center-of-rotation, the reflected signals are simply added together:

$$\psi(R,t) = \sum_{n=0}^{N-1} \psi_{(n)}(R,t) \tag{3.37}$$

where $\psi_{(n)}$ denotes the reflected signal result from the nth blade. Because a lot of the components in the equation are the same for all N blades, the expression can be simplified to

$$\psi(R,t) \approx \frac{\psi_0 (L_2 - L_1)}{L^2(R)} e^{j2\pi f_c t} e^{-j2kR} \sum_{n=0}^{N-1} e^{j(L_1+L_2)\gamma_n/2} \text{sinc}(\frac{L_2 - L_1}{2}\gamma_n) \tag{3.38}$$

assuming the blade length is the same for each blade. The variable γ_n differs for each blade because it depends on the blades' orientations:

$$\gamma_n = -2k(\sin\Omega_n \hat{x}_u + \cos\Omega_n \hat{y}_u) \cdot \frac{\vec{R}}{R} \tag{3.39}$$

where Ω_n represents the orientation of the nth blade. Note that each blade has the same reference frame with basis vectors $\hat{x}_u$, $\hat{y}_u$ and $\hat{z}_u$.

3.2 From Jet Engines to Drones

In order to modify the MM model from modelling the reflected signal from a single propeller to modelling the reflected signal off a drone which could include several propellers, all with

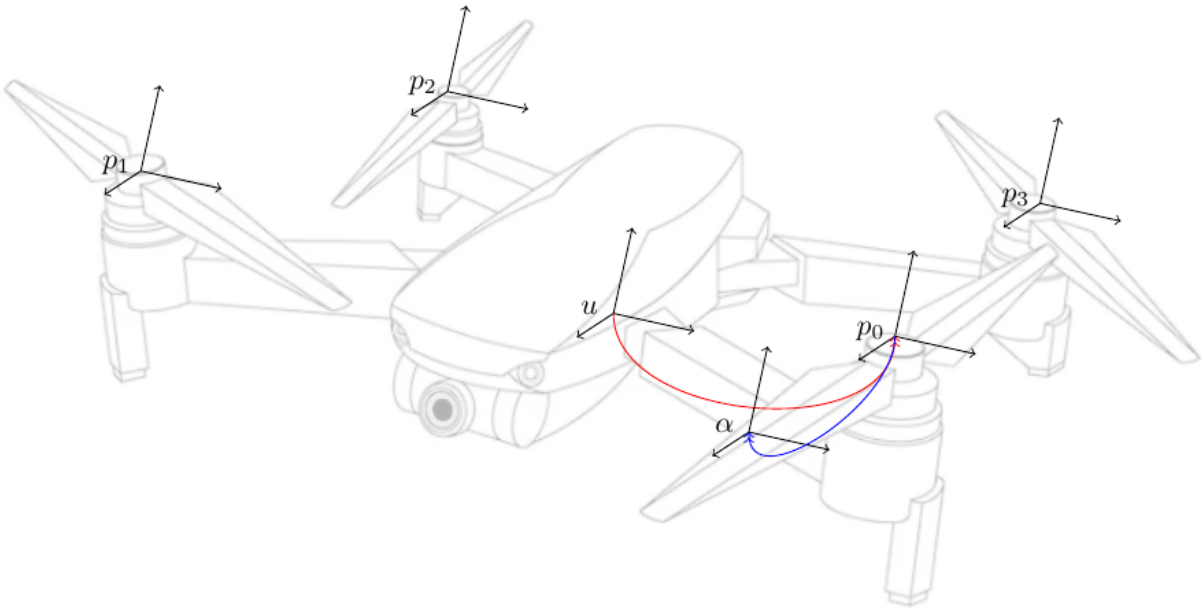

Figure 3.4: Example of reference frames introduced. Reference frame u is at the center-of-mass of the drone, reference frame p_i is at the center of the ith propeller and α along the blade of the propeller for the current value of $\alpha \in [L_1, L_2]$. The red and blue arcs represent the homogeneous transformation between the reference frames which can be accomplished through homogeneous transformation matrices [43].

their own orientations, rotational velocities, etc, additional reference frames are introduced. So far, the main reference frame that has been used to describe points in the world is the observer basis with vectors $\hat{x}_o$, $\hat{y}_o$ and $\hat{z}_o$ as in Figure 3.2. The UAV object in Section 3.1 is modelled as only a propeller as in Figure 3.1. In this section, the model for the UAV is as shown in Figure 3.4 where the UAV is composed of multiple propellers and non-rotating material.

Using the rotation matrix and this additional reference frame notation presented in Section 2.1.2, the $\vec{R}$ vector used in the MM model can be described more precisely in terms of the position of the ith propeller on the drone:

$$\vec{R} = \vec{x}^{\,o}_{p_i} - \vec{x}^{\,o}_{t} = \vec{x}^{\,o}_{u} + \boldsymbol{R}^{o}_{u}(\theta_x, \theta_y, \theta_z)\vec{x}^{\,u}_{p_i} - \vec{x}^{\,o}_{t} \tag{3.40}$$

where $\vec{x}^{\,o}_{p_i}$ is the position vector for the center of the propeller. This equation is useful because the position of the ith propeller is a constant with respect to the center-of-mass

reference frame u of the drone.

The range between the propeller center and the transceiver at a certain time depends only on the distance between the transceiver and the center-of-mass of the drone, the drone's orientation and the position of the transceiver.

The other value to be modified from the MM model is the γ_n value, described as

$$\gamma_n = -2k(\sin\Omega_n \hat{x}^o_{p_i} + \cos\Omega_n \hat{y}^o_{p_i}) \cdot \frac{\vec{R}}{||\vec{R}||}. \tag{3.41}$$

The basis vectors for the reference frame p_i with respect to the observer reference frame can also be described by rotation matrices:

$$\hat{x}^o_{p_i} = \boldsymbol{R}^o_u \boldsymbol{R}^u_{p_i} \hat{x}^{p_i}_{p_i} = \boldsymbol{R}^o_u \boldsymbol{R}^u_{p_i} \begin{bmatrix} 1 & 0 & 0 \end{bmatrix}^\top \tag{3.42}$$

$$\hat{y}^o_{p_i} = \boldsymbol{R}^o_u \boldsymbol{R}^u_{p_i} \hat{y}^{p_i}_{p_i} = \boldsymbol{R}^o_u \boldsymbol{R}^u_{p_i} \begin{bmatrix} 0 & 1 & 0 \end{bmatrix}^\top \tag{3.43}$$

$$\therefore \gamma_n(i,t) = -2k\left(\sin\Omega_n \boldsymbol{R}^o_u \boldsymbol{R}^u_{p_i} \begin{bmatrix} 1 \\ 0 \\ 0 \end{bmatrix} + \cos\Omega_n \boldsymbol{R}^o_u \boldsymbol{R}^u_{p_i} \begin{bmatrix} 0 \\ 1 \\ 0 \end{bmatrix} \right) \cdot \frac{\vec{R}}{R}. \tag{3.44}$$

The relative orientation from the center-of-mass u to the center of the ith propeller varies with each of the I propellers. Therefore γ_n depends on both time and which propeller is being analyzed, as $\vec{R}$ does.

To create a new model specific to multi-propeller UAVs, the original single-propeller version of the MM model as in equation (3.36) can be added together once for each propeller on the UAV and modified according to time, position and orientation. For $R(i,t) = ||\vec{R}(i,t)||$ and a general parameter set $P(t)$,

$$\begin{aligned}
\psi(P(t)) &\approx \sum_{i=0}^{I-1} \frac{\psi_0(L_2(i) - L_1(i))}{L^2(R(i,t))} e^{j2\pi f_c t} e^{-j2kR(i,t)} \\
&\quad \cdot \sum_{n=0}^{N_i-1} e^{j(L_1(i)+L_2(i))\gamma_n(i,t)/2} \mathrm{sinc}\left(\frac{L_2(i) - L_1(i)}{2} \gamma_n(i,t) \right) \\
&\approx \psi_0 e^{j2\pi f_c t} \sum_{i=0}^{I-1} \frac{L_2(i) - L_1(i)}{L^2(R(i,t))} e^{-j2kR(i,t)} \\
&\quad \cdot \sum_{n=0}^{N_i-1} e^{j(L_1(i)+L_2(i))\gamma_n(i,t)/2} \mathrm{sinc}\left(\frac{L_2(i) - L_1(i)}{2} \gamma_n(i,t) \right).
\end{aligned} \tag{3.45}$$

This allows for the possibility of having a different number of blades for each propeller by using N_i instead of N. The variables of the model which are time-dependent are the distance between the transceiver and center of each propeller, $R(i,t)$, and $\gamma_n(i,t)$. Based on the expressions for these two variables, the set composed of all the parameters required for evaluation, $P(t)$, is the union of a set of parameters which depend on t, $P_1(t)$, and the set of parameters which do not depend on t, P_2:

$$P_1(t) = \{\vec{x}_u^{\,o}, \vec{x}_t^{\,o}, \boldsymbol{R}_u^o\} \cup \{\{\Omega_n(i)\}_{n=0}^{N_i-1}, \vec{x}_{p_i}^{\,u}, \boldsymbol{R}_{p_i}^u\}_{i=0}^{I-1} \tag{3.46}$$

$$P_2 = \{\psi_0, f_c\} \cup \{L_1(i), L_2(i), N_i\}_{i=0}^{I-1} \tag{3.47}$$

$$P(t) = P_1(t) \cup P_2 \tag{3.48}$$

The far-field approximation that $\vec{x}_{p_i}^{\,u} \approx \vec{0} \because R \gg ||\vec{x}_{p_i}^{\,u}||$ could be used to shorten the set of parameters and simplify the model. The number of blades for each propeller could be assumed to be the same value as the drone is likely to use multiple of the same propeller instead of different propellers. The blade lengths of the different propellers are also likely to be the same length. This could be formulated into another assumption that simplifies the expression because when this is true, $(L_1(i) = L_1(0)) \wedge (L_2(i) = L_2(0)) \forall i$. These two additional constraints could simplify the model to the following expression.

$$\begin{aligned}\psi(P(t)) \approx & \psi_0 e^{j2\pi f_c t - j2kR(t)} \frac{L_2 - L_1}{L^2(R(t))} \\ & \cdot \sum_{i=0}^{I-1} \sum_{n=0}^{N-1} e^{j(L_1+L_2)\gamma_n(i,t)/2} \text{sinc}\left(\frac{L_2 - L_1}{2}\gamma_n(i,t)\right)\end{aligned} \tag{3.49}$$

This expression in equation (3.49) does allow for some simplification compared to equation (3.45) but the double-summation still exists over the terms with γ_n included which still contains the rotation matrices. The slight simplification does not justify the removal of generalization in the author's opinion therefore the constraints are not implemented moving forward.

3.3 Augmenting the Martin-Mulgrew Model with micro-Doppler Signatures

The term micro-Doppler is used to refer to the change in the reflected signal due to velocities which are "in addition to the bulk translation of an object" [7]. The micro-Doppler signature originates from secondary motion of the object. In the case of the drone, the

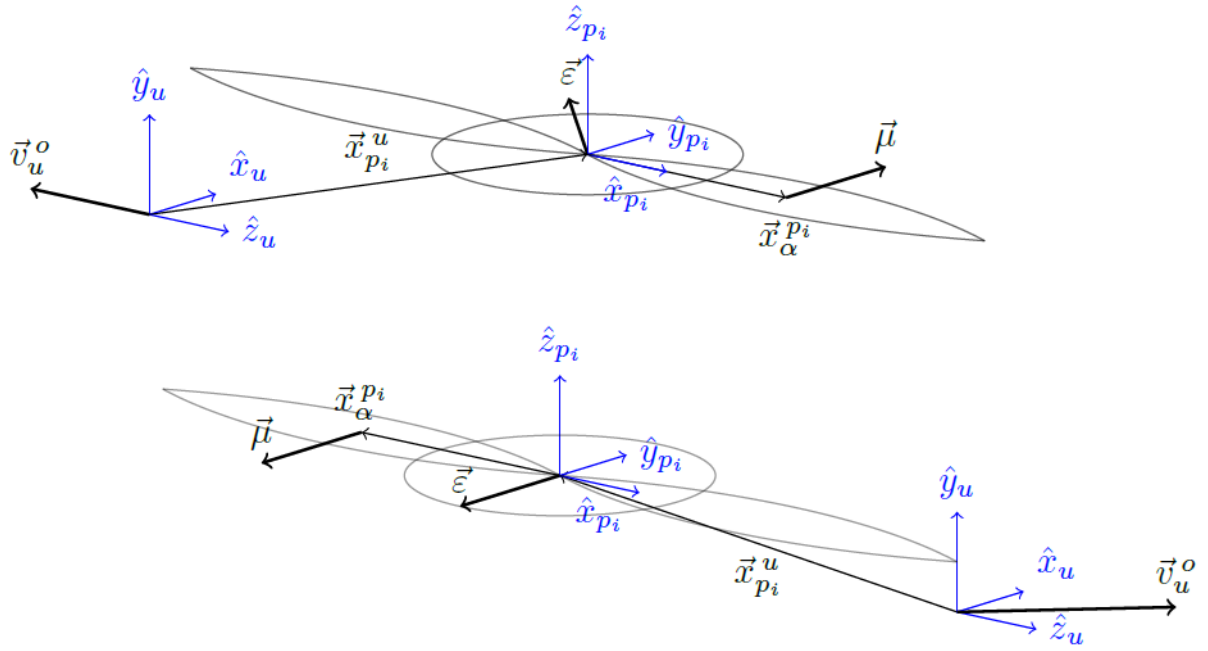

Figure 3.5: This is a display of a drone's reference frames along with the different velocities associated to a single point α along one of the ith propeller's blades for two different scenarios (top and bottom). The two reference frames displayed in blue in both top and bottom, u and p_i, are the reference frames associated with the drone's center of mass (u) and the center of the ith propeller (p_i). Arbitrary velocities were chosen for the center of mass of the drone while the velocities $\vec{\varepsilon}$ and $\vec{\mu}$ are in a fixed direction but were chosen to be displayed in a *positive* direction.

secondary motion is due mainly to the rotation of the propellers but also due to the rotation of the drone around its center of mass. Specifically, let the primary velocity—the velocity due to the total movement of the drone—be denoted $\vec{v}_u^{\,o}$. Let the velocity of the ith propeller due to the rotation of the propeller around the center of mass of the UAV be denoted $\vec{\varepsilon}$ and the velocity at a distance of α along one of the propeller blades on the ith propeller due to the blade's rotation around the center of the propeller be labelled $\vec{\mu}$. Two possibilities for these three velocities are displayed in Figure 3.5. Using these three different velocity vectors, the total velocity along a distance α of one of the blades on the ith propeller is

$$\vec{v}_{\alpha}^{\,o} = \vec{v}_u^{\,o} + \vec{\varepsilon}^{\,o} + \vec{\mu}^{\,o}. \tag{3.50}$$

In order to quantify the velocity vectors $\vec{\varepsilon}$ and $\vec{\mu}$, some important observations must be made.

Firstly, for the $\vec{\varepsilon}$ velocity, based on the pose (position and orientation) of the u reference frame and that the rotation causing the velocity is only happening around the $\hat{y}_u$ basis vector, the velocity's y component is equal to zero with respect to u. In other words,

$$ {}_y\varepsilon^u = 0 \tag{3.51}$$

where the writing convention is introduced that subscripts preceding the variable indicate one of the variable's vector components. The vector notation arrow is also removed since the variable is now a scalar.

The second observation to be made about $\vec{\varepsilon}^u$ is that it is orthogonal to the position vector for the center of the ith propeller in u's reference frame;

$$ \vec{\varepsilon}^u \perp \vec{x}^{\,u}_{p_i} \quad \equiv \quad \vec{\varepsilon}^u \cdot \vec{x}^{\,u}_{p_i} = 0. \tag{3.52}$$

This is true because the center of the propeller only moves in a circle around the center-of-mass of the drone, corresponding to reference frame u.

Thirdly, the magnitude of this velocity is proportional to its rotation frequency around the center-of-mass of the drone. If the drone rotates its propellers around its center of mass with rotation frequency of f_ε and has a distance of d_{p_i} from the $\hat{y}_u$ axis for the ith propeller, then the propeller travels a distance of $2\pi d_{p_i}$ meters per cycle at a frequency of f_ε cycles per second. Multiplying the two thus yields the magnitude of the velocity,

$$ ||\vec{\varepsilon}^u|| = 2\pi f_\varepsilon d_{p_i}. \tag{3.53}$$

Similar observations are made for the velocity $\vec{\mu}$ around p_i. Namely, in the same order as presented above,

$$ {}_z\mu^{p_i} = 0, \tag{3.54}$$

$$ \vec{\mu}^{\,p_i} \perp \vec{x}^{\,p_i}_{\alpha} \quad \equiv \quad \vec{\mu}^{\,p_i} \cdot \vec{x}^{\,p_i}_{\alpha} = 0 \text{ and} \tag{3.55}$$

$$ ||\vec{\mu}^{\,p_i}|| = 2\pi f_{rot,i}\alpha \tag{3.56}$$

where $f_{rot,i}$ is the rotational frequency of the propeller as in other articles on the same topic such as [13][3]. Notice that the magnitude of $\vec{\mu}^{\,p_i}$ depends on α while the magnitude of $\vec{\varepsilon}^u$ does not. The contribution of $\vec{\varepsilon}^u$ is the same $\forall \alpha \in [L_1, L_2]$. These observations may be made more clear through Figure 3.6.

[3]These authors assume the rotational frequency is the same for all propellers, hence they only use f_{rot}, however it is left general here to allow the option to model different propeller frequencies hence the '$,i$' appended to the subscript.

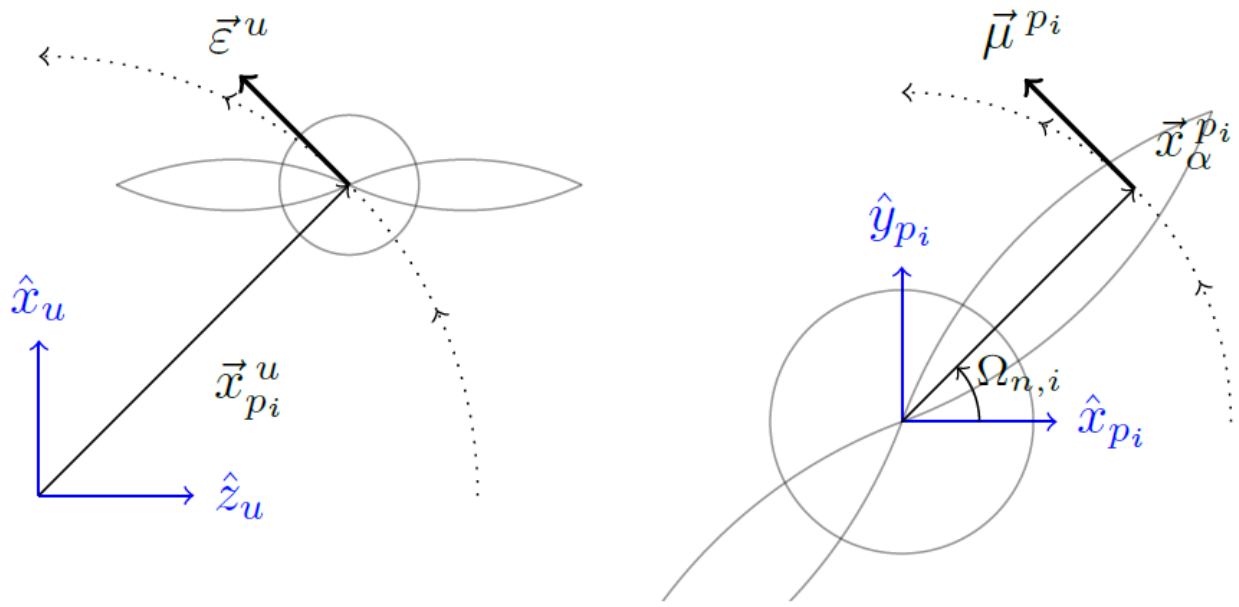

Figure 3.6: The left side displays the propeller rotating around the $\hat{y}_u$ axis with velocity $\vec{\varepsilon}^{\,u}$. The right side displays the propeller blade rotating around the $\hat{z}_{p_i}$ axis. Both of these diagrams are in 2D because the hidden-axis components of both velocities displayed are null with respect to each reference frame.

To quantify $\vec{\varepsilon}^{u}$ in terms of known (or assumed to be known) parameters, the observations in equations (3.51), (3.52) and (3.53) are used. Along with these observations, d_{p_i}, defined to be the shortest distance of the point $\vec{x}^{\,u}_{p_i}$ away from the $\hat{y}_u$ axis, can be expressed as the magnitude of $\vec{x}^{\,u}_{p_i}$ where the y component is set to zero. In other words,

$$d_{p_i} = \sqrt{({}_{x}x^{u}_{p_i})^2 + ({}_{z}x^{u}_{p_i})^2}. \tag{3.57}$$

Firstly, combining (3.51) and (3.52) leads to

$${}_{x}\varepsilon^{u}\ {}_{x}x^{u}_{p_i} +_{z} \varepsilon^{u}\ {}_{z}x^{u}_{p_i} = 0. \tag{3.58}$$

Isolating for the x component of the velocity,

$${}_{x}\varepsilon^{u} = -\frac{{}_{z}\varepsilon^{u}\ {}_{z}x^{u}_{p_i}}{{}_{x}x^{u}_{p_i}}. \tag{3.59}$$

Second, combining equations (3.53) and (3.57) and squaring both sides,

$$\begin{aligned} ||\vec{\varepsilon}^{u}|| &= 2\pi f_{\varepsilon}\sqrt{({}_{x}x^{u}_{p_i})^2 + ({}_{z}x^{u}_{p_i})^2} \\ ({}_{x}\varepsilon^{u})^2 + ({}_{z}\varepsilon^{u})^2 &= (2\pi f_{\varepsilon})^2\big(({}_{x}x^{u}_{p_i})^2 + ({}_{z}x^{u}_{p_i})^2\big). \end{aligned} \tag{3.60}$$

By substituting the value of ${}_{x}\varepsilon^{u}$ for the one found in equation (3.59),

$$\begin{aligned} \left(-\frac{{}_{z}\varepsilon^{u}\ {}_{z}x^{u}_{p_i}}{{}_{x}x^{u}_{p_i}}\right)^2 + ({}_{z}\varepsilon^{u})^2 &= (2\pi f_{\varepsilon})^2\big(({}_{x}x^{u}_{p_i})^2 + ({}_{z}x^{u}_{p_i})^2\big) \\ ({}_{z}\varepsilon^{u})^2\left(1 + \frac{({}_{z}x^{u}_{p_i})^2}{({}_{x}x^{u}_{p_i})^2}\right) &= (2\pi f_{\varepsilon})^2\big(({}_{x}x^{u}_{p_i})^2 + ({}_{z}x^{u}_{p_i})^2\big) \\ ({}_{z}\varepsilon^{u})^2 &= \frac{(2\pi f_{\varepsilon})^2\big(({}_{x}x^{u}_{p_i})^2 + ({}_{z}x^{u}_{p_i})^2\big)}{1 + \frac{({}_{z}x^{u}_{p_i})^2}{({}_{x}x^{u}_{p_i})^2}} \cdot \frac{({}_{x}x^{u}_{p_i})^2}{({}_{x}x^{u}_{p_i})^2} \\ ({}_{z}\varepsilon^{u})^2 &= (2\pi f_{\varepsilon}\ {}_{x}x^{u}_{p_i})^2\frac{({}_{x}x^{u}_{p_i})^2 + ({}_{z}x^{u}_{p_i})^2}{({}_{x}x^{u}_{p_i})^2 + ({}_{z}x^{u}_{p_i})^2} \\ \therefore\ {}_{z}\varepsilon^{u} &= \pm 2\pi f_{\varepsilon}\ {}_{x}x^{u}_{p_i}. \end{aligned} \tag{3.61}$$

Substituting the expression found into equation (3.59) leads to

$${}_{x}\varepsilon^{u} = \mp 2\pi f_{\varepsilon}\ {}_{z}x^{u}_{p_i}. \tag{3.62}$$

From the two expressions found for the velocity components, it is reasonable that the two components have opposing signs since for example in the first quadrant where ${}_{x}x^{u}_{p_i} \geq 0 \wedge {}_{z}x^{u}_{p_i} \geq 0$ as in the left side of Figure 3.6, if the velocity is counter-clockwise, then the x component is negative or 0 and the y component is positive or 0. The $\pm$ and $\mp$ signs in the expressions for the components of $\vec{\varepsilon}^{u}$ account for both possibilities: the velocity going clockwise and counter-clockwise.

Based on standard mathematical convention, a rotation in the counter-clockwise direction is chosen to represent the positive values for both velocities $\vec{\varepsilon}$ and $\vec{\mu}$. Therefore,

$$\vec{\varepsilon}^{u} = 2\pi f_{\varepsilon} \begin{bmatrix} -{}_{z}x^{u}_{p_i} \\ 0 \\ {}_{x}x^{u}_{p_i} \end{bmatrix}. \tag{3.63}$$

To verify that the signs make sense intuitively, the expression can be evaluated in the different quadrants:

$$(1) \quad {}_{x}x^{u}_{p_i} > 0 \wedge {}_{z}x^{u}_{p_i} > 0 \implies {}_{x}\varepsilon^{u} < 0 \wedge {}_{z}\varepsilon^{u} > 0 \tag{3.64}$$
$$(2) \quad {}_{x}x^{u}_{p_i} < 0 \wedge {}_{z}x^{u}_{p_i} > 0 \implies {}_{x}\varepsilon^{u} < 0 \wedge {}_{z}\varepsilon^{u} < 0 \tag{3.65}$$
$$(3) \quad {}_{x}x^{u}_{p_i} < 0 \wedge {}_{z}x^{u}_{p_i} < 0 \implies {}_{x}\varepsilon^{u} > 0 \wedge {}_{z}\varepsilon^{u} < 0 \tag{3.66}$$
$$(4) \quad {}_{x}x^{u}_{p_i} > 0 \wedge {}_{z}x^{u}_{p_i} < 0 \implies {}_{x}\varepsilon^{u} > 0 \wedge {}_{z}\varepsilon^{u} > 0 \tag{3.67}$$

Moving on to the velocity caused by the rotation of the propeller blades around the center of the propeller, $\vec{\mu}^{\,p_i}$. The same process can be repeated which was used to determine the expressions for the components of $\vec{\varepsilon}^{u}$ to yield

$${}_{y}\mu^{p_i} = \pm 2\pi f_{rot,i}\, {}_{x}x^{p_i}_{\alpha} \tag{3.68}$$
$${}_{x}\mu^{p_i} = \mp 2\pi f_{rot,i}\, {}_{y}x^{p_i}_{\alpha} \tag{3.69}$$

Because the same convention is used that positive velocity corresponds to counter-clockwise movement,

$$\vec{\mu}^{p_i} = 2\pi f_{rot,i} \begin{bmatrix} -{}_{y}x^{p_i}_{\alpha} \\ {}_{x}x^{p_i}_{\alpha} \\ 0 \end{bmatrix}. \tag{3.70}$$

$\vec{\mu}^{p_i}$ can also be expressed in terms of α based on the angle $\Omega_{n,i}$ which is the angle of the

point $\vec{x}_\alpha^{\,p_i}$ around the $\hat{z}_{p_i}$ axis[4]. Using this, the point $\vec{x}_\alpha^{\,p_i}$ can be expressed by

$$\vec{x}_\alpha^{\,p_i} = \alpha \begin{bmatrix} \cos\Omega_{n,i} \\ \sin\Omega_{n,i} \\ 0 \end{bmatrix} \quad \therefore \quad \vec{\mu}^{p_i} = 2\pi f_{rot,i}\alpha \begin{bmatrix} -\sin\Omega_{n,i} \\ \cos\Omega_{n,i} \\ 0 \end{bmatrix}. \tag{3.71}$$

Putting these three velocities together as in equation (3.50), the total velocity of a single point α along the nth blade of the ith propeller is given by

$$\vec{v}_\alpha^{\,o} = \vec{v}_u^{\,o} + \boldsymbol{R}_u^o \vec{\varepsilon}^{\,u} + \boldsymbol{R}_u^o \boldsymbol{R}_{p_i}^u \vec{\mu}^{\,p_i} \tag{3.72}$$

$$= \vec{v}_u^{\,o} + 2\pi f_\varepsilon \boldsymbol{R}_u^o \begin{bmatrix} -{}_z x_{p_i}^u \\ 0 \\ {}_x x_{p_i}^u \end{bmatrix} + 2\pi f_{rot,i}\alpha \boldsymbol{R}_u^o \boldsymbol{R}_{p_i}^u \begin{bmatrix} -\sin\Omega_{n,i} \\ \cos\Omega_{n,i} \\ 0 \end{bmatrix}. \tag{3.73}$$

The velocity to which the Doppler shift applies is the relative velocity between the point α along the blade and the transceiver. As in equations (2.2) through (2.5), the relative velocity is given by

$$\vec{v}_r^{\,o} = \text{proj}_{\vec{x}_\alpha^{\,o} - \vec{x}_t^{\,o}} \vec{v}_\alpha^{\,o} - \text{proj}_{\vec{x}_\alpha^{\,o} - \vec{x}_t^{\,o}} \vec{v}_t^{\,o} = \text{proj}_{\vec{x}_\alpha^{\,o} - \vec{x}_t^{\,o}} (\vec{v}_\alpha^{\,o} - \vec{v}_t^{\,o}) \tag{3.74}$$

$$= (\vec{v}_\alpha^{\,o} - \vec{v}_t^{\,o}) \cdot (\vec{x}_\alpha^{\,o} - \vec{x}_t^{\,o}) \frac{\vec{x}_\alpha^{\,o} - \vec{x}_t^{\,o}}{||\vec{x}_\alpha^{\,o} - \vec{x}_t^{\,o}||^2} \tag{3.75}$$

$$= \frac{(\vec{v}_\alpha^{\,o} - \vec{v}_t^{\,o}) \cdot (\vec{x}_\alpha^{\,o} - \vec{x}_t^{\,o})}{||\vec{x}_\alpha^{\,o} - \vec{x}_t^{\,o}||} \frac{\vec{x}_\alpha^{\,o} - \vec{x}_t^{\,o}}{||\vec{x}_\alpha^{\,o} - \vec{x}_t^{\,o}||}. \tag{3.76}$$

In this expression, $\vec{v}_r^{\,o}$ is decomposed into the form $\vec{v}_r^{\,o} = m\vec{d}$ where m is the magnitude of the vector and d is the direction vector whose magnitude is 1. Therefore,

$$||\vec{v}_r^{\,o}|| = \frac{(\vec{v}_\alpha^{\,o} - \vec{v}_t^{\,o}) \cdot (\vec{x}_\alpha^{\,o} - \vec{x}_t^{\,o})}{||\vec{x}_\alpha^{\,o} - \vec{x}_t^{\,o}||}. \tag{3.77}$$

For notational simplification, let $\vec{v}_\alpha^{\,o} - \vec{v}_t^{\,o} = \vec{h} + \alpha\vec{q}$ and $\vec{D} = \vec{x}_\alpha^{\,o} - \vec{x}_t^{\,o}$. Then the magnitude

[4]Note that the angle $\Omega_{n,i}$ is different than the angle Ω_n defined previously as in Figure 3.1. Specially, $\Omega_{n,i} = \frac{\pi}{2} - \Omega_n(i)$. This redefinition is done so that the angle is defined w.r.t. standard rotational conventions.

of the relative velocity can also be expressed as

$$||\vec{v}_r^{\,o}|| = (\vec{h} + \alpha\vec{q}) \cdot \frac{\vec{D}}{||\vec{D}||} = \vec{h} \cdot \frac{\vec{D}}{||\vec{D}||} + \alpha\vec{q} \cdot \frac{\vec{D}}{||\vec{D}||} \tag{3.78}$$

$$\text{where } \vec{h} = \vec{v}_u^{\,o} + 2\pi f_\varepsilon \boldsymbol{R}_u^o \begin{bmatrix} -_z x_{p_i}^u \\ 0 \\ {}_x x_{p_i}^u \end{bmatrix} - \vec{v}_t^{\,o} \tag{3.79}$$

$$\text{and } \vec{q} = 2\pi f_{rot,i} \boldsymbol{R}_u^o \boldsymbol{R}_{p_i}^u \begin{bmatrix} -\sin\Omega_{n,i} \\ \cos\Omega_{n,i} \\ 0 \end{bmatrix}. \tag{3.80}$$

With the magnitude of the relative velocity fully quantified, it is time to apply it to the original expression for the computation of the MM model for a single blade on a single propeller as in equation (3.5) by using what was derived in equation (2.18). This new model makes micro-Doppler considerations on top of the original model. Let it be expressed by ψ_d as follows

$$\psi_d = \int_{L_1}^{L_2} \frac{\psi_0}{L^2(||\vec{D}||)} e^{j2\pi f_c (1+2\frac{||\vec{v}_r^{\,o}||}{c})(t-\frac{2||\vec{D}||}{c})} d\alpha. \tag{3.81}$$

Note that this expression considers both transmitted and reflected signal attenuation and phase shifting at once instead of leaving it general with the illumination function $A(\alpha)$ as in equation (3.5) and then having to substitute for the variable.

The function can be expanded to form the following

$$\psi_d = \psi_0 e^{j2\pi f_c t} \int_{L_1}^{L_2} \frac{1}{L^2(D)} e^{-j4\pi f_c D/c} e^{j4\pi f_c \frac{||\vec{v}_r^{\,o}||}{c} t} e^{-j8\pi f_c \frac{||\vec{v}_r^{\,o}||}{c^2} D} d\alpha \tag{3.82}$$

where $D = ||\vec{D}||$. This integral looks intimidating due to the fact all the terms depend on α. In order to simplify this integral to allow it to be analytically solvable, the far-field approximation is used so that the distance between the points $\vec{x}_\alpha^{\,o}$ and $\vec{x}_t^{\,o}$ is roughly equal to the distance between the center of propeller and the transceiver[5]. In other words $\vec{D} \approx \vec{R}$ where $\vec{R} = \vec{x}_{p_i}^{\,o} - \vec{x}_t^{\,o}$. Using this approximation, the expression becomes

$$\psi_d \approx \psi_0 e^{j2\pi f_c t} \int_{L_1}^{L_2} \frac{1}{L^2(R)} e^{-j4\pi f_c R/c} e^{j4\pi f_c \frac{||\vec{v}_r^{\,o}||}{c} t} e^{-j8\pi f_c \frac{||\vec{v}_r^{\,o}||}{c^2} R} d\alpha \tag{3.83}$$

$$\approx \frac{\psi_0 e^{j2\pi f_c t} e^{-j4\pi f_c R/c}}{L^2(R)} \int_{L_1}^{L_2} e^{j4\pi f_c \frac{||\vec{v}_r^{\,o}||}{c} t} e^{-j8\pi f_c \frac{||\vec{v}_r^{\,o}||}{c^2} R} d\alpha. \tag{3.84}$$

[5]This approximation is later revised as a better approximation presents itself through numerical assessment.

The expression for $||\vec{v}_r^{\,o}||$ as in equation (3.78) can then be used to substitute for its value:

$$\psi_d \approx \frac{\psi_0 e^{j2\pi f_c t} e^{-j4\pi f_c R/c}}{L^2(R)} \int_{L_1}^{L_2} e^{j4\pi f_c (\vec{h}+\alpha\vec{q})\cdot\frac{\vec{R}}{R} t c^{-1}} e^{-j8\pi f_c (\vec{h}+\alpha\vec{q})\cdot\frac{\vec{R}}{R} R c^{-2}} d\alpha \tag{3.85}$$

$$\approx \ldots \int_{L_1}^{L_2} e^{j4\pi f_c \vec{h}\cdot\frac{\vec{R}}{R} t c^{-1}} e^{j4\pi f_c \alpha\vec{q}\cdot\frac{\vec{R}}{R} t c^{-1}} e^{-j8\pi f_c \vec{h}\cdot\vec{R} c^{-2}} e^{-j8\pi f_c \alpha\vec{q}\cdot\vec{R} c^{-2}} d\alpha \tag{3.86}$$

$$\approx \frac{\psi_0 e^{j2\pi f_c t} e^{-j4\pi f_c R/c}}{L^2(R)} e^{j4\pi f_c \vec{h}\cdot\frac{\vec{R}}{R} t c^{-1}} e^{-j8\pi f_c \vec{h}\cdot\vec{R} c^{-2}} \cdot \int_{L_1}^{L_2} e^{j4\pi f_c \alpha\vec{q}\cdot\frac{\vec{R}}{R} t c^{-1}} e^{-j8\pi f_c \alpha\vec{q}\cdot\vec{R} c^{-2}} d\alpha \tag{3.87}$$

$$\approx \frac{\psi_0 e^{j2\pi f_c t} e^{-j4\pi f_c R/c}}{L^2(R)} e^{j4\pi f_c c^{-1}(\vec{h}\cdot\frac{\vec{R}}{R})(t-\frac{2R}{c})} \int_{L_1}^{L_2} e^{j4\pi f_c \alpha c^{-1}(\vec{q}\cdot\frac{\vec{R}}{R})(t-\frac{2R}{c})} d\alpha \tag{3.88}$$

$$\approx \frac{\psi_0 e^{j2\pi f_c t} e^{-j4\pi f_c R/c}}{L^2(R)} e^{j4\pi f_c c^{-1}(\vec{h}\cdot\frac{\vec{R}}{R})(t-\frac{2R}{c})} \int_{L_1}^{L_2} e^{jl\alpha} d\alpha \tag{3.89}$$

where $l = 4\pi f_c c^{-1}(\vec{q}\cdot\frac{\vec{R}}{R})(t-\frac{2R}{c})$. Using the same process as equations (3.30) through (3.34), the integral is evaluated to yield:

$$\psi_d \approx \frac{\psi_0 e^{j2\pi f_c t} e^{-j4\pi f_c R c^{-1}}}{L^2(R)} e^{j4\pi f_c c^{-1}(\vec{h}\cdot\frac{\vec{R}}{R})(t-\frac{2R}{c})} (L_2 - L_1) e^{j(L_1+L_2)l/2} \mathrm{sinc}\left(\frac{L_2 - L_1}{2} l\right). \tag{3.90}$$

Note the similarity between equations (3.36) and (3.90). The difference (not literally) between the two is the inclusion of the $e^{j4\pi f_c c^{-1}(\vec{h}\cdot\frac{\vec{R}}{R})(t-\frac{2R}{c})}$ term and using l instead of γ.

To calculate the value of the signal reflected from all the blades, the expression is added I times for I propellers and N_i times for the number of blades on the ith propeller:

$$\psi_{dc} \approx \sum_{i=0}^{I-1} \sum_{n=0}^{N_i-1} \frac{\psi_0 e^{j2\pi f_c t} e^{-j4\pi f_c R c^{-1}}}{L^2(R)} e^{j4\pi f_c c^{-1}(\vec{h}\cdot\frac{\vec{R}}{R})(t-\frac{2R}{c})} \cdot (L_2(i) - L_1(i)) e^{j(L_1(i)+L_2(i))l/2} \mathrm{sinc}\left(\frac{L_2(i) - L_1(i)}{2} l\right) \tag{3.91}$$

In order to simplify the expression for ψ_{dc}, dependency of the variables must be established. First, R depends on the location of the center of the ith propeller so R depends on i. A subscript i is introduced here on the variable to indicate that it is dependent on i. It however does not depend on n because it remains the same for all blades on one propeller.

The first simplification can be made:

$$\psi_{dc} \approx \psi_0 e^{j2\pi f_c t} \sum_{i=0}^{I-1} \frac{e^{-j4\pi f_c R_i c^{-1}}}{L^2(R_i)} \sum_{n=0}^{N_i-1} e^{j4\pi f_c c^{-1}(\vec{h}\cdot\frac{\vec{R}_i}{R_i})(t-\frac{2R_i}{c})} \cdot (L_2(i)-L_1(i)) e^{j(L_1(i)+L_2(i))l/2} \text{sinc}\left(\frac{L_2(i)-L_1(i)}{2}l\right) \tag{3.92}$$

Next, the terms $L_2(i)$ and $L_1(i)$ are both assumed to be independent of n though that is not necessarily the case. Additionally, from the expression for $\vec{h}$ given in equation (3.79), it is concluded that $\vec{h}$ is dependent of i, due to the $\vec{x}^u_{p_i}$ components, but independent of n. Therefore, the expression can be slightly simplified to

$$\psi_{dc}(P_{dc}(t)) \approx \psi_0 e^{j2\pi f_c t} \sum_{i=0}^{I-1} \frac{(L_2(i)-L_1(i)) e^{-j4\pi f_c R_i c^{-1}}}{L^2(R_i)} e^{j4\pi f_c c^{-1}(\vec{h}\cdot\frac{\vec{R}_i}{R_i})(t-\frac{2R_i}{c})} \cdot \sum_{n=0}^{N_i-1} e^{j(L_1(i)+L_2(i))l/2} \text{sinc}\left(\frac{L_2(i)-L_1(i)}{2}l\right). \tag{3.93}$$

$\vec{q}$ however still depends on n because of the $\Omega_{n,i}$ term included as in equation (3.80). Since l depends on $\vec{q}$, it also depends on both i and n. Therefore, equation (3.93) is the final form of the model for this section where the argument is the parameter set $P_{dc}(t)$. As with the non-Doppler version of the model, the parameter set is decomposed into two separate sets; one which is dependent on t, $P_{1,dc}(t)$, and another parameter set which isn't, $P_{2,dc}$. The full parameter set dependent on t, $P_{dc}(t)$, is their union:

$$P_{1,dc}(t) = \{\vec{x}^o_u, \vec{x}^o_t, \boldsymbol{R}^o_u, f_\varepsilon, \vec{v}^o_u\} \cup \{\{\Omega_{n,i}\}_{n=0}^{N_i-1}, \vec{x}^u_{p_i}, \boldsymbol{R}^u_{p_i}, f_{rot,i}\}_{i=0}^{I-1} \tag{3.94}$$

$$P_{2,dc} = \{\psi_0, f_c\} \cup \{L_1(i), L_2(i), N_i\}_{i=0}^{I-1} \tag{3.95}$$

$$P_{dc}(t) = P_{1,dc}(t) \cup P_{2,dc} \tag{3.96}$$

3.3.1 Proving that propeller velocities do not fully cancel

One might think intuitively that the velocities due to the propeller rotation always has an equal and opposite velocity in two propeller blades that are π radians apart as in Figure 3.7 and therefore the effect of the velocity on the resulting echo signal is cancelled. However, this is an incorrect conclusion. This is proved here.

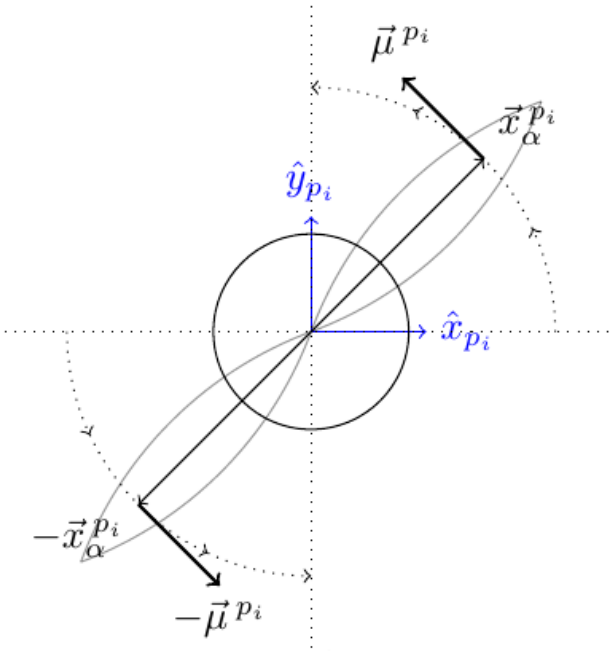

Figure 3.7: Opposing velocities in a propeller.

To begin, the echo signal resulting from the infinitesimal length $d\alpha$ at the origin of the ith propeller is modelled (omitting the "w.r.t. p_i" superscript for notational simplicity) as

$$\psi = d\alpha \frac{\psi_0}{L^2(R)} e^{2\pi f_c (1+2v_r c^{-1})(t-2Rc^{-1})} \tag{3.97}$$

with all the previously used variables. Adding two of these echo signals resulting from the infinitesimal length along the blade, both at the origin of the reference frame—the center of the propeller, and at a relative velocity where both of these echo signal components have $\vec{\mu} = \vec{0}$, thus $v_r = -\vec{v}_t \cdot \frac{\vec{R}}{R}$,

$$\psi_{\mu=0} = 2d\alpha \frac{\psi_0}{L^2(R)} e^{2\pi f_c (1-2(\vec{v}_t \cdot \frac{\vec{R}}{R})c^{-1})(t-2Rc^{-1})}. \tag{3.98}$$

When $\mu > 0$, the magnitude of the relative velocity is calculated as

$$v_1 = (\vec{v}_\alpha - \vec{v}_t) \cdot \frac{\vec{R}}{R} = \vec{\mu} \cdot \frac{\vec{R}}{R} - \vec{v}_t \cdot \frac{\vec{R}}{R}. \tag{3.99}$$

For an equal and opposite μ value, the relative velocity magnitude is

$$v_2 = -\vec{\mu} \cdot \frac{\vec{R}}{R} - \vec{v_t} \cdot \frac{\vec{R}}{R} \tag{3.100}$$

so if the two velocities are added together, the μ components are cancelled leaving only $-2\vec{v_t} \cdot \vec{R}R^{-1}$. However, if the two echo signals are added together,

$$\begin{aligned}
\psi_{\mu>0} = \quad & d\alpha \frac{\psi_0}{L^2(R)} e^{2\pi f_c(1+2v_1c^{-1})(t-2Rc^{-1})} \\
& + d\alpha \frac{\psi_0}{L^2(R)} e^{2\pi f_c(1+2v_2c^{-1})(t-2Rc^{-1})} \\
= \quad & d\alpha \frac{\psi_0}{L^2(R)} e^{2\pi f_c(t-2Rc^{-1})} e^{4\pi f_c v_1 c^{-1}(t-2Rc^{-1})} \\
& + d\alpha \frac{\psi_0}{L^2(R)} e^{2\pi f_c(t-2Rc^{-1})} e^{4\pi f_c v_2 c^{-1}(t-2Rc^{-1})} \\
= \quad & d\alpha \frac{\psi_0}{L^2(R)} e^{2\pi f_c(t-2Rc^{-1})} \left(e^{4\pi f_c v_1 c^{-1}(t-2Rc^{-1})} + e^{4\pi f_c v_2 c^{-1}(t-2Rc^{-1})}\right).
\end{aligned}$$

Let $a = 4\pi f_c c^{-1}(t - Rc^{-1})$ be a temporary variable. Then

$$\begin{aligned}
\psi_{\mu>0} &= d\alpha \frac{\psi_0}{L^2(R)} e^{2\pi f_c(t-2Rc^{-1})} \left(e^{av_1} + e^{av_2}\right) \\
&= d\alpha \frac{\psi_0}{L^2(R)} e^{2\pi f_c(t-2Rc^{-1})} e^{-av_t \cdot \frac{\vec{R}}{R}} \left(e^{a\mu} + e^{-a\mu}\right) \\
&= d\alpha \frac{\psi_0}{L^2(R)} e^{2\pi f_c(t-2Rc^{-1})(1-2c^{-1}\vec{v}_t \cdot \frac{\vec{R}}{R})} \left(2\cos\left(4\pi f_c c^{-1}(t-2Rc^{-1})\vec{\mu} \cdot \frac{\vec{R}}{R}\right)\right) \\
&= \psi_{\mu=0} \cos\left(4\pi f_c c^{-1}(t-2Rc^{-1})\vec{\mu} \cdot \frac{\vec{R}}{R}\right).
\end{aligned} \tag{3.101}$$

Because $\psi_{\mu=0} \neq \psi_{\mu>0} \wedge \psi_{\mu=0} \neq 0$, the velocities do not cancel in the echo signal model even though the velocities due to the propellers' rotations cancel each other.

3.3.2 Fourier Analysis of Backscatter Signal

The RCS for any object is a function of carrier frequency of the radar system, aspect and elevation angles. For complex objects, the RCS varies drastically from variations in all

three of these dependencies. For this reason, the RCS is often model in a statistically random manner. Swerling models are used to accomplish this [37].

This noisy RCS phenomenon causes significant distortion when performing signal analysis on backscatter signals, specifically on both the amplitude and phase of the signal. To be clear, amplitude and phase are defined for a complex number c as $|A|$ and θ respectively in $c = |A|e^{j\theta}$.

The component of the signal that remains consistent through these fluctuations is the frequency. This motivates performing frequency analysis on the returning signal. The radar reference book [37] uses the terminology coherent and non-coherent analysis to describe when the returning signal's phase is taken into consideration and when it is not, respectively, in the radar processing. For this analysis, coherent processing must be used as most of the information of the time-domain signal is contained in the phase of the signal due to the micro-Doppler signatures from the complex model.

The Continuous-Time Fourier Transform (CTFT) $X(j\omega)$ for a signal $x(t)$ where ω is the radial frequency is defined as [34]

$$X(j\omega) = \int_{-\infty}^{\infty} x(t)e^{-j\omega t}dt, \quad -\infty < \omega < \infty. \tag{3.102}$$

To describe the backscatter signal in the frequency-domain $\psi_{dc}(j\omega)$ analytically, the following integral would have to be solved:

$$\Psi_{dc}(j\omega) = \int_{-\infty}^{\infty} \psi_{dc}(P_{dc}(t))e^{-j2\pi f_c t}dt. \tag{3.103}$$

Due to the complexity of the expression for ψ_{dc} as in equation (3.93) and the numerous dependencies on time t, it is unrealistic to expect to solve this analytically. Hence the approach of the Discrete-Time Fourier Transform (DTFT) is taken where the discrete-time frequency domain representation for the backscatter signal $\Psi_{dc}(e^{j\omega})$ is given by

$$\Psi_{dc}(e^{j\omega}) = \sum_{n=-\infty}^{\infty} \psi_{dc}[n]e^{-j\omega n}, \quad \psi_{dc}[n] = \psi_{dc}(P_{dc}(t))\big|_{t=nT}, \quad T = f_s^{-1}. \tag{3.104}$$

$\psi_{dc}[n]$ is the discrete-time backscatter signal evaluated at the nth time sample, T is the sampling period and f_s is the sampling frequency. The sampling frequency is usually required to be at least two times the highest frequency in the signal being analysed as in the Nyquist sampling theorem, however, since narrowband sampling can be performed on this signal due to the micro-Doppler effect only modifying the frequencies local to

the carrier (also referred to as the micro-Doppler band), the sampling frequency can be drastically reduced. The necessary step required to enable this is a demodulation from the carrier frequency to baseband. This is done by multiplying the signal by $e^{-j2\pi f_c t}$ to shift the resulting signal back to being centered around 0 Hz:

$$\psi_b[n] = \left(\psi_{dc}(P_{dc}(t))e^{-j2\pi f_c t}\right)\Big|_{t=nT} \tag{3.105}$$

$$\Psi_b(e^{j\omega}) = \sum_{n=-\infty}^{\infty} \psi_b[n]e^{-j\omega n}. \tag{3.106}$$

The sampling frequency then should only be large enough to account for the signal bandwidth; $f_s \geq BW$. An example of this narrowband sampling is shown here for illustration. In this example, a signal with a bandwidth of 1 kHz is modulated on a carrier frequency of 10 kHz. The frequency spectrum is plotted in Figure 3.8. In order to be able to reconstruct this signal from its discrete-time samples, a sampling frequency needs to be greater than twice the maximum frequency. In general, for a signal modulated on some carrier, $f_s \geq 2(f_c + BW/2)$. For this particular signal,

$$f_s \geq 2(10 + 0.5) \text{ kHz} = 21 \text{ kHz}. \tag{3.107}$$

However, when multiplying a time-domain signal by $e^{j\omega_0 n}$ for some radial frequency ω_0, the following result appears, using the definition of the DTFT in equation (3.104):

$$\begin{aligned} y[n] &= e^{j\omega_0 n}x[n] \\ Y(e^{j\omega}) &= \sum_{n=-\infty}^{\infty} y[n]e^{-j\omega n} \\ &= \sum_{n=-\infty}^{\infty} e^{j\omega_0 n}x[n]e^{-j\omega n} \\ &= \sum_{n=-\infty}^{\infty} x[n]e^{-j(\omega-\omega_0)n} = X(e^{j(\omega-\omega_0)}). \end{aligned} \tag{3.108}$$

In other words, the multiplication of the signal by $e^{j\omega_0 n}$ in the time-domain has the effect of shifting the signal in the frequency-domain. This is known as demodulation. In this example, the signal is multiplied by $e^{-j2\pi f_c t}$ to shift the frequency-domain of the signal to baseband. This is shown in Figure 3.9. In reapplying the Nyquist sampling theorem to the demodulated signal, the maximum frequency is now just $BW/2$ and therefore a sampling

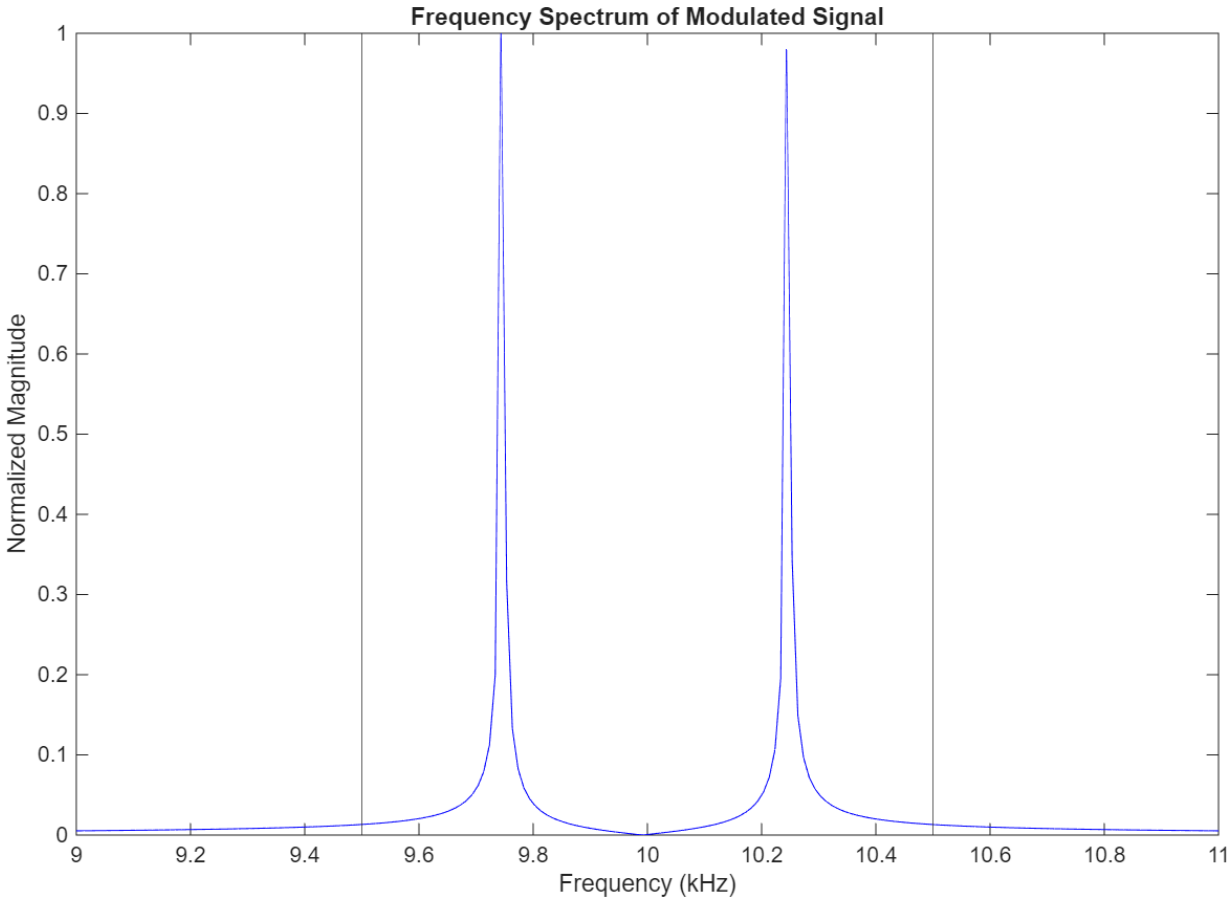

Figure 3.8: Frequency spectrum of an example signal being modulated on a carrier frequency. The black vertical lines indicate where the bandwidth starts and ends.

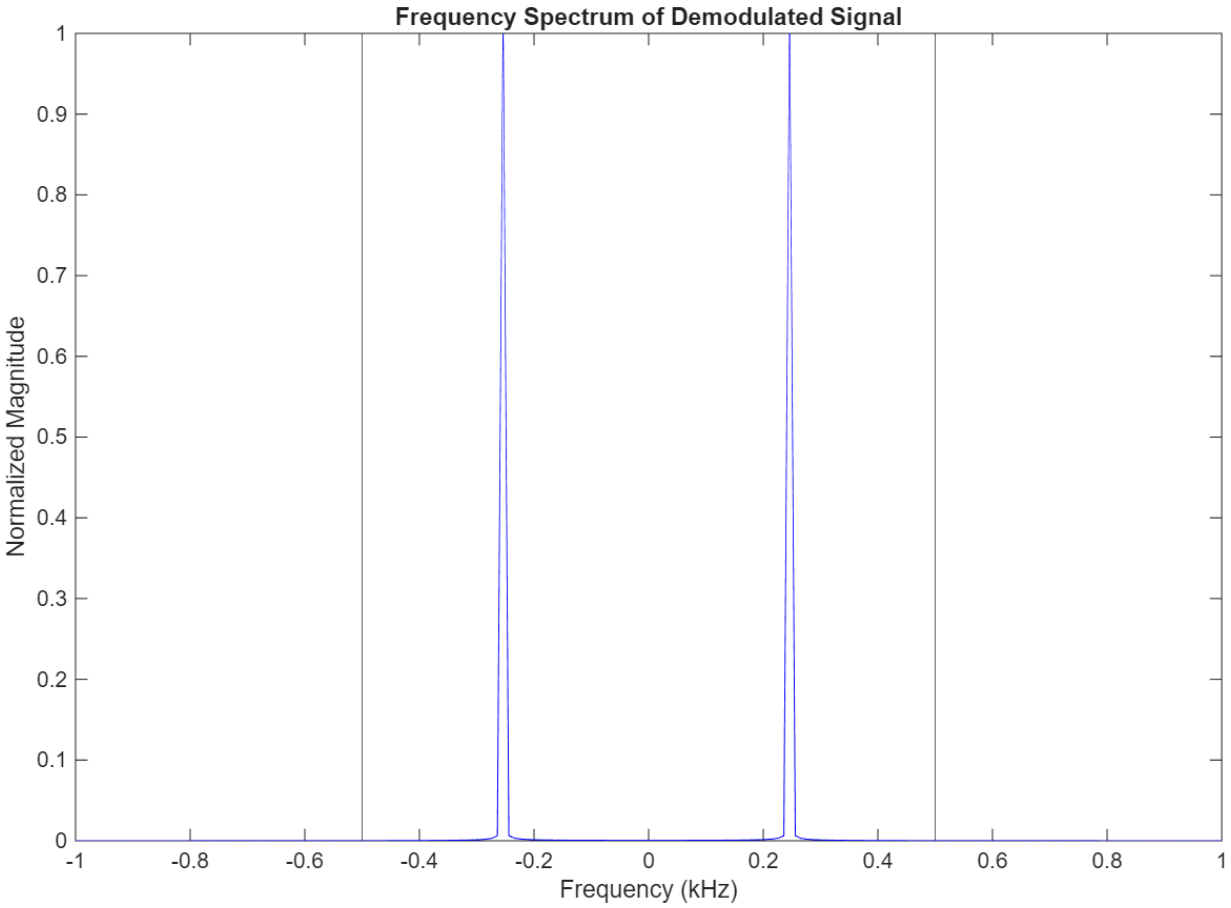

Figure 3.9: Frequency spectrum of an example signal being modulated on a carrier frequency after demodulation. The black vertical lines indicate where the bandwidth starts and ends.

frequency $f_s = BW = 1$ kHz can be used. Compared to the original required 21 kHz, this is a significant reduction in the number of samples required to reconstruct the original signal.

Due to the micro-Doppler adjustments to the backscatter signal, the bandwidth will increase to account for both forward and backward velocities of the UAV propellers. It can be expected that the minimum and maximum frequencies defining the bandwidth to be proportional to the velocity of the propellers. Using equation (2.14), the bandwidth of the signal can be set to

$$BW = \frac{2f_c||\vec{v}||}{c} - \frac{-2f_c||\vec{v}||}{c} \tag{3.109}$$

$$= \frac{4f_c||\vec{v}||}{c} \tag{3.110}$$

where $||\vec{v}||$ is the magnitude of the maximum velocity of the drone's propellers. The BW can always be increased or reduced depending on experimental results. The DTFT of the signal can be calculated efficiently with the Fast Fourier Transform (FFT) algorithm.

3.3.3 Experimental Validation of Theory

In this section, a simulation is presented which displays how the theory developed thus far predicts the micro-Doppler signal alterations on the carrier wave caused by the signal reflecting off complex drone-like objects.

The intention of the simulation is to construct a scenario where a sinusoidal carrier signal at a frequency of 20 GHz is transmitted from a transmitter at the origin through an isotropic antenna, reflected off of the complex target model at a distance of 100m from the origin and received by the mono-static transceiver at the origin. During the data collection process, the drone is only hovering off the ground while its propellers are rotating at maximum rotational frequency of 20k Rotations Per Minute (RPM). In other words, the position of the drone's center-of-mass is constant for the duration of the experiment. Because the theory so far has only covered the complex target model's propellers, there will be no static RCS; only the moving parts of the drone are simulated. The number of scattering centers which are used to model the propellers is varied under the variable name N_{scat} and differences examined. The complex drone model used is displayed in Figure 3.10 and the parameters of the experiment are listed in Table 3.1. This experiment uses Swerling model 2 for all scatterers in this experiment.

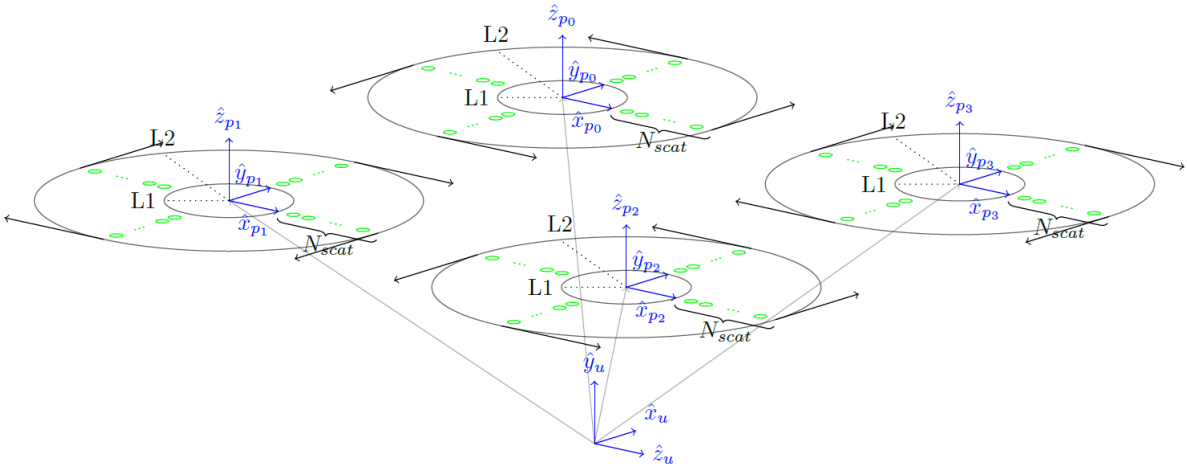

Figure 3.10: Complex drone model. The blue vectors represent the basis vector for both the core of the drone (u) and each of the four propellers (p_i). The green ellipses show each of the point-scatterers included in the experiment. There are N_{scat} scatterers for each blade on each propeller. Note that the spin direction of the 0th and 2nd propellers is counter-clockwise while the spin direction of the 1st and 3rd propellers is clockwise; a typical configuration for drones. The blade lengths are the same for each propeller with a value of $L2 - L1$.

Parameter label	Description	Value
f_c	Carrier frequency	20 GHz
R	Range between the transmitter and target	100 m
v	Target velocity	0 m/s
BW	Signal bandwidth	5 MHz
t_s	Simulation time	1 ms
P_{tx}	Transmit Power	10 W
G_{tx}	Transmitter system gain	15 dB
G_{rx}	Receiver system gain	15 dB
N_f	Receiver system noise figure	6 dB
$L1$	Length from the center of the propeller to the start of the blade	1 m
$L2$	Length of the propeller blade $+L1$	2 m
RPM	Rotations per minute for each propeller	20 k rot/min
N_{prop}	Number of propellers	4
RCS	RCS area for each point scatterer along the blades	$\frac{0.05}{N_{scat}}$ m^2

Table 3.1: Experimental verification parameters for Section 3.3.3.

This experiment works by simulating the scenario using MATLAB's Phased Array toolbox. The package allows for simulating the entire system from transmitter, to enabling the multiple reflections from the complex drone model, to the receiver. With the system initialized, the Continuous Wave (CW) signal is generated in a discrete manner for each sample point for the duration of the simulation. To significantly reduce computation required to simulate this environment, narrowband sampling of 5 MHz is used for a 20 GHz carrier wave with the intention of demodulating the signal before sampling at the receiver.

The software works by iteratively changing the positions and velocities of the targets and sending a portion of the signal through the entire channel to get the portion of the received signal delivered by the transmitted signal. Each scattering center is considered a separate target in this simulation so it is necessary to define both the position and velocity for each of the $N_{prop} \cdot N_{blades} \cdot N_{scat}$ point-scatterers. The Rx signal components are then aggregated together coherently to form the final Rx signal.

The theoretical Rx signal ψ_{dc} is then calculated by mapping the experiment parameters to the parameter set $P_{dc}(t)$ as in equation (3.96). The theoretical computation is then performed using equation (3.93).

Both the experimental and theoretical Rx signals are then demodulated to a baseband signal by multiplying them by $e^{-j2\pi f_c t}$. An FFT is then taken for both signals are their spectrums can be compared.

In Figures 3.11 through 3.14, the normalized magnitudes of the experimental received signal and theoretical received signal Discrete-Time Fourier Transforms (DFTs) are plotted. It appears as though the theoretical signal does not map to the experimental signal precisely, though it does form a nice envelope in a more simplified shape compared to the experimental Rx signal which appears to just be a noisy signal with a higher amplitude in the micro-Doppler band for the carrier. The effective bandwidths of each signal are almost identical. It is also shown that because of the micro-Doppler effects introduced by the spinning of the propellers mounted on the drone, the transmitted signal is distorted both positively and negatively in the frequency domain around the carrier frequency by an amount that terminates near the maximum possible micro-Doppler shift. The theoretical bandwidth for a simple sinusoidal signal is infinitesimal as in a delta pulse, however here it can be seen that the bandwidth is over 1 MHz. This is a big difference when compared to the transmitted signal, whose frequency domain representation is also plotted in all graphs.

There does not seem to be a better option for how many scattering centers to use along the blades. All signals seems to distort the carrier wave similarly within the bandwidth predicted by the theoretical model presented in this thesis.

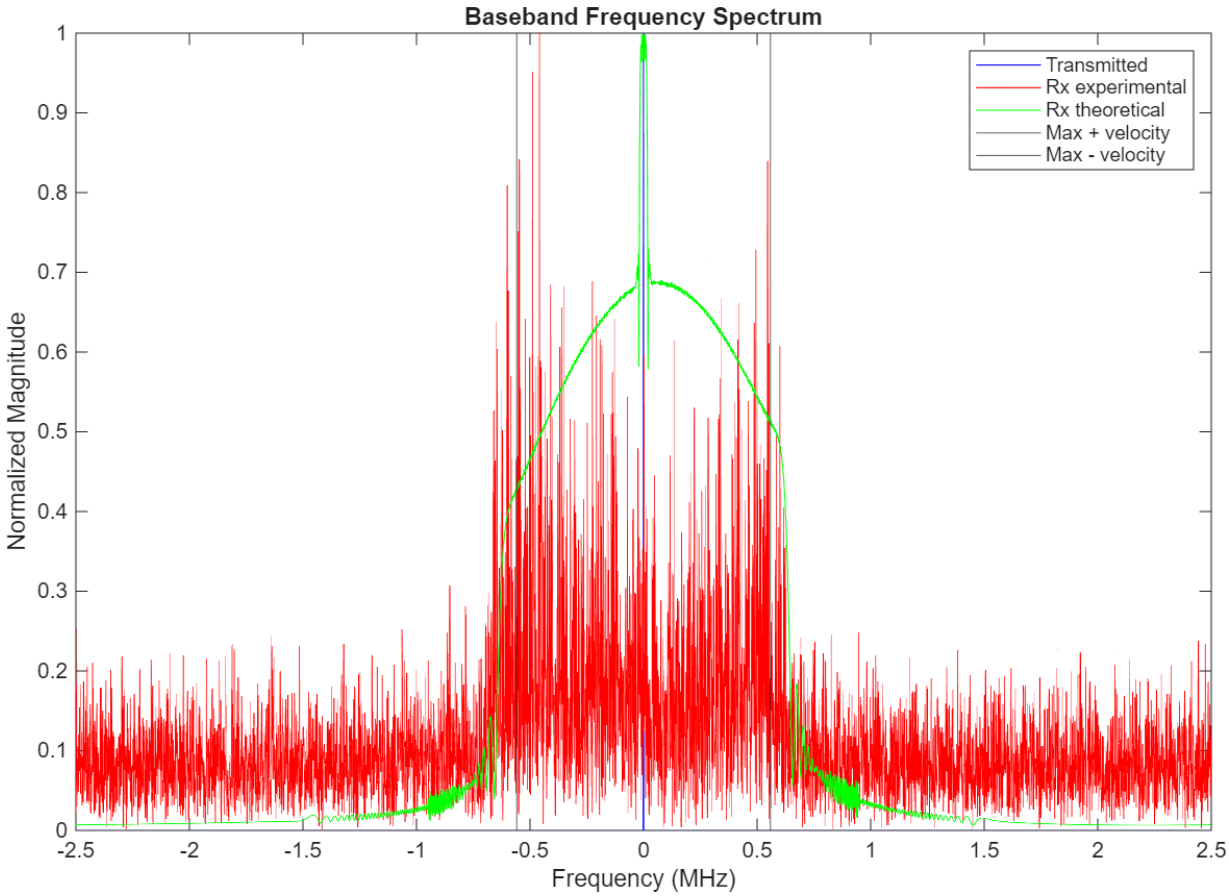

Figure 3.11: Simulation spectrum results with $N_{blades} = 2$ and $N_{scat} = 1$.

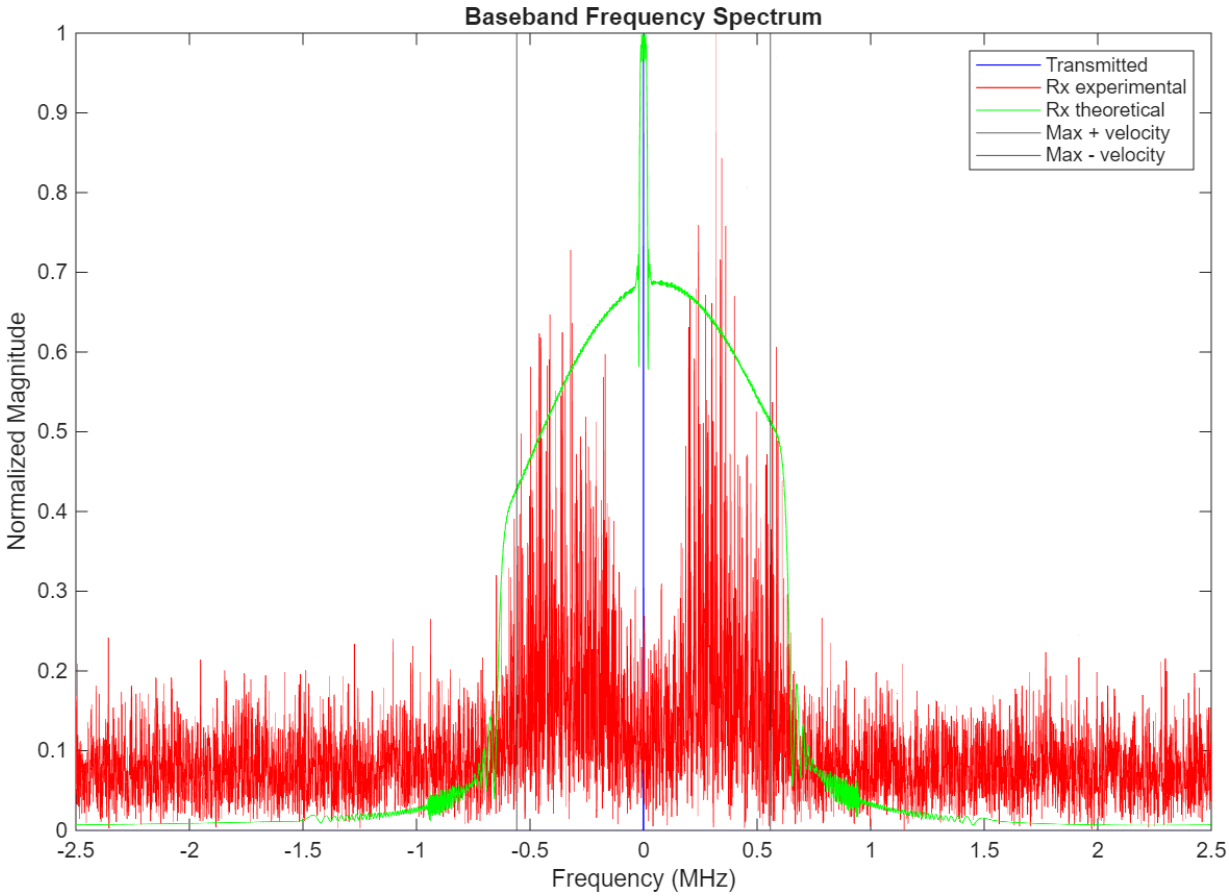

Figure 3.12: Simulation spectrum results with $N_{blades} = 2$ and $N_{scat} = 50$.

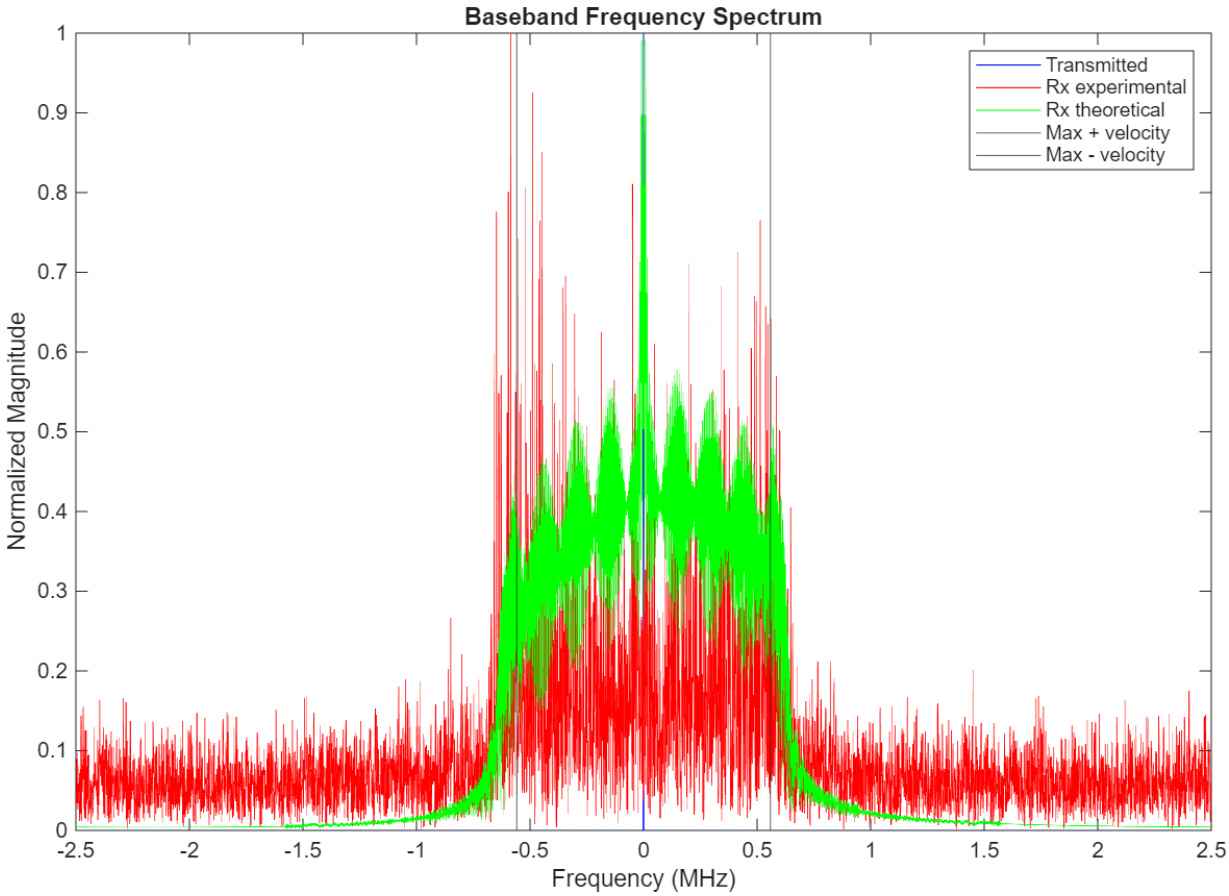

Figure 3.13: Simulation spectrum results with $N_{blades} = 4$ and $N_{scat} = 1$.

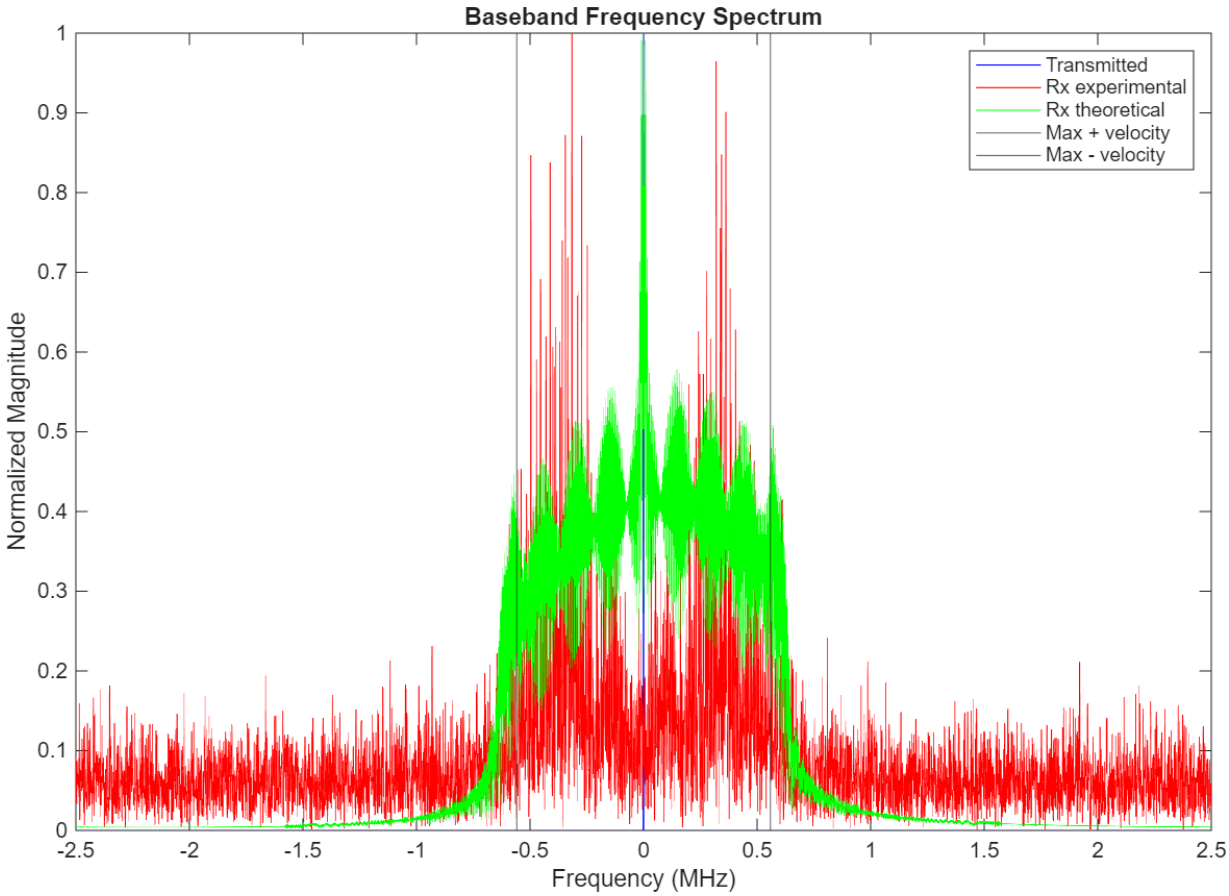

Figure 3.14: Simulation spectrum results with $N_{blades} = 4$ and $N_{scat} = 50$.

There does not seem to be a major difference in the shape of the experimental signals by changing the number of blades for each propeller: N_{blades}. Examining the experimental results in Figures 3.11 and 3.14, it appears as though increasing the number of blades has no significant effect. There is a major effect, however. It is that increasing the number of blades increases the amount of power which is in the micro-Doppler band relative to the amount of power scattered by the static portion of the drone. This effect is not seen in these images because the magnitudes are normalized and the backscatter from the static portion of the drone is not taken into consideration. This is further examined in Section 3.4.

All graphs also show a vertical line for $\pm 2f_c||\vec{v}||/c$ as in equation (3.110). Note that in all eight simulations, both theoretical and simulation results show that the bandwidth actually extends past the frequency distortion due to the maximum speed of the propellers. Therefore, the propellers are interacting cooperatively to further skew the signal beyond this expected maximum or there is some spectral leakage occurring.

This experiment shows that there is merit to using this theoretical model for modeling electromagnetic reflections from complex drone-like objects.

3.4 Combination of static and dynamic reflections

Equation (3.93) describes the echo signal for the total reflected signal received by the transceiver for I propellers on a drone. It does not consider the portion of the reflected signal which is due strictly to the static (non-rotating) portion of the drone. The static portion of the reflection can be approximately computed in the following manner, making use of the Radar Cross Section (RCS) σ [37] for the UAV whose positional norm is $||\vec{x}_u^o||$. Letting $C = ||\vec{x}_u^o - \vec{x}_t^o||$,

$$\psi_s = \iint_\sigma \frac{\psi_0}{L^2(C)} e^{j2\pi f_c(1+2v_r c^{-1})(t-2Cc^{-1})} da \tag{3.111}$$

where da is the infinitesimal surface area for the RCS. Applying the far-field approximation, all the components of the integrand can be reasonably made independent of which part of

the surface area it is being evaluated at. Therefore,

$$\psi_s \approx \frac{\psi_0}{L^2(C)} e^{j2\pi f_c(1+2v_r c^{-1})(t-2Cc^{-1})} \iint_\sigma da \tag{3.112}$$

$$\approx \sigma(t) \frac{\psi_0}{L^2(C)} e^{j2\pi f_c(1+2v_r c^{-1})(t-2Cc^{-1})} \tag{3.113}$$

$$\approx \sigma(t) \frac{\psi_0}{L^2(C)} e^{j2\pi f_c(1+2(||\vec{v}_u^{\,o}-\vec{v}_t^{\,o}||\cdot\frac{\vec{C}}{C})c^{-1})(t-2Cc^{-1})}. \tag{3.114}$$

Hence the total reflected signal is the combination of both of these, $\psi_{MM}(P_{MM}(t)) = \psi_s + \psi_{dc}$, and is given by

$$\begin{aligned}\psi_{MM}(P_{MM}(t)) \approx \sigma(t) \frac{\psi_0}{L^2(C)} & e^{j2\pi f_c(1+2(||\vec{v}_u^{\,o}-\vec{v}_t^{\,o}||\cdot\frac{\vec{C}}{C})c^{-1})(t-2Cc^{-1})} \\ & + \psi_0 e^{j2\pi f_c t} \sum_{i=0}^{I-1} \frac{(L_2(i)-L_1(i))e^{-j4\pi f_c R_i c^{-1}}}{L^2(R_i)} e^{j4\pi f_c c^{-1}(\vec{h}\cdot\frac{\vec{R}_i}{R_i})(t-\frac{2R_i}{c})} \\ & \cdot \sum_{n=0}^{N_i-1} e^{j(L_1(i)+L_2(i))l/2} \mathrm{sinc}\left(\frac{L_2(i)-L_1(i)}{2} l\right).\end{aligned} \tag{3.115}$$

The set of parameters $P_{MM}(t)$ required to use this theoretical model is thus modified to include the UAV's RCS:

$$P_{1,MM}(t) = \{\vec{x}_u^{\,o}, \vec{x}_t^{\,o}, \boldsymbol{R}_u^o, f_\varepsilon, \vec{v}_u^{\,o}, \vec{v}_t^{\,o}, \sigma\} \cup \{\{\Omega_{n,i}\}_{n=0}^{N_i-1}, \vec{x}_{p_i}^{\,u}, \boldsymbol{R}_{p_i}^u, f_{rot,i}\}_{i=0}^{I-1} \tag{3.116}$$

$$P_{2,MM} = \{\psi_0, f_c\} \cup \{L_1(i), L_2(i), N_i\}_{i=0}^{I-1} \tag{3.117}$$

$$P_{MM}(t) = P_{1,MM}(t) \cup P_{2,MM} \tag{3.118}$$

3.4.1 Experimentation with Simulation

To validate this idea of having a static RCS for modelling the drone as in equation (3.115), another experiment is assembled similar to the experiment shown in Section 3.3.3. The difference between that experiment and this one is the inclusion of a large RCS which does not move relative to the center-of-mass of the drone centered on the u reference frame. This is shown in Figure 3.15. The parameters for this experiment are shown in Table 3.2. The scattering centers are again all modelled with Swerling 2 probabilistic models.

The results for this experiment are shown in Figures 3.16 and 3.17. Note that the magnitude of the spectrum in the micro-Doppler band (which excludes the center frequency) is

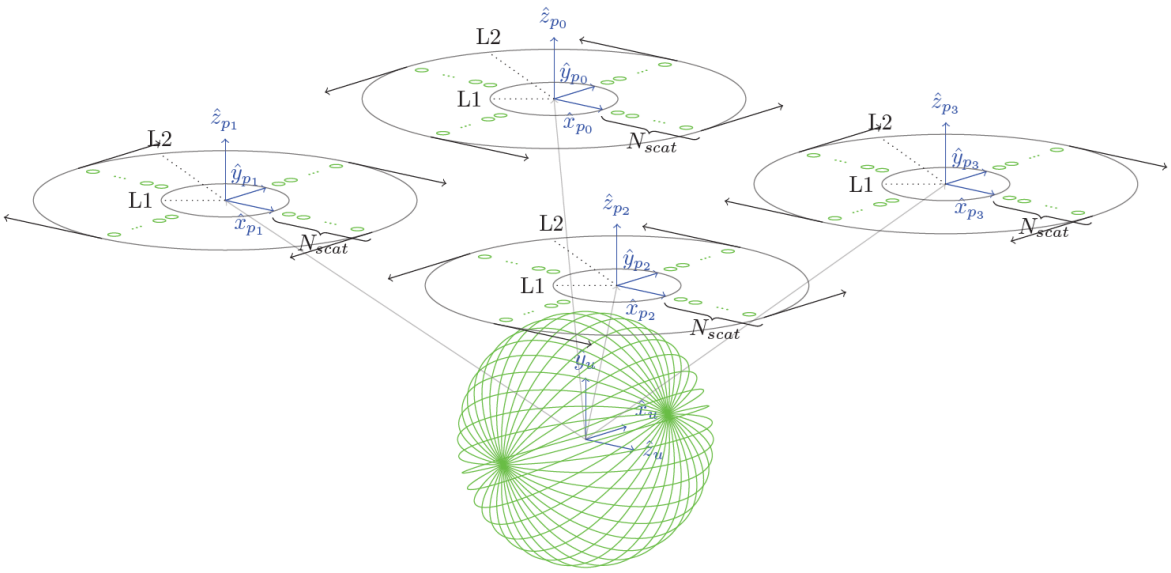

Figure 3.15: Complex drone model for static and dynamic scattering centers. The difference between this scenario and the previous, as in Figure 3.10, is the inclusion of this large RCS modelled as a sphere.

Parameter label	Description	Value
f_c	Carrier frequency	20 GHz
R	Range between the transmitter and target	100 m
v	Target velocity	0 m/s
BW	Signal bandwidth	5 MHz
t_s	Simulation time	1 ms
P_{tx}	Transmit Power	10 W
G_{tx}	Transmitter system gain	40 dB
G_{rx}	Receiver system gain	40 dB
N_f	Receiver system noise figure	20 dB
$L1$	Length from the center of the propeller to the start of the blade	1 m
$L2$	Length of the propeller blade $+L1$	2 m
RPM	Rotations per minute for each propeller	20 k rot/min
N_{prop}	Number of propellers	4
N_{blades}	Number of blade for each propeller	4
N_{scat}	Number of scatterers on each blade	10
$RCS_{dynamic}$	RCS area for each point scatterer along the blades	0.01 m^2
RCS_{static}	RCS area for the static scattering center	0.5 m^2

Table 3.2: Experimental verification parameters for Section 3.4.1.

much lower relative to the results from the previous experiments in Figures 3.11 and 3.14. This is because the large scatterer at the center of the drone is the most significant scatterer in the experiment and skews the magnitude normalization. Going from $N_{blades} = 2$ to $N_{blades} = 4$ shows that increasing the number of moving scatterers increases the amount of signal power within the micro-Doppler band.

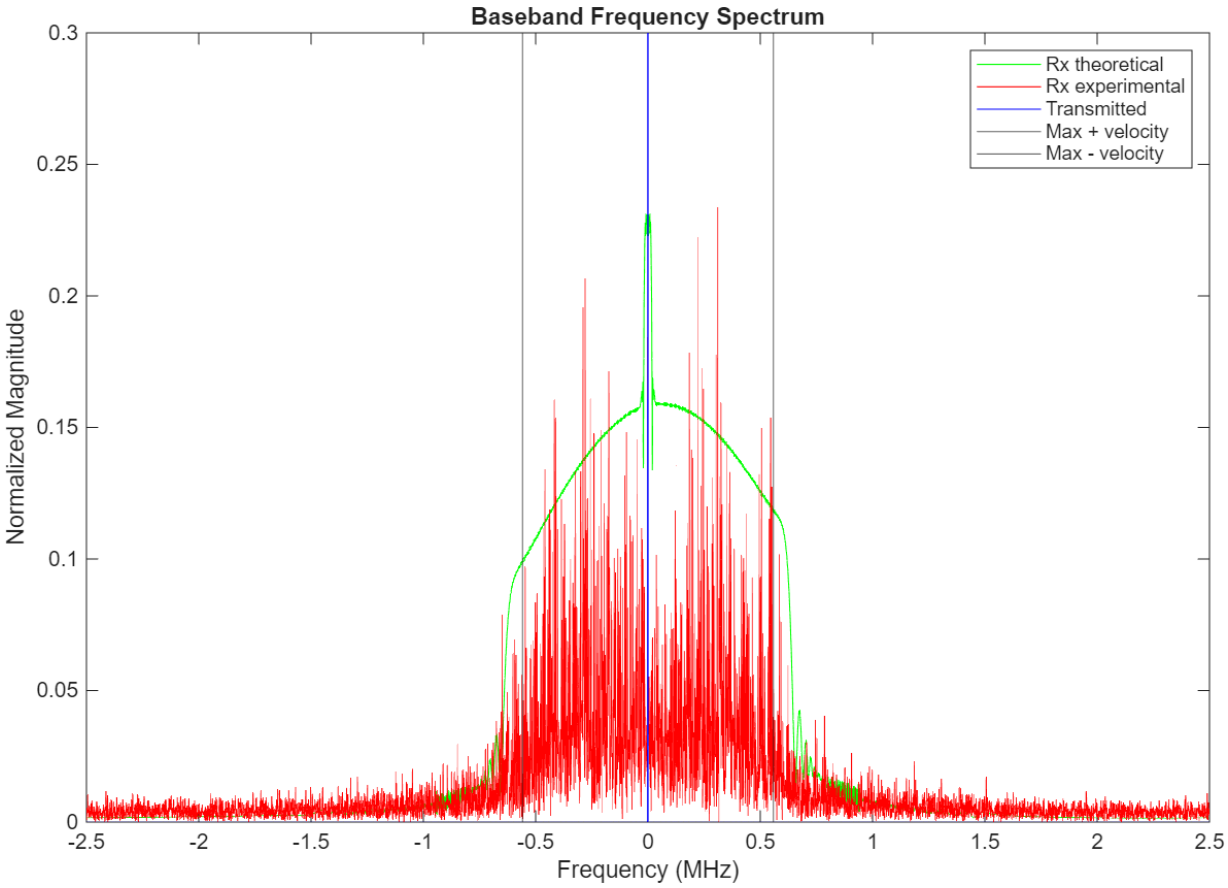

Figure 3.16: Simulation spectrum results with $N_{blades} = 2$. Note that the normalized magnitude on the y axis goes from 0 to 0.3. The remaining 0.3 to 1.0 on the y-axis that is hidden has a vertical line for which the blue, green and red signals all climb to 1.0.

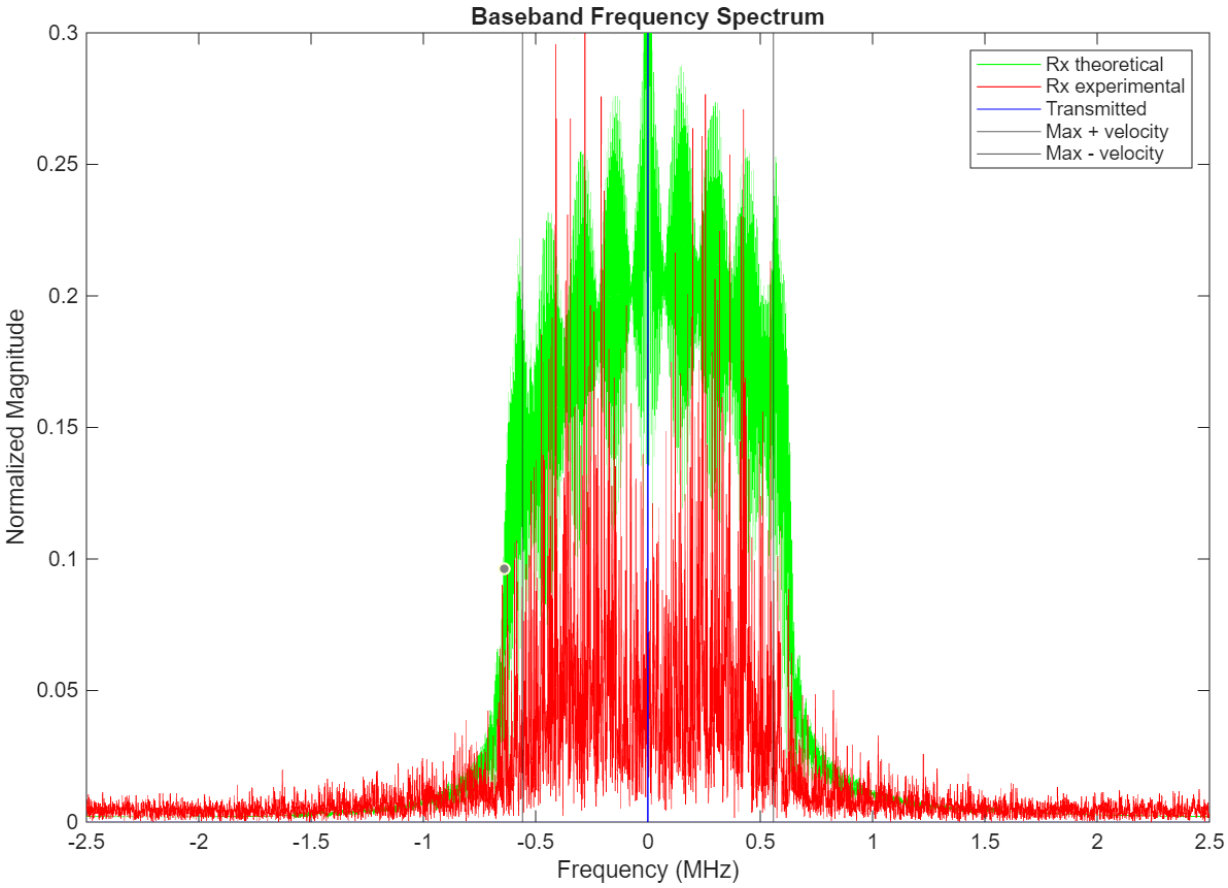

Figure 3.17: Simulation spectrum results with $N_{blades} = 4$. Note that the normalized magnitude on the y axis goes from 0 to 0.3. The remaining 0.3 to 1.0 on the y-axis that is hidden has a vertical line for which the blue, green and red signals all climb to 1.0.

Chapter 4

Theoretical Models for 5G OFDM Transmit Signals

In this Chapter, the modelling work that has been done for simple complex exponential sinusoidal backscatter is combined to form an aggregate backscatter signal for the more realistic Orthogonal Frequency Division Multiplexing (OFDM) transmit signal, which is to be used as the radar pulse.

The core of OFDM is the simultaneous transmission of frequency-adjacent subcarriers whose amplitudes vary depending on what information is being communicated at a particular symbol time [29]. The set of OFDM data symbols $x(k,p)$ is therefore a matrix whose arguments are the indices of both frequency (subcarrier index k) and time (OFDM symbol index p). For N_s subcarriers in a OFDM signal with N_t time-intervals whose duration is T, there are N_sN_t *resource elements* available for communicating information.

Specifically, the baseband signal for one OFDM time interval at index p can be expressed by [44]

$$s_{tx}(t) = \begin{cases} \sum_{k=0}^{N_s-1} x(k,p)e^{j2\pi t\frac{k}{T}} & t_p \leq t < t_{p+1} \\ 0 & t < t_p \vee t_{p+1} \leq t \end{cases} \tag{4.1}$$

where t_p and t_{p+1} are the time thresholds for the pth time-interval. For example, an OFDM signal composed of 6 orthogonal subcarriers is plotted in Figure 4.1 for one time-interval and $x(k,p) = 1, \forall k$. The SubCarrier Spacing (SCS) in the frequency domain between the subsequent subcarriers is then just $1/T$ where T is the symbol duration. In the 3GPP 5G NR standards, the SCS must be preset to one of seven possible values as in [1].

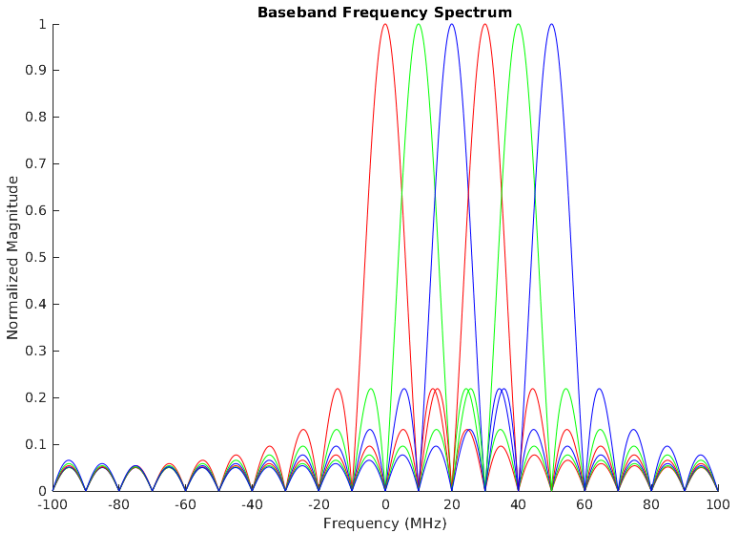

Figure 4.1: OFDM carriers plotted side-by-side in the frequency domain.

If this type of signal is to be used as the transmit signal to listen for backscatter reflections, then it should be expected that the received signal would be a coherent combination of the return signals from multiple simple sinusoidal waves as both the transmit and received signals can be decomposed into a linear combination of simpler signals. With the transmit signal having the form of equation (4.1), the received signal should take the following form before windowing:

$$\psi_{dark}(P(t),p) := \sum_{k=-\left\lfloor \frac{N_s}{2} \right\rfloor}^{\left\lceil \frac{N_s}{2} \right\rceil - 1} x(k,p)\psi(P(t, f_c + \frac{k}{T})) \tag{4.2}$$

with $P(t)$ taking the value of either $P_{MM}(t)$ as in equation (3.118) or $P_{PS}(t)$ as in equation (2.38) and $\psi(P(t))$ being defined in either equation (3.115) as ψ_{MM} for the MM model or equation (2.35) as ψ_{PS} for the point-scatterer model. The intention with the notation $\psi(P(t, f_c + \frac{k}{T})$ for the arguments of ψ is to convey that the backscatter function is no longer a function of the carrier frequency but of the subcarrier frequencies instead. The summation indices are also adjusted from equation (4.1) to better center the baseband frequencies around 0 Hz.

After windowing the backscatter function, the resulting signal takes the form of

$$\psi_o(P(t),p) = \ldots$$
$$\begin{cases} \psi_{dark}(P(t),p) & 2R_{min}c^{-1} \leq t \leq 2R_{max}c^{-1} + T \\ 0 & \text{otherwise} \end{cases} \tag{4.3}$$

where R_{min} is defined as $\min(\{||\vec{x}_{p_i}^{\,o} - \vec{x}_t^{\,o}||\}_{i=0}^{I-1})$ for the MM model and $\min(\{||\vec{x}_p^{\,o} - \vec{x}_t^{\,o}||\}_{p=0}^{P-1})$ for the point-scatterer model and R_{max} being similarly defined.

In the 3GPP 5G NR standard, there exists different *numerology* $\mu \in \mathbb{Z}, 0 \leq \mu \leq 6$, to specify communication parameters. Specifically, one 5G frame is composed of 10 subframes. The subframes are composed of 2^μ slots and one slot is composed of 14 data symbols. After every slot, a cyclic prefix is transmitted to increase the orthogonality of the different carriers during transmission to increase the signal reliability. The cyclic prefix increases in size as the SCS increases [1, 40, 50]. For the purposes of this research, the transmission of the cyclic prefix is not considered as it is more of a physical layer enhancement and does not contribute non-redundant information. This does form a difference between a standard 5G transmission signal and a purely OFDM transmission, however.

The largest SCS of 960 kHz when $\mu = 6$ provides the smallest symbol duration of roughly 1.118 μs [1] which includes the cyclic prefix. Without cyclic prefix, the duration would be $1/960k \approx 1.042$ μs. This is the SCS that provides the most precision and is only available in the FR2 band of 5G NR which is from 24.25 to 71 GHz [1] from release 17 of the communication standard. Hence the radar waveform will be targeting lower range, due to the propagation loss being proportional to the carrier frequency, and higher resolution since the smaller wavelength signal is able to discern smaller reflection features on complex radar targets.

With this signal model, the time-domain of the received signal can be analyzed and cross-referenced with a Finite Impulse Response (FIR) filter that is a time-reversed and complex conjugated version of the transmit signal for matched-filtering:

$$h[n] = s_{tx}^*[-n] \tag{4.4}$$
$$y[n] = \psi_o(P[n],p) * h[n]. \tag{4.5}$$

where the '$*$' superscript indicates the complex conjugate, the '$*$' operator describes the convolution operation and the signals have been discretized with some sampling frequency f_s. The peak of $y[n]$ indicates where the signal ψ_o most closely resembles the transmit radar signal for each pulse.

To perform frequency-domain analysis on the signal from a single pulse, the received signal is first demodulated by performing the following operation:

$$\psi_b[n] = e^{-j2\pi f_c n}\psi_o(P[n], p) \tag{4.6}$$

where the b subscript in ψ_b indicates that the signal is in baseband. A Fast Fourier Transform (FFT) can then be taken of the received signal between the index where $y[n]$ is maximized and the same index plus the symbol duration. This can be compared to the simulated signal's Discrete Fourier Transform (DFT) as in Section 3.3.3.

4.1 Constructing a Traditional Pulsed Radar Framework Using OFDM

Traditional pulse radars work on the basis of having the same pulse be transmitted, reflected and received multiple times with a certain Pulse Repetition Frequency (PRF) [37]. The transmission signal in this case is $s_{tx}(t)$ as in equation (4.1). The signal is transmitted at the start of the pulse interval (i.e. $0 \leq t < T$) and some time is allocated for receiving radar return signals for each pulse. This model can be recreated in the OFDM framework by letting resource elements in subsequent time-intervals be equal to zero through changing the data symbols $x(k, p)$. For example, for a pulse interval of $M \in \mathbb{N}$, which is the number of OFDM symbols in one radar pulse, $\forall$ subcarrier index k and pulse number $a \in \mathbb{Z}, a \geq 0$,

$$x(k, p) = \begin{cases} 1 & p = aM \\ 0 & p \neq aM. \end{cases} \tag{4.7}$$

For each pulse number, a new received signal can be constructed as in the following matrix:

$$\boldsymbol{r}_x[:, a] = \begin{bmatrix} \psi_o(P[aN_{spp}], a) \\ \psi_o(P[aN_{spp} + 1], a) \\ \vdots \\ \psi_o(P[(a+1)N_{spp} - 1], a) \end{bmatrix} \tag{4.8}$$

where the parameter set $P(t)$ has been discretized to $P[n]$ with some sampling frequency f_s and N_{spp} is the number of samples per pulse. The $\boldsymbol{r}_x$ matrix then has N_{spp} rows and A columns, where A is the number of pulses to be used.

A matched filter can then be used, as described in equations (4.4) and (4.5), to find the peaks of each of the A signals. At the index of maximum correlation n_r, the radar processing signal $z[n]$ can be constructed using all A pulses:

$$y[n] = \sum_{a=0}^{A-1} \psi_o(P[aN_{spp} + n], a) * s_{tx}^*[-n] \tag{4.9}$$

$$n_r = \arg\max_n(y[n]) \tag{4.10}$$

$$z[n] = \boldsymbol{r}_x[n_r, :]. \tag{4.11}$$

From $z[n]$, joint time-frequency domain analysis can be performed, for example using Short-Time Fourier Transforms or Wigner-Ville Distributions [7], to output the micro-Doppler signatures of the target.

4.2 Experimentation through Simulations

This section presents several different simulations intended to numerically assess the viability of micro-Doppler analysis using the augmented MM model. The experiments all compare the results from all three separate methods for generating range-speed response as well as micro-Doppler signatures: augmented MM model, PS model and MATLAB's Phased Array full system simulation (which also uses the PS model).

4.2.1 Optimistic System Simulation

In this experiment, the same scenario is used for the locations and velocities of the scattering centers of the complex drone model as in Figure 3.10. This experiment, however, incorporates two thousand radar pulses in the 5G NR OFDM framework, as described in Section 4.1 with transmit power and Effective Radiated Power (ERP) capped to 35 dBm and 55 dBm respectively in order to meet 5G NR transmission standards.

In this experiment, three separate receive matrices $\boldsymbol{r}_x$ as in equation (4.8) are constructed: one for the experimental result, one for the theoretical result using the MM model and one for the theoretical result using the point-scatterer model. Each of these receive matrices is subject to matched-filtering and peak-finding as in equation (4.10). Each of the three radar signals are then constructed as in equation (4.11). The three radar

Parameter label	Description	Value
f_c	Carrier frequency	50 GHz
R	Range between the transmitter and target	100 m
v	Target velocity	0 m/s
SCS	Subcarrier Spacing	960 kHz
N_s	Number of subcarriers	14
BW	Receive signal bandwidth	14.4 MHz
PRF	Pulse Repetition Frequency	0.5 MHz
N	Number of samples per pulse	29
A	Number of pulses	2k
P_{tx}	Transmit Power	3.16 W
G_{tx}	Transmitter system gain	20 dB
G_{rx}	Receiver system gain	40 dB
N_f	Receiver system noise figure	20 dB
$L1$	Length from the center of the propeller to the start of the blade	20 mm
$L2$	Length of the propeller blade $+L1$	100 mm
RPM	Rotations per minute for each propeller	20 k rot/min
N_{prop}	Number of propellers	4
N_{blades}	Number of blades per propeller	4
RCS_d	RCS area for each point scatterer along the blades	0.05 m^2
RCS_s	Static RCS for the center-of-mass	0.5 m^2

Table 4.1: Experimental verification parameters for Section 4.2.1.

Figure 4.2: Experimental range-speed response for the scenario described in Section 4.2.1.

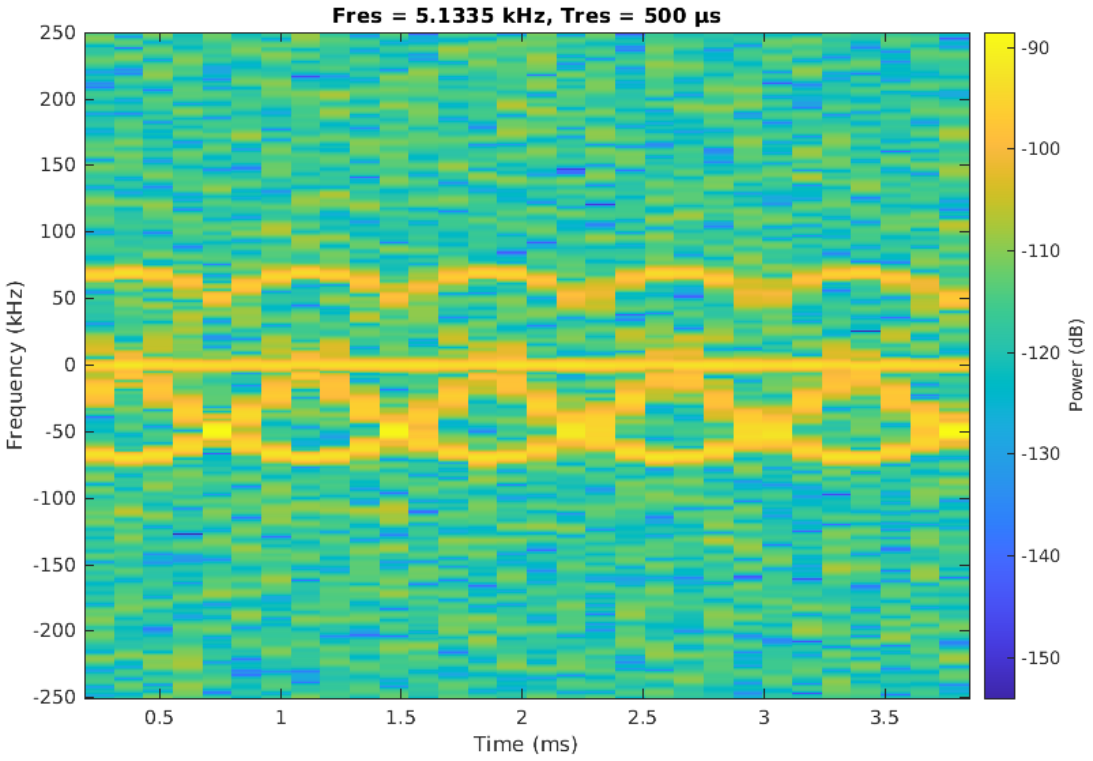

Figure 4.3: Experimental micro-Doppler signature for the scenario described in Section 4.2.1 using Swerling model 3 RCS for all scatterers.

signals are then analyzed in joint time-frequency domain using Short-Time Fourier Transforms (STFT) with a Kaiser window to construct a spectrogram. The parameters for the experiment are as follows in Table 4.1.

The range-speed response Figure 4.2 shows that the entire drone fits into two range bins. The range resolution is given by $c/2BW$ which is roughly 10.4m here so the two range bins which the drone fits into are the bins which are roughly from $(88.54, 98.96]$ and $(98.96, 109.38]$ meters. The experimental received matrix at the index of maximum correlation n_r points to the $(98.96, 109.38]$ range bin and produces the spectrogram shown in Figure 4.3. Three distinct contributors are distinguishable: the static portion of the drone which is a horizontal line at 0 Hz, the negative relative velocity components and the positive relative velocity components which appear sinusoidal. The range-speed response is shown in Figure 4.2. Both Figures show that the drone is clearly detectable at this range with these limitations on output power based on the noise introduced in the MATLAB simulation.

The MM model micro-Doppler signature is shown in Figure 4.4 and that of the point-scatterer model is shown in Figure 4.5. The point-scatterer model accurately resembles the experimentation excluding its amplitude. This is likely due to a difference in RRE between the Phased Array toolbox in MATLAB and what is used to scale the amplitude in this theory. The MM model's micro-Doppler signature seems to not display the signature at all.

To determine why the signature is not being displayed correctly in the MM model, the $\vec{q}$ vector, as defined in equation (3.80) is scaled by a factor of 200 and the simulation is run again. The spectrogram result is shown in Figure 4.6.

The micro-Doppler pattern seems to match the experimental and point-scatterer models, however the bandwidth occupied is wrong and there are distinct peaks for the entire band when positive and negative relative velocities are peaked; i.e. when the sin functions are maximum and minimum. This is due to the effect of the sinc function in the $\boldsymbol{r}_x[n_r, :]$ signal, shown in Figure 4.7. The spectrogram shows drastic peaks at the same moments in time when the relative propeller velocities are maximum and minimum. Clearly, this is a major issue that must be resolved with the augmented MM model.

To attempt to resolve the issue, the theoretical MM model's assumptions are revisited. Taking inspiration from the point-scatterer model, the far-field approximation that the velocities all originate from the center of the propellers as in the original MM model is revised to be at the tip of each of the blades. This modifies the equation for $\psi_{MM}(P_{MM}(t))$

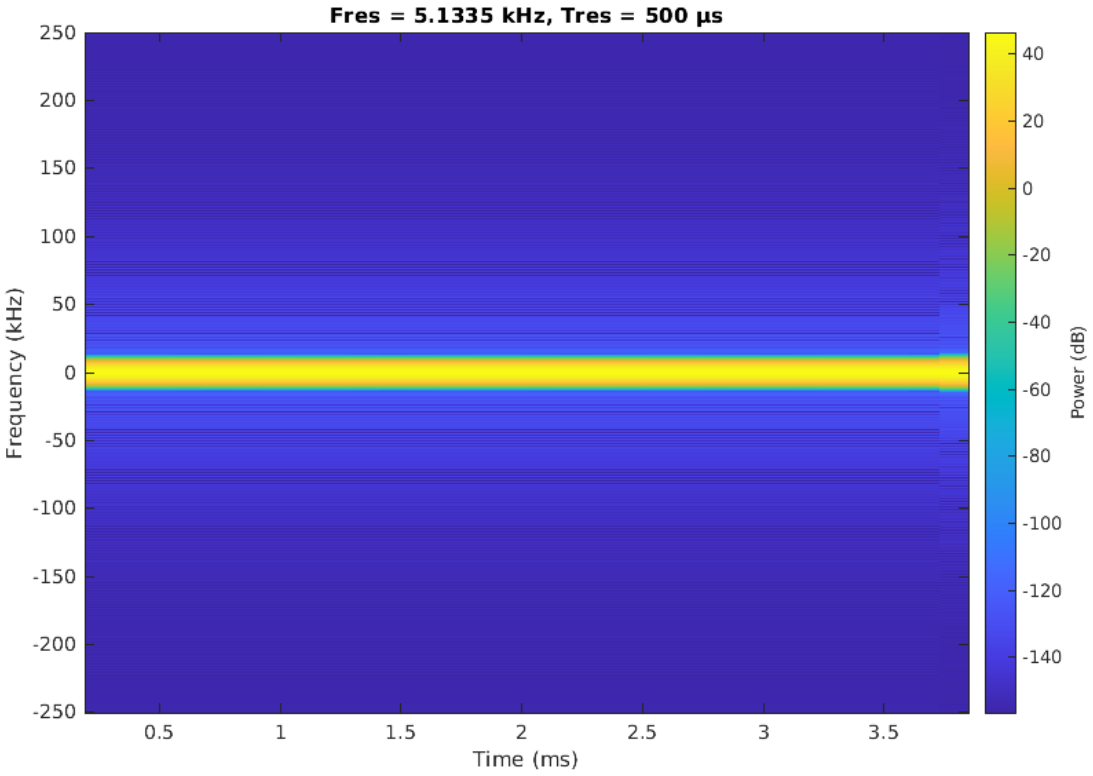

Figure 4.4: Theoretical MM model micro-Doppler signature for the scenario described in Section 4.2.1.

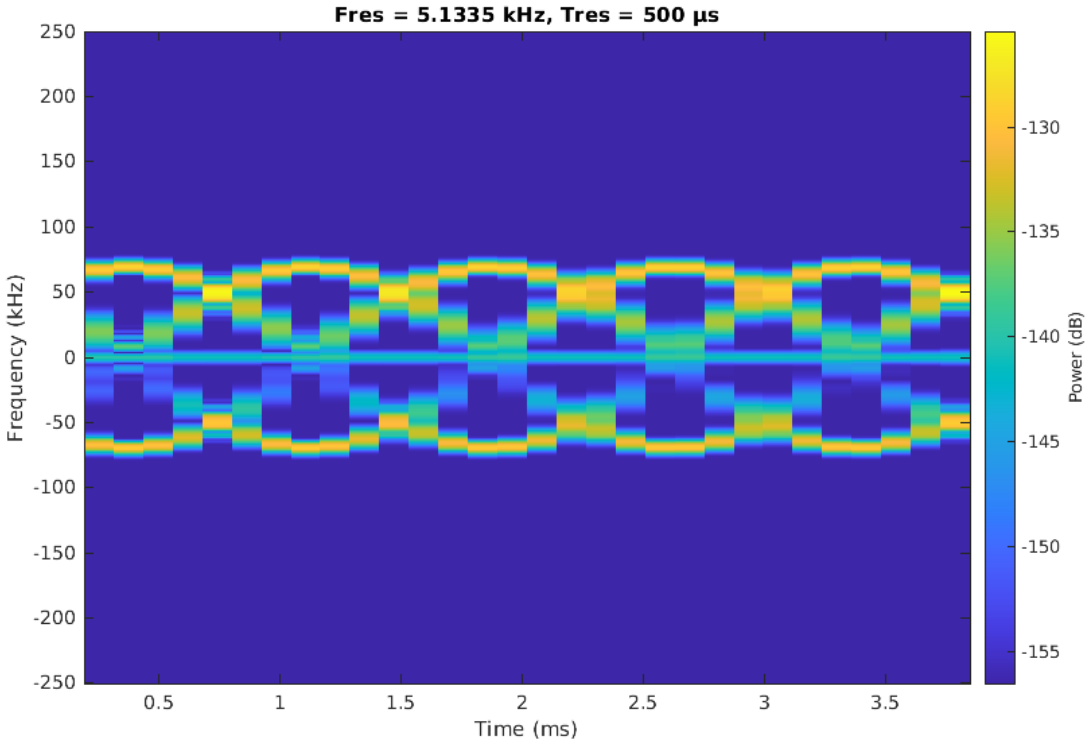

Figure 4.5: Theoretical point-scatterer model with one scatterer at the end of each blade for each propeller.

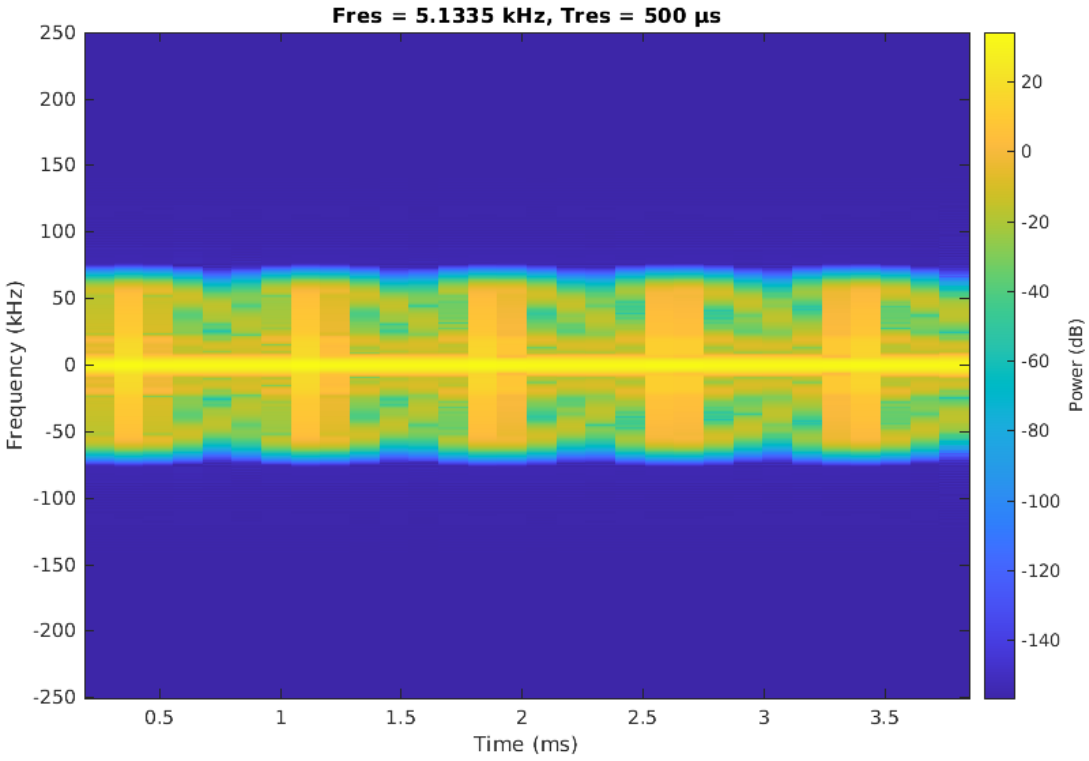

Figure 4.6: Theoretical MM model micro-Doppler signature for the scenario described in Section 4.2.1.

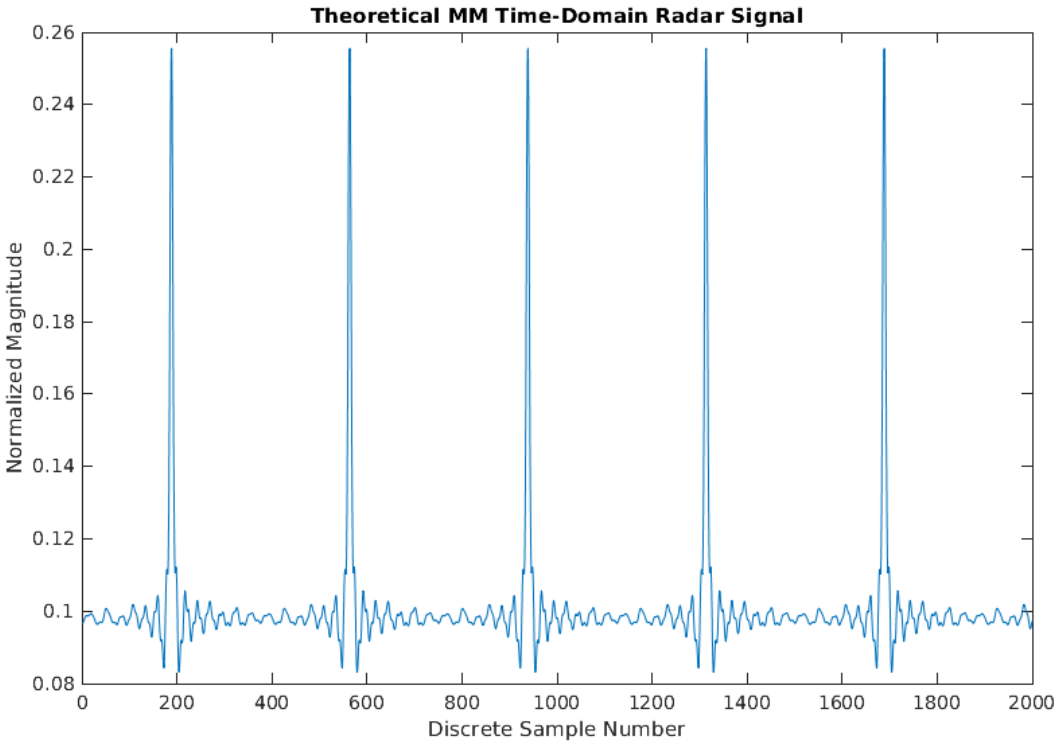

Figure 4.7: Time domain signal for $z[n] = \boldsymbol{r}_x[n_r, :]$ for augmented MM model

from equation (3.115) to

$$\psi_{MM}(P_{MM}(t)) \approx \sigma(t)\frac{\psi_0}{L^2(C)}e^{j2\pi f_c(1+2(||\vec{v}_u^{\,o}-\vec{v}_t^{\,o}||\cdot\frac{\vec{C}}{C})c^{-1})(t-2Cc^{-1})}$$
$$+\psi_0 e^{j2\pi f_c t}\sum_{i=0}^{I-1}\sum_{n=0}^{N_i-1}\frac{(L_2(i)-L_1(i))e^{-j4\pi f_c R_{i,n}c^{-1}}}{L^2(R_{i,n})}e^{j4\pi f_c c^{-1}(\vec{h}\cdot\frac{\vec{R}_{i,n}}{R_{i,n}})(t-\frac{2R_{i,n}}{c})}$$
$$\cdot\, e^{j(L_1(i)+L_2(i))l(i,n)/2}\mathrm{sinc}\left(\frac{L_2(i)-L_1(i)}{2}l(i,n)\right) \tag{4.12}$$

where $R_{i,n} = ||\vec{x}_{i,n}^{\,o} - \vec{x}_t^{\,o}||$ is the distance between the transceiver and the tip of the nth blade on the ith propeller. The expression for l is also modified from $l = 4\pi f_c c^{-1}(\vec{q}\cdot\frac{\vec{R}_i}{R_i})(t-\frac{2R_i}{c})$ to

$$l(i,n) = 4\pi f_c c^{-1}\left(\vec{q}\cdot\frac{\vec{R}_{i,n}}{R_{i,n}}\right)\left(t-\frac{2R_{i,n}}{c}\right). \tag{4.13}$$

This modification to the model is possible because the far-field approximation is being used in the original model to simplify the position of the scatterer from a distance α along the blade to the center of the propeller. Instead of simplifying the distance α to the center of the propeller, it is simplified to the tips of the blades.

With this modification, the simulation is adjusted and the simulation is performed again. The spectrogram for the radar signal generated using the MM model is shown in Figure 4.8.

This time, the micro-Doppler signature perfectly matches the signature from both the experimental model and the point-scatterer model. This concludes that applying the far-field approximation in this way produces much better results than approximating the distance to the center of the propeller. The range-speed response for the modified MM model is shown in Figure 4.9. It correctly predicts the range bins to which the target is located and the speeds at which it is traveling.

In addition, the time-domain signal $\boldsymbol{r}_x[:,\beta]$ for the first three pulses ($\beta = 1,2,3$) are displayed for the experimental, point-scatterer and MM models in Figure 4.10. When compared to the 5G OFDM pulse being used as radar signal, shown in Figure 4.11, the received signals indeed appear to be delayed versions of the transmit signals in that there are two distinct peaks in each signal but also don't immediately show the transmit signal. This is when the combination of pulses comes into play to create radar processing gains to ensure the target is detected. When these signals are aggregated for each pulse and fed through the matched-filter, the correlations are output as in Figure 4.12. The correlation seen in this Figure is proportional to the probability of a target being in each range-bin.

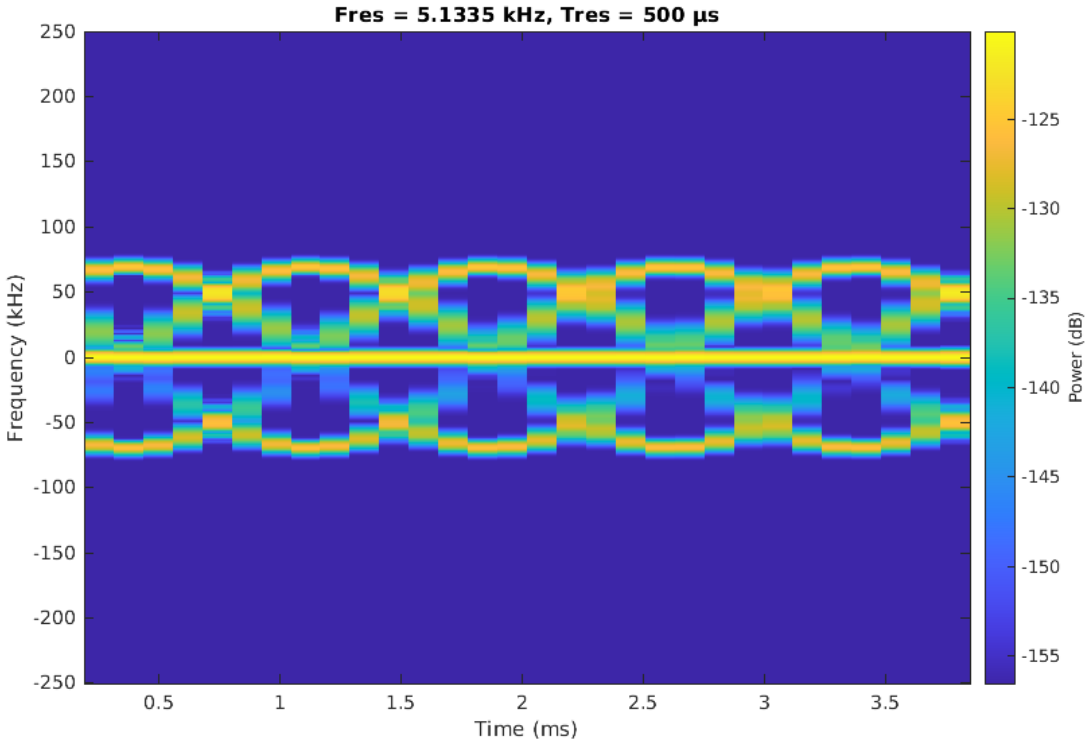

Figure 4.8: Theoretical MM model micro-Doppler signature for the scenario described in Section 4.2.1 with far-field approximation being used at the tip of the blades instead of at the center of the propeller.

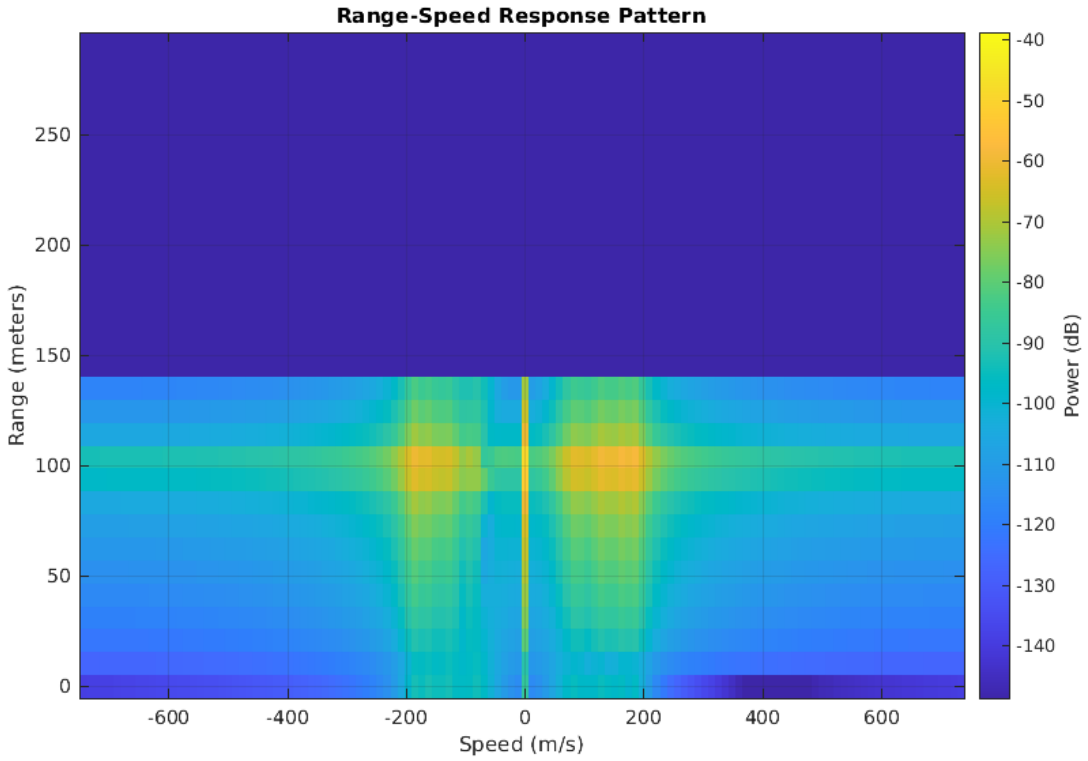

Figure 4.9: Theoretical range-speed response for the scenario described in Section 4.2.1 with modified MM model.

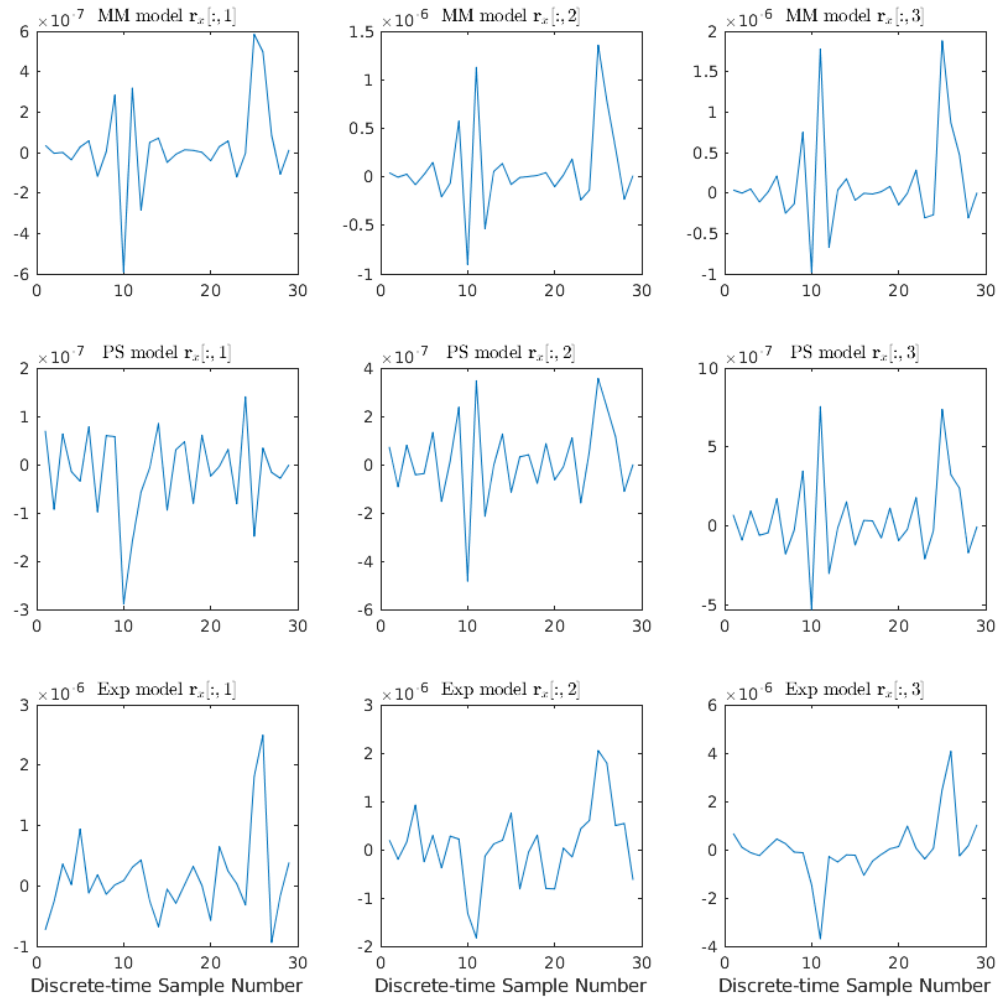

Figure 4.10: Time-domain comparison for ψ_{dark} for the first three pulse responses for the scenario described in Section 4.2.1.

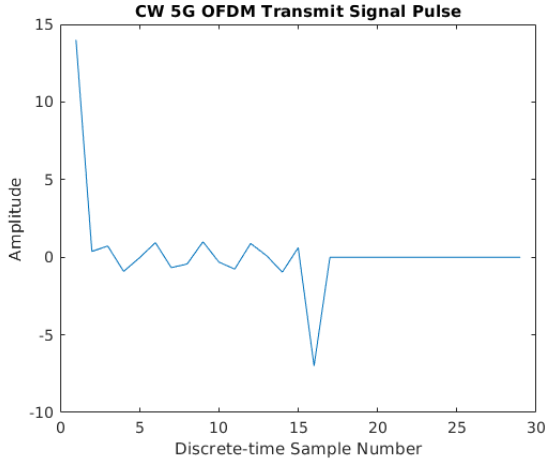

Figure 4.11: Transmit pulse used in experiment described in Section 4.2.1.

The magnitude of the correlation itself is not of major importance when comparing all three models, only that all three of the shape of each of the graphs are very similar, though each of the theoretical models exhibit more range-leakage than that of the experimental model. This is consistent with the range-speed response for the MM model shown in Figure 4.9. The experimental model's correlation function is likely more sharp due to the fact that there is significant noise in the received signal, from both the Swerling models of the scattering centers and the inherit noise to the transceiver system, both of which are not present in the theoretical models (but could easily be included).

Applying windowing to the received signals as in Figure 4.13 reduces the range-leakage. This is displayed in Figure 4.14. Notice that the correlation function tapers much more quickly for the theoretical models than prior to windowing.

Using the range-bin correlation function $y[n]$, one can deduce that the object at roughly 100m away does not reside solely in one range-bin but two. This is consistent with the experiment setup. So theoretically, examining the micro-Doppler signature in the index of maximum correlation n_r displays the micro-Doppler velocities which are occurring only between the range of $[98.96, 109.38]$. One could also perform a similar micro-Doppler investigation within the range of $[88.54, 98.96]$. Doing so produces an almost identical micro-Doppler signature to those displayed for all three models in this experiment. The conclusion can then be made that there is an entity moving in the same manner in both range bins. This is consistent with the experiment setup since two of the four propellers are within the closer range bin and two are in the farther one. This raises the question: if the two front propellers are spinning at a different rate than the back propellers, do the

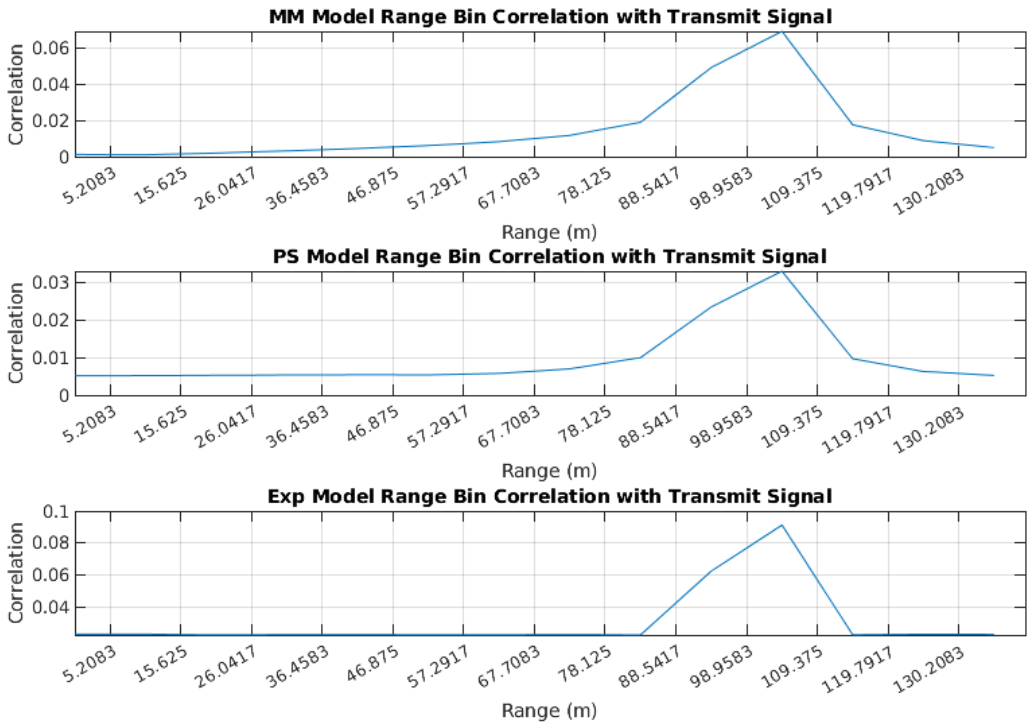

Figure 4.12: Range-bin correlations for each model investigated in Section 4.2.1 for $\boldsymbol{r}_x$ generated using ψ_{dark}.

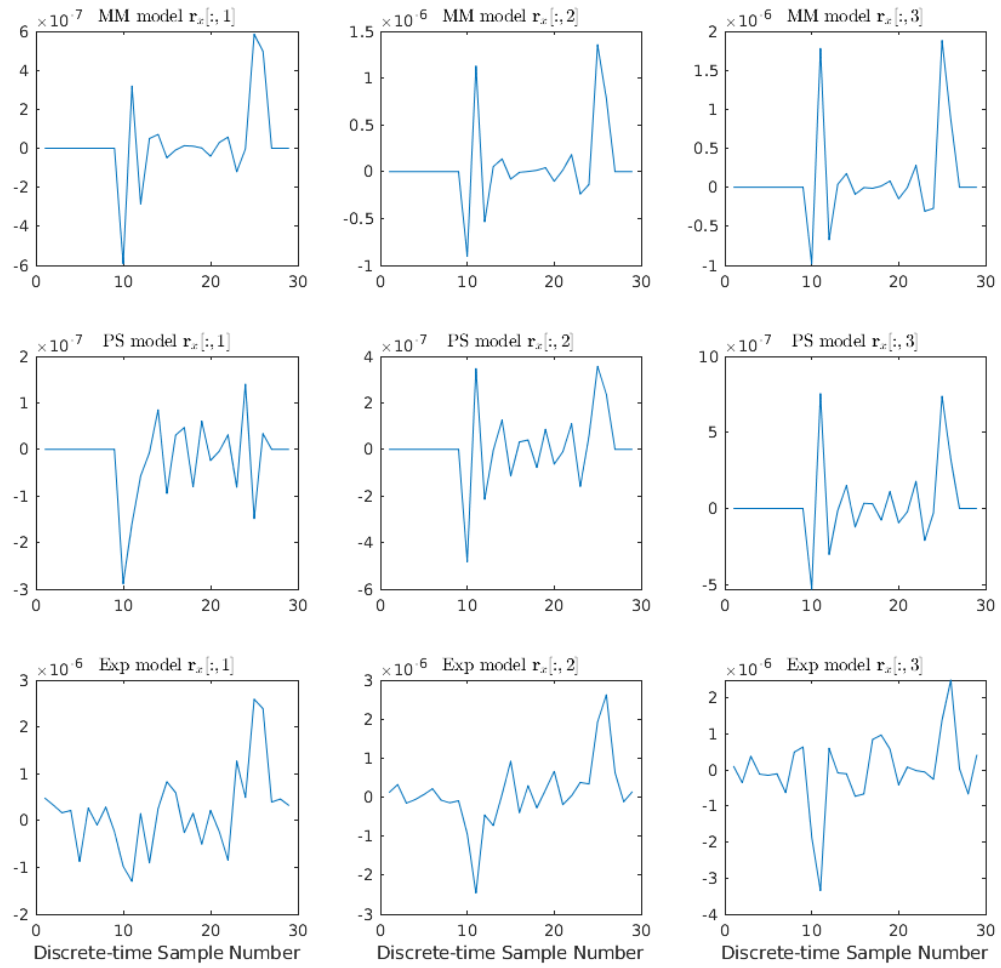

Figure 4.13: Windowed time-domain signals for both theoretical models. The experimental model does windowing automatically.

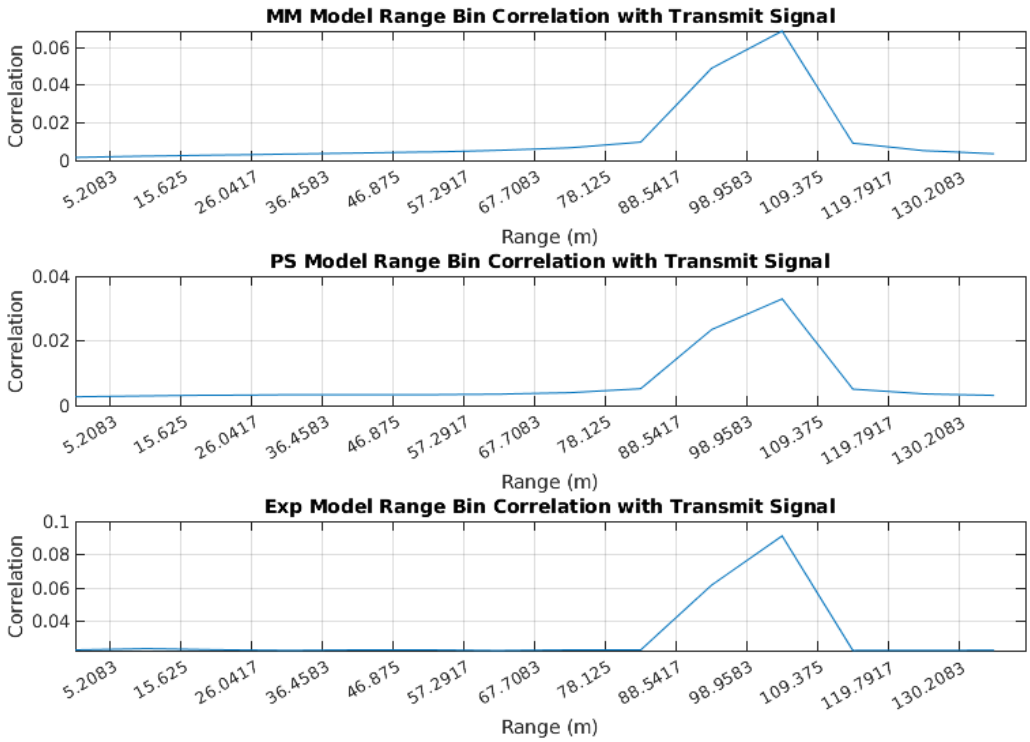

Figure 4.14: Range-bin correlation after windowing the received signal to go from ψ_{dark} to ψ_o as in equation (4.3).

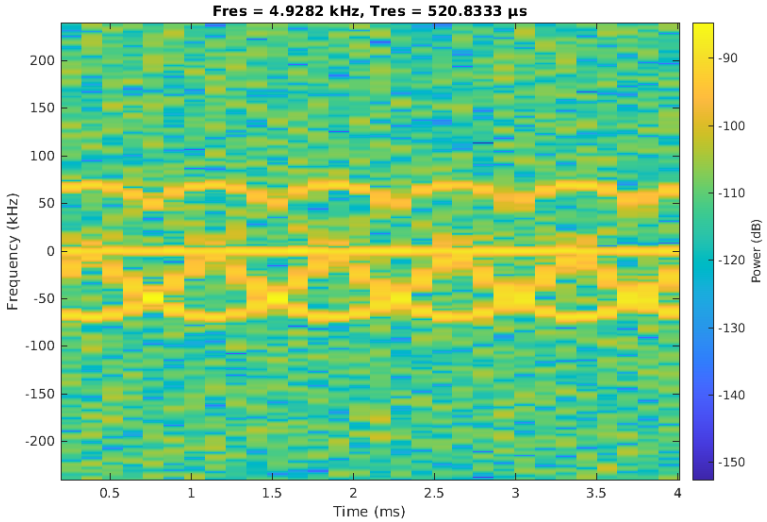

Figure 4.15: Full-system simulation micro-Doppler signature for the scenario described in Section 4.2.2 using Swerling model 2 RCS for all scatterers.

micro-Doppler signatures display a difference in bandwidth? This is further examined in Section 4.2.3.

4.2.2 More Realistic System Numerical Assessment

The full-system simulations in Section 4.2.1 were optimistic by having high gains and low receiver system losses. This simulation is intended to essentially repeat the experiment in Section 4.2.1 but with more realistic system parameters. These more realistic parameters are detailed in the Table 4.2, for example having receive and transmit gains of 10 dBi instead of 20 and 40 dBi respectively. Results are displayed in Figures 4.15 through 4.20.

The three models all show similar results. The magnitudes between the MM model and the full system simulation in both the range-speed response and micro-Doppler signatures are almost identical, indicating that the RRE used in the simulations match, while the magnitude for the PS model is about 20 dB higher than expected. This is an interesting result since the RRE for both PS model and MM model is the same function call in the MATLAB code. This affects the amount of leakage present in the range-speed response in Figure 4.20. Comparing this range-response to the other two, more leakage in both range and Doppler is visible due to the higher magnitude. The range-speed response for the MM

Parameter label	Description	Value
f_c	Carrier frequency	50 GHz
R	Range between the transmitter and target	100 m
v	Target velocity	0 m/s
SCS	Subcarrier Spacing	960 kHz
N_s	Number of subcarriers	14
BW	Receive signal bandwidth	14.4 MHz
PRF	Pulse Repetition Frequency	0.5 MHz
T_{symbol}	Symbol duration	1.04 μs
T_{pulse}	Pulse duration	2.08 μs
N_{spp}	Number of samples per pulse	30
A	Number of pulses	2k
P_{tx}	Transmit Power	3.16 W
G_{tx}	Transmitter system gain	10 dBi
G_{rx}	Receiver system gain	10 dBi
N_f	Receiver system noise figure	6 dB
L	Aggregate system losses	10 dB
$L1$	Length from the center of the propeller to the start of the blade	20 mm
$L2$	Length of the propeller blade $+L1$	100 mm
RPM	Rotations per minute for each propeller	20 k rot/min
N_{prop}	Number of propellers	4
N_{blades}	Number of blades per propeller	4
RCS_d	RCS area for each point scatterer along the blades	0.05 m^2
RCS_s	Static RCS for the center-of-mass	0.5 m^2

Table 4.2: Numerical assessment parameters for Section 4.2.2.

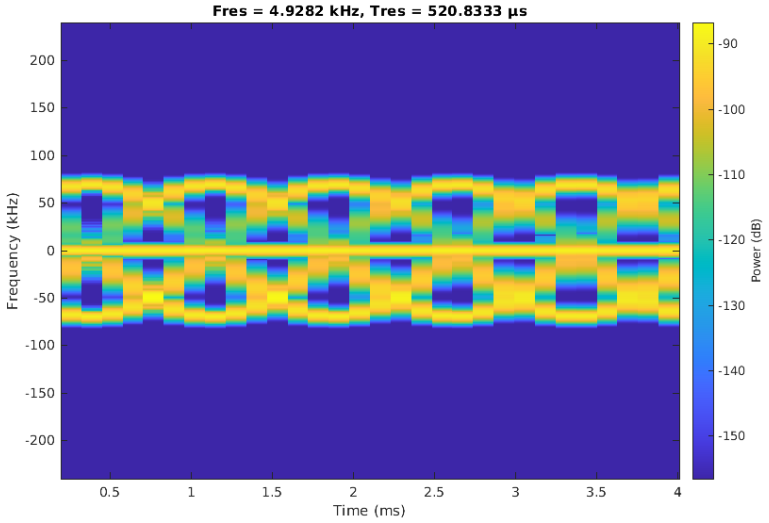

Figure 4.16: Theoretical MM model micro-Doppler signature for the scenario described in Section 4.2.2.

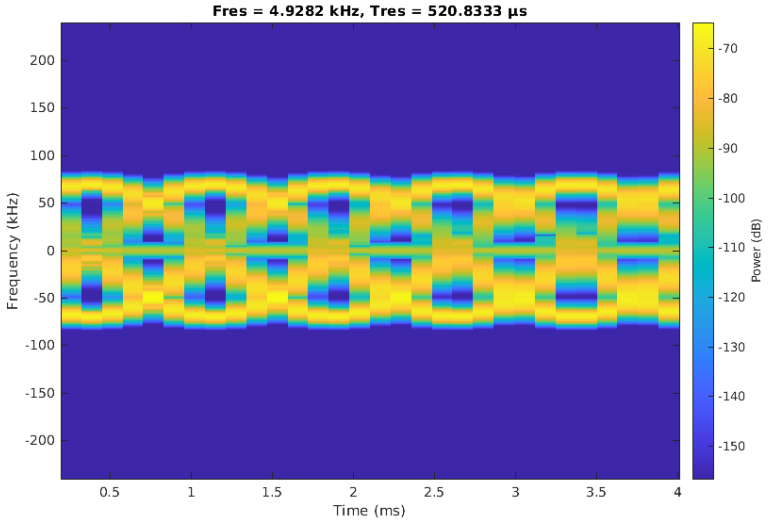

Figure 4.17: Theoretical point-scatterer model with one scatterer at the end of each blade for each propeller.

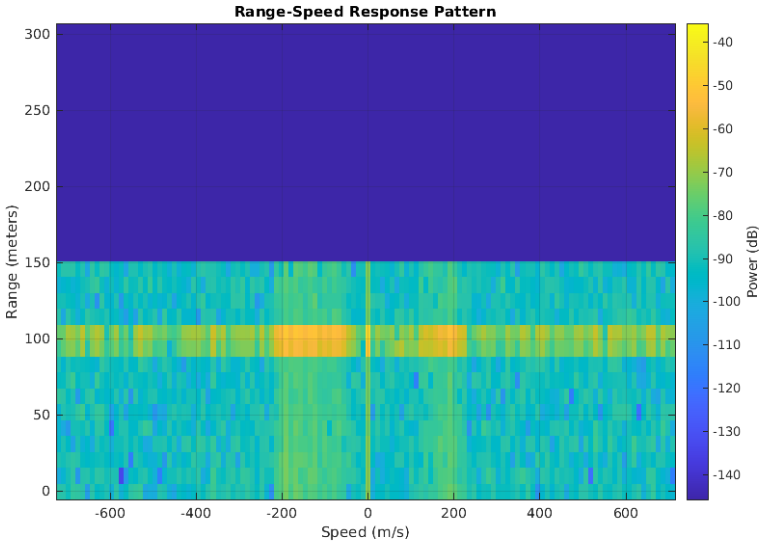

Figure 4.18: Full-system simulation range-speed response for the scenario described in Section 4.2.2.

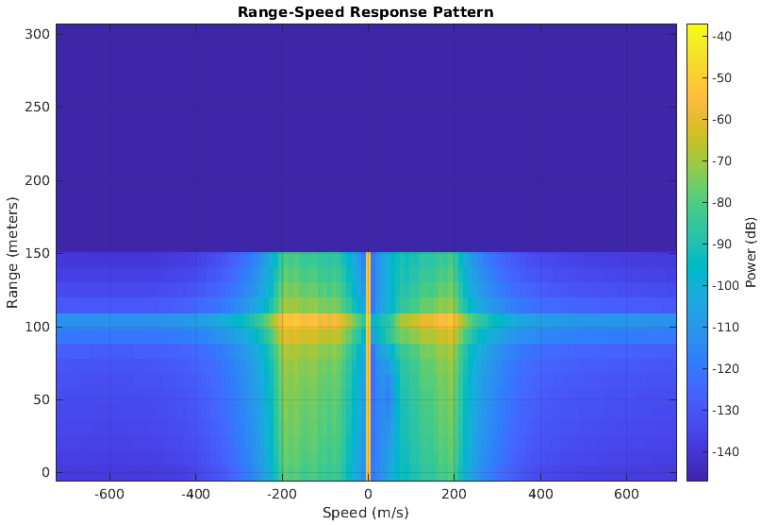

Figure 4.19: MM model range-speed response for simulation in Section 4.2.2.

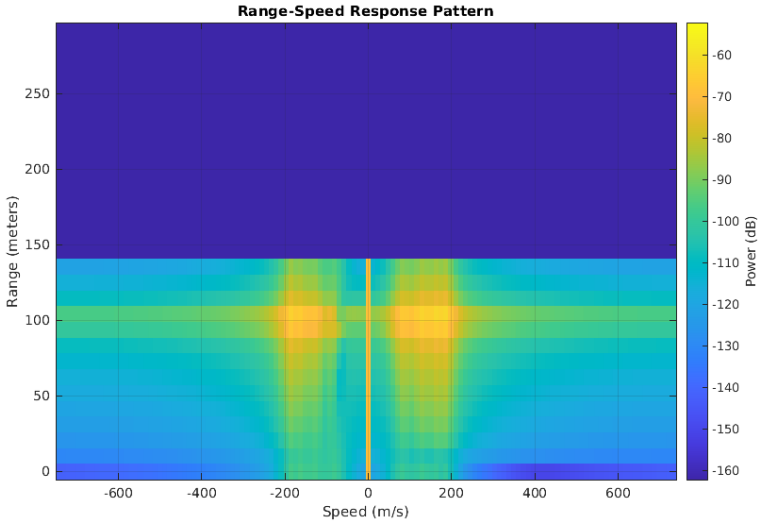

Figure 4.20: PS model range-speed response for simulation in Section 4.2.2.

model shows some lesser range and speed leakage which is consistent with MATLAB's full system simulation model in Figure 4.18. In the micro-Doppler plots for the MM and PS models, the two plots show correct shapes as well as subtle fading on the upper side of the graph at around 25 kHz. This fading is also present in the full-system simulation micro-Doppler plot where the fading causes the signal to be obscured by the presence of noise. The major differences between the micro-Doppler plots for the MM and PS models that the magnitude of the PS model is about 20 dB higher and the static component (0 Hz) is more apparent in the MM model.

In general, it is shown that the augmented MM model matches the full-system simulation and the signatures are visible and detectable in the presence of noise using the more realistic radar parameters as in Table 4.2. If one were provided the results of the experiment without knowledge of its setup, deductions can easily be made. For example, one revolution of one of the blades takes about 3 ms as shown in the spectrogram. This is equivalent to 333 revolutions per second or 20k revolutions per minute, exactly the RPM used in this simulation. Additionally, based on the bidirectional micro-Doppler shift maximums of around 70 kHz in the spectrogram, one can conclude that the propellers' velocities are 209.5 m/s using the Doppler formula. Inference can then be made that the radius of rotation for the propeller is $r = 209.5 \cdot 3 \cdot 10^{-3}/(2\pi) = 0.1$m, exactly the length of L_2 used in the simulation.

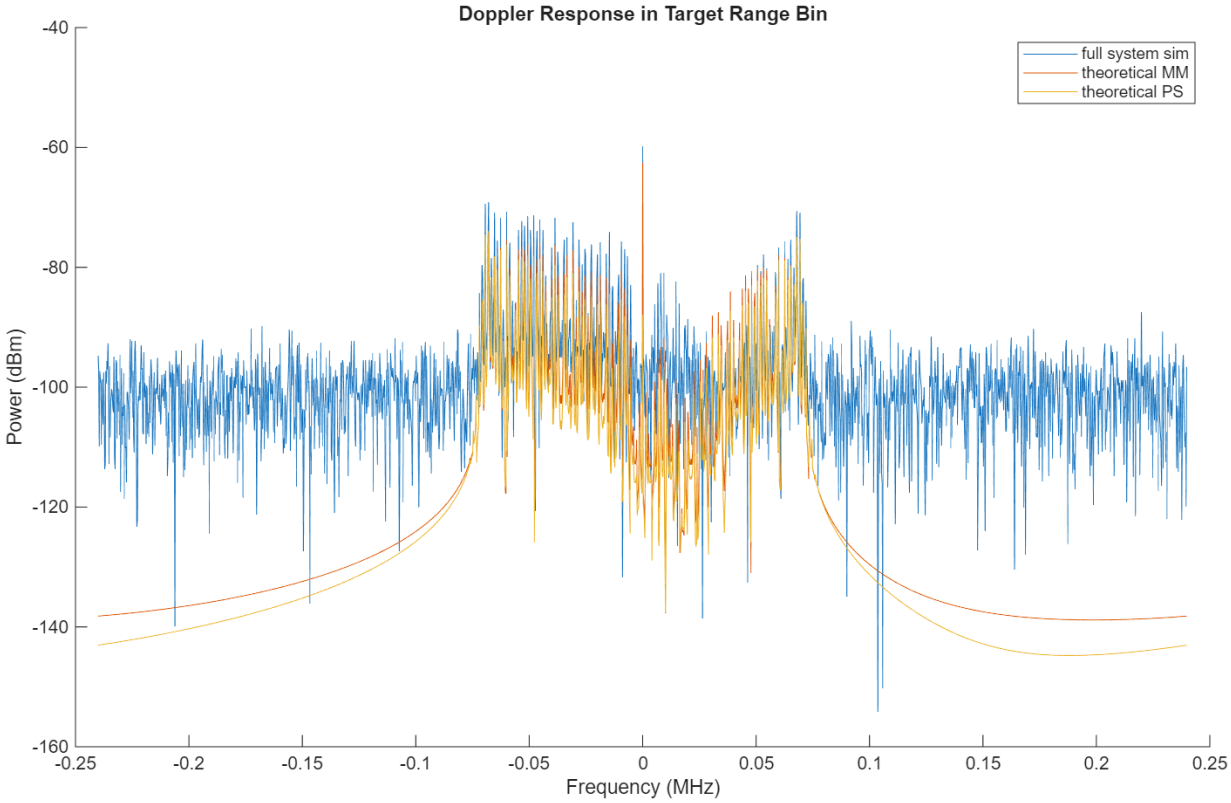

Figure 4.21: All three models are compared when analyzing a specific horizontal slice of the range-Doppler response for the system. This is effectively the same information as is contained in one slice of the range-speed response at 100m.

In addition, specific slices of either the range-speed response may be analyzed to provide further insight. For example, Figures 4.21 and 4.22 show the resulting successful comparison for a specific range and for a specific time window respectively. These figures show that the peaks and valleys of all three different models line up perfectly, even through the full system simulation's white noise present.

4.2.3 Experiment: Multiple Propeller Velocities

This section shows the results acquired from the simulation of the same scenario as in Section 4.2.1 but with the two propellers closest to the transceiver spinning at half the speed as the propellers farther away. The range of the center of the drone is chosen to land

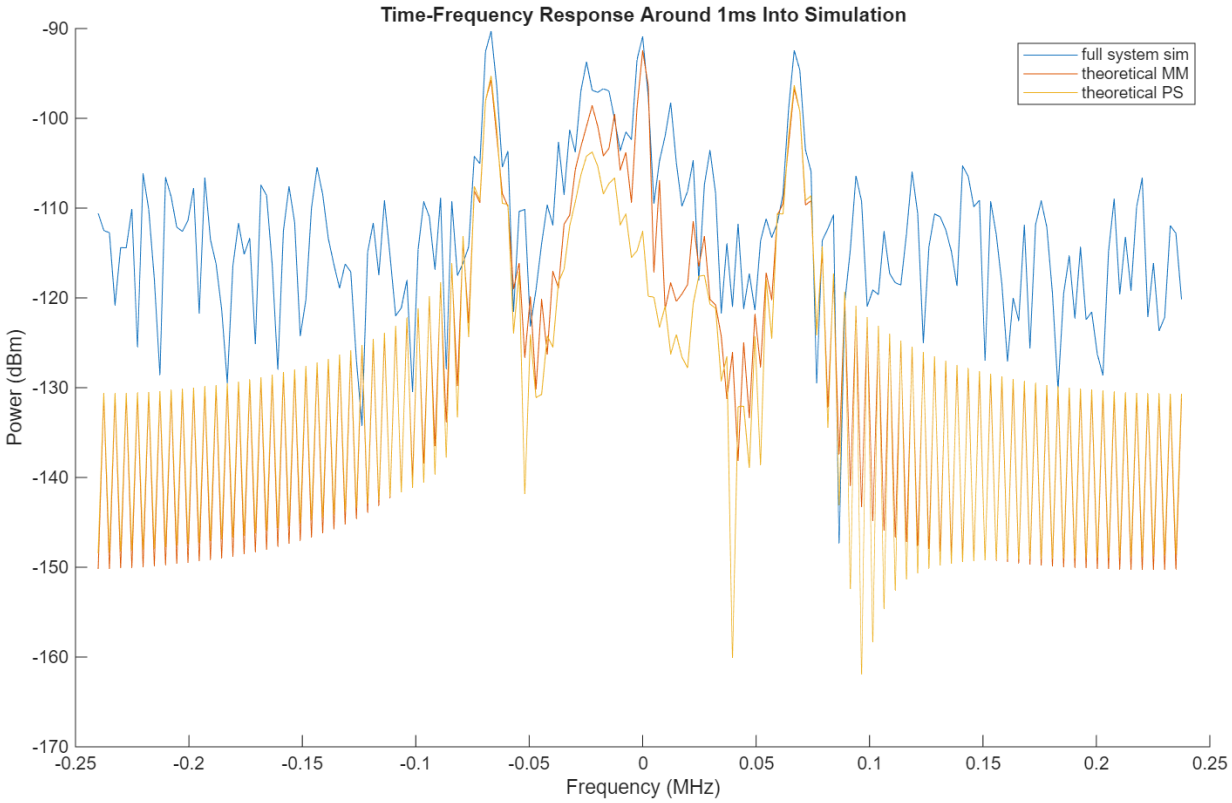

Figure 4.22: All three models are compared when analyzing a specific vertical slice of the micro-Doppler signature in the time-frequency response. The vertical slice occurs at 1ms with a time range of 0.2ms around the point, that is, from 0.9ms to 1.1ms.

directly in between two range bins: $r_1 : [88.54, 98.96]$ and $r_2 : [98.96, 109.38]$. Additionally, the distance between the center of the drone and the center of each propeller is chosen to be 5m, i.e. $||\vec{x}^u_{p_i}|| = 5 \text{ m}, \forall i$. The experiment is setup this way to unambiguously place the front propellers in r_1 and the back propellers in r_2 so it should be expected that the maximum Doppler shift shown in the micro-Doppler signature spectrogram for the front propellers be twice that of the back propellers.

First, the range correlation signals are shown in Figure 4.23. The range correlation represents how similar the transmit signal is to the received for each range bin. According to these three graphs, the correlation for the full-system simulation is higher than it is for both the MM model and the PS model. This is due to the presence of noise in the full-system simulation and its absence in the other two models. The important thing to note is that the three graphs have the same shape and peak at the exact same time. It is expected based on the simulation setup that the correlation signal peaks somewhere near 100m and be relatively flat in those two range bins and then taper off. It is clear from the Figure that there are only two range-bins which could realistically contain a portion of the target. This is excellent behavior for the MM model. The indices are r_1 and r_2 as expected for all models. The range-speed response for all three different models, shown in Figure 4.24, shows that for r_1 and r_2, different propagation Doppler shifts are present. This is consistent with what is expected. It is shown in these graphs that signal resulting from the range-bin that is farther away and containing a portion of the drone, r_2 on the y-axis, the power is less spread out than for that of portion of the signal representing the range bin r_1. We can infer from this that the propellers which are farther away are moving much slower. The range-speed response for the PS and MM models are very similar in shape which shows that the MM model accurately predicts the pattern of movement, as the PS model on the left is effectively showing the result from the full-system simulation without the noise.

Second, the micro-Doppler signatures for $\boldsymbol{r}_x[r_1, :]$ and $\boldsymbol{r}_x[r_2, :]$ are shown in Figure 4.25 and 4.26 respectively. The micro-Doppler signatures clearly show that each of the range bins are dominated by the velocities generated by the propellers in each of the range bins. Some leakage is present in that the non-dominant velocities' signatures are still present in signatures for both r_1 and r_2.

This allows for inference: a system able to perform this processing on the signals can infer that a target exists which spans r_1 and r_2. Inference can also be made that the target is composed of multiple rotating parts which rotate at different velocities which are based on the maximum frequency shift in the micro-Doppler signatures for the two range bins, similar to as is done at the end of Section 4.2.2. The ratio between static RCS and dynamic RCS can also be used to infer that either the drone component in r_1 is either a

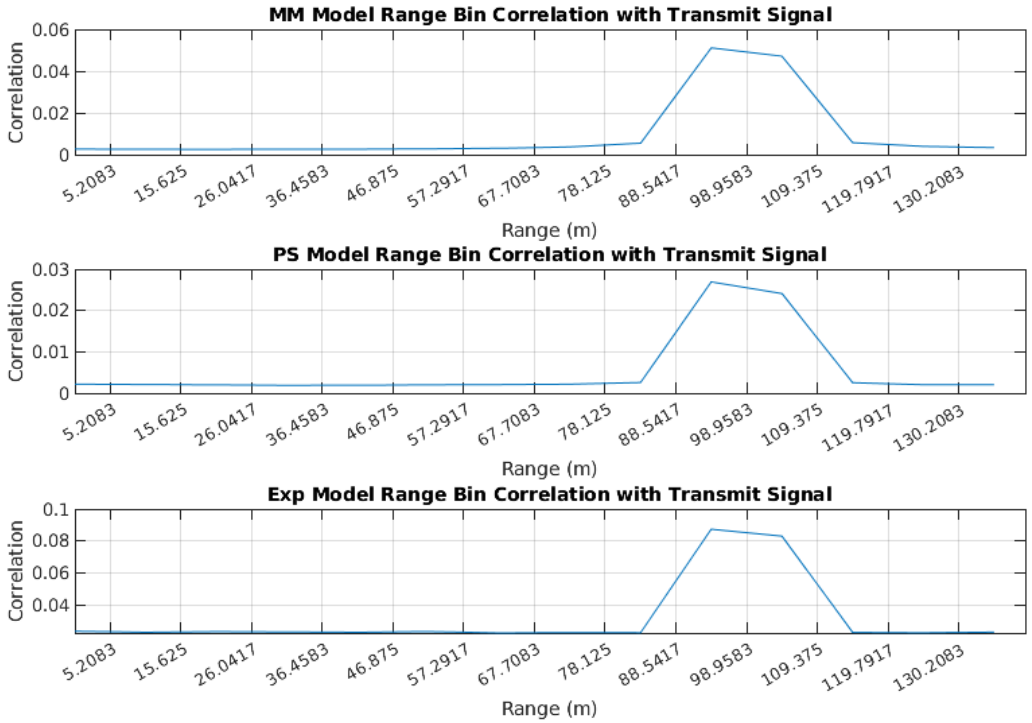

Figure 4.23: Range-bin correlation after windowing the received signals for each of the three models.

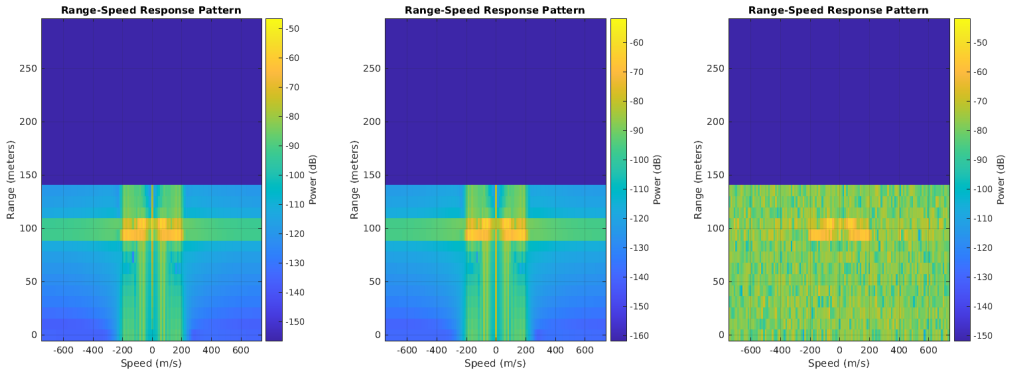

Figure 4.24: Range-speed response for all three models: left - MM model, middle - PS model, right - experimental model.

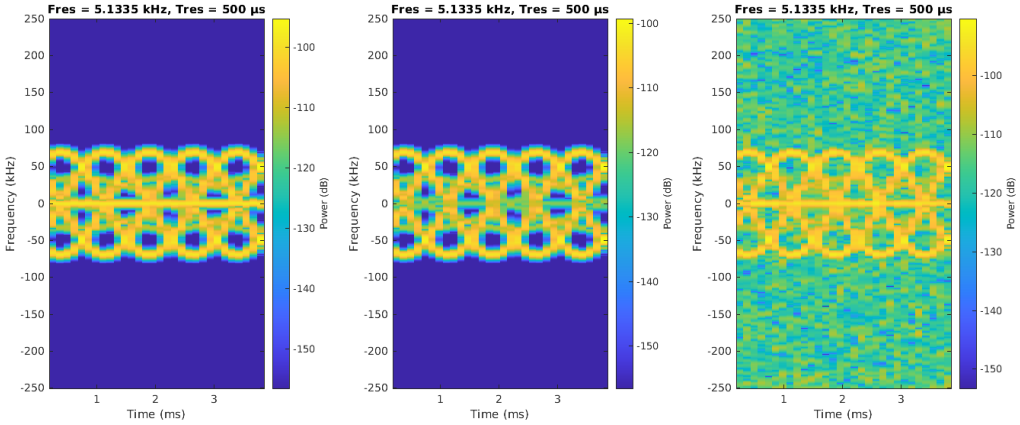

Figure 4.25: Micro-Doppler signatures for the front two propellers in the range bin at index r_1 for all three models: left - MM model, middle - PS model, right - experimental model.

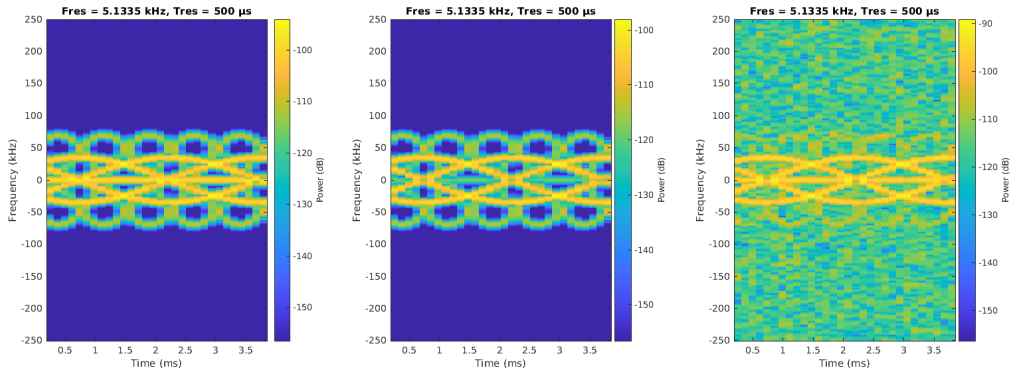

Figure 4.26: Micro-Doppler signatures for the front two propellers in the range bin at index r_2 for all three models: left - MM model, middle - PS model, right - experimental model..

large propeller or multiple smaller ones.

4.2.4 More Precise Modelling

With a larger bandwidth OFDM radar pulse signal, achievable by increasing the number of subcarriers used, the target can be broken down even further into its components. With a bandwidth of 14.4 MHz in prior experiments, corresponding to a range-bin size of 10.4m, the drone could fit in either one range-bin or two but no more. If additional precision is required or desired, the number of subcarriers could be increased to for example 1040. This would lead to a bandwidth and sampling frequency of about 1 GHz and thus a range-bin resolution of 15 cm. With this increased precision, similar analysis could be done to determine different micro-Doppler signatures at all the range-bins occupied by the target. This would produce precise data about the target allowing further inference.

4.3 Summary

In summary, two algorithms are provided for generating simulations using the augmented MM model using pulsed OFDM radar. Firstly, the simulation which makes use of the stop-and-hop approximation to enhance performance is shown. The stop-and-hop approximation assumes the drone does not move at all for the duration of a single pulse. Although it does improve performance, the accuracy of the algorithm may decrease. Hence, the second algorithm provided makes no such assumption to increase precision at the cost of computational complexity. The two algorithms are written with the nomenclature presented in this thesis to help the reader map the algorithm to portions of this work. Actual MATLAB simulations may also be provided to the reader upon request so the reader does not have to translate the algorithm into actual code. The two algorithms are explained in detail.

4.3.1 Stop-and-Hop Augmented MM model Simulation

Before the algorithm even begins, it is assumed that time-independent system parameters are set such as antenna gains and system losses as well as target parameters such as in equation 3.118. The algorithm first defines a window buffer of 5m. This window buffer allows for the receiver to continue to receive the signal even if the target is slightly outside of the window range (by an amount defined by this parameter). The pulses are then iterated

as in line 2. The time in the simulation at the start of the pulse t_p is the current pulse number times the pulse repetition interval (PRF^{-1}). The time-dependent parameters of the model - core position and velocities of UAV and transceiver, drone orientation through the rotation matrix $\boldsymbol{R}_u^o$, the rate at which the drone is spinning f_ε and the current RCS of the drone σ. The time-dependent parameters for each propeller is then updated - the blade angles Ω_i, the relative position of this propeller relative to the center of the UAV $\vec{x}_{p_i}^{\,u}$, the orientation of the propeller w.r.t. the UAV $\boldsymbol{R}_{p_i}^u$ and the rate of rotation of each propeller $f_{rot,i}$. It is up to the simulation designer to program the update_params() and update_prop_params() functions as the trajectory can be whatever they want. To remove some more work from the user, they could instead provide the Euler angles defining the orientation of the drone for the orientation matrix to be calculated thereafter. The setup for this pulse is then complete.

The pulse time then starts on line 10. The if-statement on line 11 tests whether or not the UAV is within the distance where a return signal is expected. If it's not, then the return signal value is kept at zero. The result is initialized to zero on line 12 and each of the OFDM subcarriers are iterated thereafter. Then, for each of the propellers on the UAV, the position of the center of the propeller relative to an outside observer $\vec{x}_{p_i}^{\,o}$ is calculated using orientation and position of the drone. Line 17 then iterates all the blades. The positions of the tips of the blades are then calculated first relative to the propeller and then relative to the observer. The range vector between the tip of the blade and the transceiver is calculated on line 20. The core of the augmented MM model follows: first, calculate $\vec{h}$ as in equation (3.79), next, calculate $\vec{q}$ as in equation (3.80), next, calculate l as in equation (4.13). The result for the dynamic portion of this discrete-time index is then calculated using the MM model expression in equation (4.12). Note that the RRE() function represents the amplitude term $\psi_0/L_2(R_{i,n})$ in the expression for the dynamic portion and $\psi_0\sigma/L_2(R_{i,n})$ for the static portion[1]. The for-loop iterations are terminated for the blade, propeller and subcarriers. The result matrix $\boldsymbol{r}_x$ at this index for pulse m is then set to the combination of the static and dynamic result multiplied by the amplitude of the OFDM symbol $x(k,1)$. The result index is incremented before the fast-time loop continues to the next iteration.

[1]One could also add-in a width parameter to the RRE() function for the dynamic portion of the drone which would scale the RRE by a factor of (1+width) to account for the blade not being infinitesimally thin; e.g. if the blade has a width of 4mm then the RRE would be $\psi_0 \cdot 1.004/L_2(R_{i,n})$.

4.3.2 Precise Augment MM model Simulation

The only difference between this algorithm and then stop-and-hop approximation algorithm is that the update_params() and update_prop_params() functions are called every time the time index is increased for this algorithm.

Algorithm 4.1 Stop-and-Hop Augmented MM model Simulation

$wb \leftarrow 5$ → window buffer of 5m
for $m \leftarrow 1; m \leq M; m \leftarrow m+1$ **do** → iterate the pulses; slow-time
  $t_p \leftarrow (m-1)/PRF$ → $t_p :=$ time at pulse start
  $[\vec{x}_u^o; \vec{x}_t^o; \vec{v}_u^o; \vec{v}_t^o; \boldsymbol{R}_u^o; f_\varepsilon; \sigma] \leftarrow$ update_params(t_p)
  $\vec{R} \leftarrow |\vec{x}_u^o - \vec{x}_t^o|$
  for $i \leftarrow 1; i \leq I; i \leftarrow i+1$ **do**
    $[\Omega_i; \vec{x}_{p_i}^u; \boldsymbol{R}_{p_i}^u; f_{rot,i}] \leftarrow$ update_prop_params(t_p, i)
  end for
  $idx \leftarrow 1$
  for $t \leftarrow 0; t < 1/PRF; t \leftarrow t + f_s^{-1}$ **do** → iterate time in pulse; fast-time
    if $(2(|\vec{R}| - wb)/c \leq t) \wedge (t \leq T_{symbol} + 2(|\vec{R}| + wb)/c)$ **then**
      $res \leftarrow 0$
      for $k \leftarrow -\lfloor N_s/2 \rfloor; k \leq \lceil N_s/2 \rceil - 1; k \leftarrow k+1$ **do** → iterate the subcarriers
        for $i \leftarrow 1; i \leq I; i \leftarrow i+1$ **do**
          $\vec{x}_{pi}^o \leftarrow \boldsymbol{R}_u^o \vec{x}_{p_i}^u + \vec{x}_u^o$
          $\boldsymbol{R}_{p_i}^o \leftarrow \boldsymbol{R}_u^o \boldsymbol{R}_{p_i}^u$
          for $n \leftarrow 1; n \leq N_i; n \leftarrow n+1$ **do**
            $\vec{x}_{L_2}^{p_i} \leftarrow L_2[\cos(\Omega_{n,i}); \sin(\Omega_{n,i}); 0]$
            $\vec{x}_{L_2}^o \leftarrow \boldsymbol{R}_{p_i}^o \vec{x}_{L_2}^{p_i} + \vec{x}_{pi}^o$
            $\vec{R}_{n,i} \leftarrow \vec{x}_{L_2}^o - \vec{x}_t^o$
            $\vec{h} \leftarrow \vec{v}_u^o - \vec{v}_t^o + 2\pi f_\varepsilon \boldsymbol{R}_u^o [-{}_z x_{p_i}^u; 0; {}_x x_{p_i}^u]$
            $\vec{q} \leftarrow f_{rot,i} \boldsymbol{R}_{p_i}^o [-\sin(\Omega_{n,i}); \cos(\Omega_{n,i}); 0]$
            $l \leftarrow \frac{4\pi}{c}\big(f_c + \frac{k}{T_{symbol}}\big)\frac{\vec{q}\cdot\vec{R}_{n,i}}{|\vec{R}_{n,i}|}\big(t - \frac{2|\vec{R}_{n,i}|}{c}\big)$
            $res \leftarrow res + x(k,1)(L_2 - L_1)\mathrm{RRE}(|\vec{R}_{n,i}|)\exp\Big(j2\pi\big(f_c + \frac{k}{T_{symbol}}\big)\big(t - \frac{2|\vec{R}_{n,i}|}{c}\big)\Big)$
              $\cdot \exp\Big(j4\pi\big(f_c + \frac{k}{T_{symbol}}\big)c^{-1}\big(\frac{\vec{h}\cdot\vec{R}_{n,i}}{|\vec{R}_{n,i}|}\big)\big(t - \frac{2|\vec{R}_{n,i}|}{c}\big)\Big)$
              $\cdot \exp(j(L_1 + L_2)l/2)\mathrm{sinc}((L_2 - L_1)l/2)$ → compute Rx signal
          end for
        end for
        $res \leftarrow res + x(k,1)\mathrm{RRE}(R)\exp\Big(j2\pi f_c\big(t - \frac{2|\vec{R}|}{c}\big)\Big)$
      end for
      $\boldsymbol{r}_x[idx, m] \leftarrow res$
    end if
    $idx \leftarrow idx + 1$
  end for
end for

Algorithm 4.2 Precise Augmented MM model Simulation

$wb \leftarrow 5$ → window buffer of 5m
for $m \leftarrow 1; m \leq M; m \leftarrow m+1$ **do** → iterate the pulses; slow-time
  $t_p \leftarrow (m-1)/PRF$ → $t_p :=$ time at pulse start
  $idx \leftarrow 1$
  for $t \leftarrow 0; t < 1/PRF; t \leftarrow t + f_s^{-1}$ **do** → iterate time in pulse; fast-time
    $[\vec{x}_u^o; \vec{x}_t^o; \vec{v}_u^o; \vec{v}_t^o; \boldsymbol{R}_u^o; f_\varepsilon; \sigma] \leftarrow$ update_params$(t_p + t)$
    $\vec{R} \leftarrow |\vec{x}_u^o - \vec{x}_t^o|$
    for $i \leftarrow 1; i \leq I; i \leftarrow i+1$ **do**
      $[\Omega_i; \vec{x}_{p_i}^u; \boldsymbol{R}_{p_i}^u; f_{rot,i}] \leftarrow$ update_prop_params$(t_p + t, i)$
    end for
    if $(2(|\vec{R}| - wb)/c \leq t) \wedge (t \leq T_{symbol} + 2(|\vec{R}| + wb)/c)$ **then**
      $res \leftarrow 0$
      for $k \leftarrow -\lfloor N_s/2 \rfloor; k \leq \lceil N_s/2 \rceil - 1; k \leftarrow k+1$ **do** → iterate the subcarriers
        for $i \leftarrow 1; i \leq I; i \leftarrow i+1$ **do**
          $\vec{x}_{pi}^o \leftarrow \boldsymbol{R}_u^o \vec{x}_{p_i}^u + \vec{x}_u^o$
          $\boldsymbol{R}_{p_i}^o \leftarrow \boldsymbol{R}_u^o \boldsymbol{R}_{p_i}^u$
          for $n \leftarrow 1; n \leq N_i; n \leftarrow n+1$ **do**
            $\vec{x}_{L_2}^{p_i} \leftarrow L_2[\cos(\Omega_{n,i}); \sin(\Omega_{n,i}); 0]$
            $\vec{x}_{L_2}^o \leftarrow \boldsymbol{R}_{p_i}^o \vec{x}_{L_2}^{p_i} + \vec{x}_{pi}^o$
            $\vec{R}_{n,i} \leftarrow \vec{x}_{L_2}^o - \vec{x}_t^o$
            $\vec{h} \leftarrow \vec{v}_u^o - \vec{v}_t^o + 2\pi f_\varepsilon \boldsymbol{R}_u^o [-{}_z x_{p_i}^u; 0; {}_x x_{p_i}^u]$
            $\vec{q} \leftarrow f_{rot,i} \boldsymbol{R}_{p_i}^o [-\sin(\Omega_{n,i}); \cos(\Omega_{n,i}); 0]$
            $l \leftarrow \frac{4\pi}{c}\big(f_c + \frac{k}{T_{symbol}}\big)\frac{\vec{q}\cdot\vec{R}_{n,i}}{|\vec{R}_{n,i}|}\big(t - \frac{2|\vec{R}_{n,i}|}{c}\big)$
            $res \leftarrow res + x(k,1)(L_2 - L_1)\mathrm{RRE}(|\vec{R}_{n,i}|)\exp\Big(j2\pi\big(f_c + \frac{k}{T_{symbol}}\big)\big(t - \frac{2|\vec{R}_{n,i}|}{c}\big)\Big)$
              $\cdot \exp\Big(j4\pi\big(f_c + \frac{k}{T_{symbol}}\big)c^{-1}\big(\frac{\vec{h}\cdot\vec{R}_{n,i}}{|\vec{R}_{n,i}|}\big)\big(t - \frac{2|\vec{R}_{n,i}|}{c}\big)\Big)$
              $\cdot \exp(j(L_1 + L_2)l/2)\mathrm{sinc}((L_2 - L_1)l/2)$ → compute Rx signal
          end for
        end for
        $res \leftarrow res + x(k,1)\mathrm{RRE}(R)\exp\Big(j2\pi f_c\big(t - \frac{2|\vec{R}|}{c}\big)\Big)$
      end for
      $\boldsymbol{r}_x[idx, m] \leftarrow res$
    end if
    $idx \leftarrow idx + 1$
  end for
end for

Chapter 5

Conclusion

5.1 Conclusions

The problem statement of constructing a simple, versatile, closed-form simulation model which can be used to model OFDM pulsed-radar reflections from drones is answered by a simulation model constructed by starting with the MM model and augmenting it to allow it to include multiple propellers along with a rigid body and using an OFDM pulsed radar. Algorithms 4.1 and 4.2 how exactly how these simulations are performed. Since the simulation is constructed using the augmented MM model derived here instead of the industry standard way to model complex targets, the point-scatterer model, redundancy is achieved. This is beneficial to increase one's certainty that the simulations will match real-world data when generating predictions if the two models agree. The two models are shown to produce very similar results through various MATLAB simulations. From the prediction output, one can infer: drone position relative to the transceiver, orientation, topology, velocity, etc.

5.2 Summary of Contributions

1. **Derivation of closed-form drone backscatter model for OFDM radar using MM model.** No other source provides a radar backscatter modeling mechanism specifically for drones which has so few assumptions which limit it. As explored in Section 1.1, the assumptions of various other authors limit the capacity of their simulation algorithms such as limiting the movement capability of the simulated

target or its topology. The modeling method presented in this thesis allows the simulator to construct any arbitrary scenario with a drone model whose topology is free to vary as the simulator wants. In using the point-scatterer model to define a complex target in a simulation, a lot of work is needed to define exactly where each point-scatterer is and what their velocities are at each point in time. The framework presented in this thesis simplifies this process in the MM model and can also be used to facilitate this task of modeling the target using the point-scatterer model.

2. **Implementation of simulation models in various scenarios.** Various simulations have been constructed throughout this thesis which showcase that, in each scenario, the model provides accurate predictions compared to the industry-standard algorithm with full-system simulations. These show easily that multiple inferences can be made about the target given only the result of the simulation, such as position, topology and velocity of the drone. From the implementation of the simulations, a conclusion was made as to how the far-field approximation should be used to most accurately predict the micro-Doppler effect using the MM model.

3. **Derivation of augmented Martin-Mulgrew model.** No other sources explicitly extend the MM model beyond its original use which was to model the backscatter from a single propeller where the height of the propeller center is equal to the height of the monostic transceiver. This can be useful for anyone looking to use the model in a more general manner in the future.

4. **Derivation of initial Martin-Mulgrew model.** The best source for deriving the initial MM model is [15], however, it is not the most detailed derivation. The derivation provided in this thesis can help in the understanding of this model.

5.3 Future Works

By virtue of using an OFDM radar in this work with numerous degrees-of-freedom such as the data symbols, the modulation type, the number of subcarriers, etc., various ideas can be explored.

1. **JCR/ISAC.** An optimization problem can be looked into where data rate and radar capability are simultaneously maximized, though the two are inherently a trade-off. This would allow the multi-purpose use of OFDM transceivers.

2. **Bistatic/multistatic inferences.** Instead of having a monostatic transceiver as in this thesis, consideration can be made for different positions and velocities of transmitters and receivers in the same OFDM environment. This would allow for better, more precise positional inference for the target through triangulation and redundancy.

3. **Optimal OFDM TX radar signal.** Since the radar's transmit signal can vary significantly in this framework, it would be useful to know what the optimal OFDM radar transmit signal is. This could be done by examining the ambiguity function of various candidate transmit waveforms fitting the framework.

4. **Machine Learning training of classification or general inference models.** This simulator could be used to provide training data for ML models. One obvious use-case would be to generate the training data for an ML model in the form of the micro-Doppler time-frequency plot and validate the model using real-world data. A highly accurate model would validate the use of simulations to augment the training data.

5. **Further analytical computations.** Substituting the position of each of the blades on the drone for an analytical expression produces an expression including the Bessel function. This could be further explored to provide closed-form solutions and analytical insights.

6. **Low Probability of Intercept (LPI).** Using an OFDM radar could allow for a signal which is not obviously a radar signal but still perform as one. Simulations can be done using the simulator constructed here to predict how well an LPI transmit waveform would perform.

7. **Interference with users on the 5G system.** Using an OFDM radar in the manner described in this thesis could interfere with users on the 5G system. Further processing could be done at the base stations to prevent this.

References

[1] 3GPP. Tr 21.917 v17.0.1 technical specification group services and system aspects. https://portal.3gpp.org/desktopmodules/Specifications/SpecificationDetails.aspx?specificationId=3937, 2023.

[2] A. Ahmed, Y. D. Zhang, and A. Hassanien. Joint radar-communications exploiting optimized ofdm waveforms. *Remote sensing (Basel, Switzerland)*, 13(21):4376–, 2021.

[3] S. Aziez, E. Hamza, F. Hummadi, and A. Sabry. Implementation of radar cross-sections model for targets with different scattering centers. *Eastern-European Journal of Enterprise Technologies*, 5(9(119)):54–60, Oct. 2022.

[4] C. Baquero Barneto, T. Riihonen, M. Turunen, L. Anttila, M. Fleischer, K. Stadius, J. Ryynanen, and M. Valkama. Full-duplex ofdm radar with lte and 5g nr waveforms: Challenges, solutions, and measurements. *IEEE transactions on microwave theory and techniques*, 67(10):4042–4054, 2019.

[5] M. Bednarz and T. P. Zielinski. Remote radio frequency sensing based on 5g new radio positioning reference signals. *Sensors (Basel, Switzerland)*, 25(2):337–, 2025.

[6] S. Blandino, N. Golmie, A. Sahoo, T. Nguyen, T. Ropitault, D. Griffith, and A. Sonny. Detecting airborne objects with 5g nr radars, 2025.

[7] V. C. Chen and W. J. Tahmoush, D.and Miceli. *Radar micro-doppler signatures : processing and applications*. IET Radar, Sonar and Navigation Series ; 34. The Institution of Engineering and Technology, London, 2014 - 2014.

[8] V.C. Chen, F. Li, S.-S. Ho, and H. Wechsler. Micro-doppler effect in radar: phenomenon, model, and simulation study. *IEEE transactions on aerospace and electronic systems*, 42(1):2–21, 2006.

[9] Y. Chen, J. Zhang, W. Feng, and M. Alouini. Radio sensing using 5g signals: Concepts, state of the art, and challenges. *IEEE internet of things journal*, 9(2):1037–1052, 2022.

[10] H. C. A. Costa, S. J. Myint, C. Andrich, S. W. Giehl, C. Schneider, and Reiner S. T. Bistatic reflectivity and micro-doppler signatures of drones for integrated communication and sensing. In *2024 International Radar Symposium (IRS)*, pages 194–199. Warsaw University of Technology, 2024.

[11] H. C. A. Costa, S. J. Myint, C. Andrich, S. W. Giehl, C. Schneider, and R. S. Thoma. Modelling micro-doppler signature of drone propellers in distributed isac. In *Proceedings of the IEEE National Radar Conference (1996)*, pages 1–6. IEEE, 2024.

[12] Y. Cui, X. Jing, and J. Mu. Integrated sensing and communications via 5g nr waveform: Performance analysis. In *Proceedings of the ... IEEE International Conference on Acoustics, Speech and Signal Processing (1998)*, pages 8747–8751. IEEE, 2022.

[13] A. Dey, Y. Cabanes, S. Rajan, B. Balaji, A. Damini, and R. Chanchlani. Radar-based drone detection using complex-valued convolutional neural network. In *2023 IEEE Sensors Applications Symposium (SAS)*, pages 1–5. IEEE, 2023.

[14] M. Ezuma, M. Funderburk, and I. Guvenc. Compact-range rcs measurements and modeling of small drones at 15 ghz and 25 ghz. In *Proceedings (IEEE Radio and Wireless Symposium. Online)*, pages 313–316. IEEE, 2020.

[15] A. French. *Target recognition techniques for multifunction phased array radar*. PhD thesis, University College London, 2010.

[16] H.T. Friis. A note on a simple transmission formula. *Proceedings of the IRE*, 34(5):254–256, 1946.

[17] D. Gaglione, C. Clemente, C. V. Ilioudis, A. R. Persico, I. K. Proudler, J. J. Soraghan, and A. Farina. Waveform design for communicating radar systems using fractional fourier transform. *Digital signal processing*, 80:57–69, 2018.

[18] J. Gong, J. Yan, D. Li, and D. Kong. Detection of micro-doppler signals of drones using radar systems with different radar dwell times. *Drones (Basel)*, 6(9):262–, 2022.

[19] R. Guay, G. Drolet, and J. R Bray. Measurement and modelling of the dynamic radar cross-section of an unmanned aerial vehicle. *IET radar, sonar & navigation*, 11(7):1155–1160, 2017.

[20] K. Guo, X. Han, and X. Sheng. Scattering center models of backscattering waves by dielectric spheroid objects. *Opt. Express*, 26(4):5060–5074, Feb 2018.

[21] G. Hakobyan and B. Yang. A novel intercarrier-interference free signal processing scheme for ofdm radar. *IEEE transactions on vehicular technology*, 67(6):5158–5167, 2018.

[22] S. Katz and A. Tal. Hpro: Direct visibility of point clouds for optimization. *Computer graphics forum*, 44(2), 2025.

[23] O. Kilic, J. M. Garcia-Rubia, N. Tran, V. Dang, and Q. Nguyen. Detection of moving human micro-doppler signature in forest environments with swaying tree components by wind. *Radio science*, 50(3):238–248, 2015.

[24] G. Lellouch, A. K. Mishra, and M. Inggs. Design of ofdm radar pulses using genetic algorithm based techniques. *IEEE transactions on aerospace and electronic systems*, 52(4):1953–1966, 2016.

[25] K. Li, X. Qu, Y. Wu, Y. Xia, and W. Li. A method for micro-doppler extraction under passive radar based on communiction signal. In *IGARSS 2019 - 2019 IEEE International Geoscience and Remote Sensing Symposium*, pages 3760–3763. IEEE, 2019.

[26] Y. Lin, T. Lee, and C. Lin. Interference avoidance and cancellation in automotive ofdm radar networks. *Journal of signal processing systems*, 92(12):1383–1396, 2020.

[27] M. Liu, F. Gao, Z. Cui, S. Pollin, and Q. Liu. Sensing with ofdm waveform at mmwave band based on micro-doppler analysis. In *2023 IEEE International Conference on Communications Workshops (ICC Workshops)*, pages 1398–1403. IEEE, 2023.

[28] B. R. Mahafza, S. C. Winton, and A. Z. Elsherbeni. *Handbook of radar signal analysis*. Advances in Applied Mathematics. Chapman & Hall/CRC, Boca Raton, FL, 1st ed. edition, 2021.

[29] R. Maksymiuk, K. Abratkiewicz, P. Samczyński, and M. Płotka. Rényi entropy-based adaptive integration method for 5g-based passive radar drone detection. *Remote sensing (Basel, Switzerland)*, 14(23):6146–, 2022.

[30] J. Martin and B. Mulgrew. Analysis of the theoretical radar return signal form aircraft propeller blades. In *IEEE International Conference on Radar*, pages 569–572. IEEE, 1990.

[31] F. Mattei, C. Conte, V. Carotenuto, G. Rufino, A. De Maio, D. Accardo, A. Di Vincenzo, C. Esposito, A. Natale, P. Berardino, G. Palmese, S. Perna, and R. Lanari. *Exploring the Dynamic RCS of Small Drones Using FMCW Radar*.

[32] S. Mazahir, S. Ahmed, and M. Alouini. A survey on joint communication-radar systems. *Frontiers in communications and networks*, 1, 2021.

[33] M. Moore, D. A. Robertson, and S. Rahman. A new simulation methodology for generating accurate drone micro-doppler with experimental validation. *IET radar, sonar & navigation*, 18(3):477–492, 2024.

[34] A. V. Oppenheim and R. W. Schafer. *Discrete-time signal processing*. Pearson, Upper Saddle River, 3rd ed. edition, 2010.

[35] X. Qu, K. Li, Q. Zhang, and B. Liang. Micro-doppler feature extraction under passive radar based on orthogonal frequency division multiplexing communication signal. *Journal of engineering (Stevenage, England)*, 2019(20):6889–6893, 2019.

[36] D. Raval, E. Hunter, S. Hudson, A. Damini, and B. Balaji. Convolutional neural networks for classification of drones using radars. *Drones (Basel)*, 5(4):149–, 2021.

[37] M. A. Richards, J. A. Scheer, and W. A. Holm. *Principles of Modern Radar Basic principles*. Radar, Sonar & Navigation. SciTech Publishing Inc., Edison, NJ, 2010.

[38] J. Rosen and L. Quinn. *Encyclopedia of Physical Science*. Infobase Publishing, 2009.

[39] M.A. Sebt, A. Sheikhi, and M.M. Nayebi. Orthogonal frequency-division multiplexing radar signal design with optimised ambiguity function and low peak-to-average power ratio. *IET Radar, Sonar & Navigation*, 3:122–132, 2009.

[40] D. Segura, E. J. Khatib, J. Munilla, and R. Barco. 5g numerologies assessment for urllc in industrial communications. *Sensors (Basel, Switzerland)*, 21(7):2489–, 2021.

[41] S. Sen. Adaptive ofdm radar waveform design for improved micro-doppler estimation. *IEEE sensors journal*, 14(10):3548–3556, 2014.

[42] S. Sen and A. Nehorai. Adaptive ofdm radar for target detection in multipath scenarios. *IEEE transactions on signal processing*, 59(1):78–90, 2011.

[43] B. Siciliano. *Robotics : modelling, planning and control*. Advanced textbooks in control and signal processing. Springer, London, 2010 - 2010.

[44] Y. L. Sit, B. Nuss, and T. Zwick. On mutual interference cancellation in a mimo ofdm multiuser radar-communication network. *IEEE transactions on vehicular technology*, 67(4):3339–3348, 2018.

[45] M. I. Skolnik. *Radar handbook*. McGraw-Hill's AccessEngineering. McGraw-Hill Professional, Maidenhead, 3rd ed. edition, 2008.

[46] C. Sturm and W. Wiesbeck. Waveform design and signal processing aspects for fusion of wireless communications and radar sensing. *Proceedings of the IEEE*, 99(7):1236–1259, 2011.

[47] T. Thayaparan, S. Abrol, E. Riseborough, L. Stankovic, D. Lamothe, and G. Duff. Analysis of radar micro-doppler signatures from experimental helicopter and human data. *IET Radar, Sonar & Navigation*, 1:289–299, 2007.

[48] S. R. Wang, J. Y. Dai, J. Ch. Ke, Zh. Y. Chen, Q. Y. Zhou, Zh. J. Qi, Y. J. Lu, Y. Huang, M. K. Sun, Q. Cheng, and T. J. Cui. Radar micro-doppler signature generation based on time-domain digital coding metasurface. *Advanced science*, 11(19):e2306850–n/a, 2024.

[49] Z. Wei, H. Qu, Y. Wang, X. Yuan, H. Wu, Y. Du, K. Han, N. Zhang, and Z. Feng. Integrated sensing and communication signals toward 5g-a and 6g: A survey. *IEEE internet of things journal*, 10(13):11068–11092, 2023.

[50] M. Wypich and T. P. Zielinski. 5g nr based radar-on-demand using channel impulse response estimate. In *2023 Signal Processing Symposium (SPSympo)*, pages 220–225. Warsaw University of Technology, Institute of Electronic Systems, 2023.

[51] Y. Xia, Z. Song, Z. Lu, and Q. Fu. A novel range-doppler imaging algorithm with ofdm radar. *Chinese journal of aeronautics*, 29(2):492–501, 2016.

[52] J. Yan, H. Hu, J. Gong, D. Kong, and D. Li. Exploring radar micro-doppler signatures for recognition of drone types. *Drones (Basel)*, 7(4):280–, 2023.